République Algérienne Démocratique et Populaire
Ministère de l'Enseignement Supérieur et de la Recherche Scientifique
Université Batna -2- Mostefa Benboulaid
Faculté de Technologie
Département d'Électronique

THÈSE

Présentée pour l'obtention du diplôme de
DOCTORAT en SCIENCES
Spécialité: Électronique
Option: Micro-ondes

Par

Ferroudji Karim

Thème

Particle characterization by ultrasound using artificial intelligence methods

Soutenue le 30/11/2017
Devant le jury:

Nom & Prénoms	Grade	Qualité	Université/Etablissement
SAIDI Lamir	Professeur	Président	Batna -2- Mostefa Benboulaid
BENOUDJIT Nabil	Professeur	Rapporteur	Batna -2- Mostefa Benboulaid
BOUAKAZ Ayache	Directeur de recherche	Co-Rapporteur	François Rabelais Tours (France)
GOLEA Noureddine	Professeur	Examinateur	Oum El Bouaghi
GHOGGALI Noureddine	Maître de conférences A	Examinateur	Batna -2- Mostefa Benboulaid
KACHA Abdellah	Professeur	Examinateur	Jijel

Abstract

This thesis presents a study on how microemboli problems can be detected and characterized. It investigates a novel approach to the detection and classification of microemboli using a combination of data mining techniques, signal processing methods, and Radio Frequency information extracted from gaseous and solid emboli instead of the traditionally used Doppler signals processing.

Embolic phenomena, whether air or particulate emboli which are particles larger than blood cells, could occlude blood vessels and consequently prevent the normal blood flow to vital organs and surrounding tissue. As a result, it can induce immediate damages like heart attack or ischemic stroke. It is believed that detecting the emboli in early stage could prevent or reduce the associated risks of embolism. Embolus composition (gaseous or particulate matter) is vital in predicting clinically significant complications. Unfortunately, embolus detection using Doppler methods have shown their limits to differentiate solid and gaseous embolus. Radio Frequency (RF) ultrasound signals backscattered by the emboli contain additional information on the embolus in comparison to the traditionally used Doppler signals. Gaseous bubbles show a nonlinear behavior under specific conditions of the ultrasound excitation wave, this nonlinear behavior is exploited to differentiate solid from gaseous microemboli.

In order to verify the usefulness of RF ultrasound signal processing in the detection and classification of microemboli, an in vitro set-up is developed at the University of François Rabelais Tours, France in the INSERM U930 laboratory under the direction of Professor A. Bouakaz. Sonovue micro bubbles are exploited to mimic the acoustic behavior of gaseous emboli. They are injected in a nonrecirculating flow phantom containing a tube of 0.8 mm in diameter. The tissue mimicking material surrounding the tube is chosen to imitate the acoustic behavior of solid emboli. Both gaseous and solid emboli are imaged using an Anthares ultrasound scanner with a probe emitting at a transmit frequency of 1.82 MHz and at two mechanical indices (MI) 0.2 and 0.6. Therefore, we acquire four datasets, each dataset consists of 102 samples (51 gaseous emboli and 51 solid emboli). This dataset is exploited to create a number of discriminative features used for the detection and classification of circulating microemboli.

First, we employ Fast Fourier Transform approach based on neural network analysis using fundamental and second harmonic components information contained in the RF signal backscattered by an embolus. The proposed approach allows the classification of microemboli with a discrimination rate of 92.85%.

Second, we exploit a discrete wavelet transform approach using three dimensionality reduction algorithms; Differential Evolution technique, Fisher Score method, and Principal Component Analysis based on Support Vector Machines in the analysis and the characterization of the backscattered RF ultrasound signals from the emboli. Furthermore, we propose a strategy to select the suitable wavelet filter among 59 mother wavelet functions. The experimental results, based on the selected wavelet function and differential evolution algorithm, show clearly that discrete wavelet transform method achieves better average classification rates (96.42%) compared to the results obtained in the previous method using FFT based approach. The obtained results demonstrated that Radio Frequency ultrasound signals bring real opportunities for microemboli detection and characterization.

Résumé

Cette thèse présente une étude sur la façon dont les micro-emboles peuvent être détectés et caractérisés. Elle examine une nouvelle approche pour la détection et la classification des micro-emboles en utilisant une combinaison: des techniques d'intelligence artificielle, des méthodes de traitement du signal et de l'information extraite des emboles gaz et solides en utilisant les signaux radiofréquence (RF) au lieu des signaux Doppler traditionnellement utilisés.

Les phénomènes emboliques, que ce soit de l'air ou des emboles solides, sont des particules plus grandes que les cellules sanguines, qui pourraient obstruer les vaisseaux sanguins et par conséquent empêcher le flux sanguin normal aux organes vitaux et au tissu environnant. Par conséquent, ils peuvent induire des dommages immédiats comme une crise cardiaque ou un accident ischémique cérébral. La composition de l'embole (gaz ou solide) est essentielle dans la prévision de complications cliniquement significatives. Malheureusement, la détection des emboles en utilisant le Doppler a montré leurs limites pour différencier l'embole solide et l'embole gaz. Les signaux ultrasonores radiofréquence (RF) rétrodiffusés par les emboles contiennent des informations supplémentaires sur l'embole par rapport aux signaux Doppler traditionnellement utilisés. Les bulles gazeuses montrent un comportement non linéaire dans des conditions spécifiques de l'onde d'excitation ultrasonore, ce comportement non linéaire est exploité pour différencier les emboles solides des emboles gaz.

Afin de vérifier l'utilité du traitement des signaux ultrasonores RF dans la détection et la classification des micro-emboles, une étude expérimentale (in vitro) est développée à l'Université de François Rabelais Tours, en France, dans le laboratoire INSERM U930 sous la direction du Professeur A. Bouakaz. Les microsbulles de Sonovue sont exploitées pour imiter le comportement acoustique des emboles gaz. Elles sont injectées dans un phantom (nonrecirculating flow phantom), qui a les mêmes caractéristiques que le tissu humain, contenant un trou de diamètre de 0.8 mm. Le matériau imitant le tissu entourant le tube est choisi pour imiter le comportement acoustique de l'embolie solide. Les images échographiques des emboles gaz et solides sont recueillies à l'aide d'un scanner à ultrasons Anthares avec une sonde émettant à une fréquence d'émission de 1.82 MHz et avec deux index mécaniques (MI) 0.2 et 0.6. Donc, nous avons construit quatre bases de données, chaque base de données est composée de 102 échantillons (51 emboles gaz et 51 emboles solides). L'ensemble de ces quatre bases de données sont exploitées pour extraire un certain

nombre de caractéristiques discriminatives utilisées pour la détection et la classification des micro-emboles.

En premier lieu, nous proposons une nouvelle approche basée sur la transformée de Fourier rapides (FFT) et les réseaux de neurone artificielles (classificateur) en utilisant les propriétés de la fondamentale et de la deuxième composante harmonique contenue dans le signal RF rétrodiffusé par un embole (gaz ou solide). L'approche proposée permet la classification des micro-emboles avec un taux de discrimination de 92.85%.

En second lieu, nous exploitons la transformée en ondelettes discrète en utilisant trois algorithmes de réduction de dimensionnalité: la technique évolution différentielle, méthode Fisher Score et l'Analyse en Composantes Principales basées sur les machines à vecteurs de support (SVM: classificateur), dans l'analyse et la caractérisation des signaux RF ultrasonores rétrodiffusés de l'embole (gaz ou solide). De plus, nous proposons une stratégie pour sélectionner le filtre d'ondelettes approprié (meilleure ondelette mère) parmi 59 filtres. Les résultats expérimentaux, basés sur la fonction d'ondelettes sélectionnée et l'algorithme d'évolution différentielle, montrent clairement que la méthode basée sur la transformée en ondelettes discrète atteint de meilleurs taux de classification (96.42%) par rapport aux résultats obtenus dans la méthode précédente en utilisant l'approche basée sur la FFT. Les résultats obtenus ont démontré que les signaux radiofréquence ultrasonores offrent de réelles opportunités pour la détection et la caractérisation des micro-emboles.

ملخص

تقدم هذه الأطروحة دراسة عن كيفية اكتشاف مشاكل الميكروأومبولي وتميزها. وهي تحقق في نهج جديد للكشف عن الميكروبمولي وتصنيفه باستخدام مزيج من تقنيات استخراج البيانات وطرق معالجة الإشارات ومعلومات التردد الراديوي المستخرجة من الميكروأومبولي الغازية والصلبة بدلا من معالجة إشارات دوبلر المستخدمة تقليديا. يمكن لظواهر الميكروأومبولي، سواء كانت هواء أو جسيمات صلبة، و التي هي جسيمات أكبر من خلايا الدم، أن تسد الأوعية الدموية وبالتالي تمنع تدفق الدم الطبيعي إلى الأعضاء الحيوية والأنسجة المحيطة بها. ونتيجة لذلك, يمكن أن تسبب أضرارا مباشرة مثل الأزمة القلبية أو الجلطة الدماغية. يمكن للكشف عن الميكروأومبولي في المراحل المبكرة أن يمنع أو يقلل من المخاطر المرتبطة بانسداد الشرايين. تكوين الميكروأومبولي (الغازية أو الجسيمات الصلبة) أمر حيوي في التنبؤ بالمضاعفات الهامة في الكشف الطبي . للأسف، كشف الانسداد باستخدام أساليب دوبلر أظهرت حدودها للتمييز بين الميكروأومبولي الصلبة والغازية. تحتوي إشارات الموجات فوق الصوتية الراديوية (الترددات الراديوية) المرتدة بواسطة الميكروأومبولي على معلومات إضافية مقارنة بإشارات دوبلر المستخدمة تقليديا. الفقاعات الغازية تظهر سلوك غير خطي في ظل ظروف محددة من الموجات فوق الصوتية. يتم استغلال هذا السلوك غير الخطي للتمييز بين الميكروأومبولي الغازية و الصلبة.

من أجل التحقق من فائدة معالجة الموجات فوق الصوتية في كشف وتصنيف الميكروأومبولي ، تمت دراسة تجريبية (في المختبر) في جامعة فرانسوا رابليه تور، فرنسا، في المختبر INSERM U930 تحت إشراف البروفيسور ع.بوعكاز. تم استغلال فقاعات سونوفو الصغيرة لتقليد السلوك الصوتي الميكروأومبولي الغازية. حيث تم حقنها في نسيج اصطناعي (لديه نفس خصائص الأنسجة البشرية) يحتوي على أنبوب قطره 0.8 مم. تم اختيار المادة المحيطة بأنبوب الأنسجة لتقليد السلوك الصوتي للميكروأومبولي الصلبة. تصوير كل من للميكروأومبولي الغازية والصلبة تم باستخدام جهاز التصوير بالموجات فوق الصوتية مع مسبار يبعث على تردد الإرسال 1.82 ميغاهيرتز وباستعمال اثنين من المؤشرات الميكانيكية 0.2 و 0.6. بناء على ذلك، تم الحصول على أربع مجموعات للبيانات، تتكون كل مجموعة بيانات من 102 عينة (51 ميكروأومبولي غازية و 51 ميكروأومبولي صلبـة). يتم استغلال هذه البيانات لإنشاء عدد من الخصائص التمييزية المستخدمة في كشف وتصنيف الميكروأومبولي.

أولا، قمنا باستغلال طريقة محوِّل فوريه السريع وتقنيات الشبكات العصبية الاصطناعية باستخدام خصائص الترددات الأساسية والثانية الواردة في إشارة الموجات فوق الصوتية المرتدة بواسطة الميكروأومبولي. يسمح النهج المقترح بتصنيف الميكروأومبولي مع نسبة تمييز 92.85٪.

ثانيا، استخدمنا طريقة تحويل المويجات المنفصلة القائم على ثلاث خوارزميات لتخفيض الأبعاد : تقنية التطور التفاضلي، طريقة حِسَاب فيشر و تحليل المكونات الرئيسية باستخدام تقنية آلة الأشعة الحاملة في تحليل و وتصنيف إشارة الموجات فوق الصوتية المرتدة بواسطة الميكروأومبولي. بالإضافة إلى ذلك، نقترح إستراتيجية لاختيار مرشح المويجات المناسب من بين 59 مرشح. أظهرت النتائج التجريبية، استنادا إلى مرشح المويجة المختار وخوارزمية التطور التفاضلي، أن طريقة تحويل المويجات المنفصلة تحقق معدلات تصنيف أفضل (96.42٪) مقارنة بالنتائج المتحصل عليها في الطريقة السابقة باستخدام محوِّل فوريه السريع . أظهرت النتائج التي تم الحصول عليها أن إشارات الترددات الراديوية للموجات فوق الصوتية تجلب فرصا حقيقية للكشف عن الميكروأومبولي وتصنيفها.

To my dear mother and father.

Acknowledgments

I would like to acknowledge the support of PHC Tassili France-Algérie 2014 (14 MDU 909).

I am greatly indebted to my principal supervisor Professor Nabil Benoudjit for his continuous support and guidance throughout this project and for showing confidence in my work. He is always determined to help efficiently and promptly. He gave me the keys to organize the work in an efficient, accurate, creative and autonomous way.

The thesis would not have made possible without the help of my co-supervisor Professor Ayache Bouakaz. Special thanks for supporting my project right from the beginning and for providing a research environment in the INSERM U930 laboratory. I am particularly grateful for the time he spent with me during my stay in Tours, and for his interesting comments.

I would also like to thank Prof. Noureddine GOLEA, Prof. Abdellah KACHA, and Dr. Noureddine GHOGGALI for their participation to my thesis committee, and devoted their precious time to review my thesis. Profuse thanks go equally to Professor Lamir SAIDI for having agreed to preside this jury. I appreciate particularly the precise and efficient reviewing of the complete thesis they performed. I also want to thank you for letting my defense be an enjoyable moment, and for your brilliant comments and suggestions.

In the same way, I wish to thank M. Damien Fouan and all the members of the INSERM U930 laboratory for the help they provided.

I would like to acknowledge the Department of electronics at the university of Batna. My graduate experience benefitted greatly from the courses I took and the opportunities I had. I am grateful to all of those with whom I have had the pleasure to work during this and other related projects.

To my parents, a special word of appreciation, thank you for your unselfish, never-ending support and encouragement. It shall not be forgotten in any occasion. Your prayer for me was what sustained me thus far. I would also like to thank my brothers Issam and Yacine, and my sister Siham for their companionship through the journey of life.

My wife Malika and my daughter Amani – this is for you. Very warm thanks go to my wife who has been a major inspiration for me to venture into research and a driving force for me to complete it. I thank her for her daily encouragements and supports.

Finally, I would like to acknowledge friends and family for their encouragements and support.

Table of Contents

List of tables

Chapter I

Chapter II

Chapter IV

Chapter V

List of figures

Chapter I

Chapter II

Chapter III

Chapter IV

Chapter V

List of abbreviations

TCD:	Transcranial Doppler
RF:	Radio-Frequency
FFT:	Fast Fourier Transform
DWT:	Discrete Wavelet Transform
ES:	Embolic Signals
ANN:	Artificial Neural Network
MLP:	Multilayer Perceptron
RBFN:	Radial-Basis Function Network
RBF:	Radial-Basis Function kernel
DEFS:	Differential Evolution algorithm
PCA:	Principal Component Analysis
SVM:	Support Vector Machines
DVT:	Deep Vein Thrombosis
MI:	Mechanical Index
FDA:	US Food and Drug Administration
AI:	Artificial Intelligence
CM:	Confusion Matrix
AUC:	Area Under Curve
TP:	True Positive
TN:	True Negative
FP:	False Positive
FN:	False Negative
ACC:	Accuracy
r:	Recall or Sensitivity
Spe:	Specificity

P:	Precision
F:	F-measure
ROC:	Receiver Operating Characteristic Curve
THI:	Tissue Harmonic Imaging
ANN:	Artificial Neural Networks
RMS:	Root Mean Square
IP:	Instantaneous Power
EBR:	Ratio of the Embolic Signal to the Background Signal
TP2TR:	Total Power to the Threshold Ratio
RR:	Rise Rate
FR:	Fall Rate
VIE:	Variances of Instantaneous Envelope
VIF:	Variances of Instantaneous Frequency
OT:	Optimal Threshold

General Introduction

1. Definition of microemboli

Embolism is an intravascular migration of an insoluble body such as gas bubble, fat globule, blood clot, atheromatous plaque, or piece of thrombus. Embolic phenomena are still one of the leading causes of serious and sometimes life-threatening disorders in the developed and the majority of developing countries [1-7]. Since the 60s, ultrasound researchers have demonstrated that gas emboli can be detected using ultrasound waves. However, it was only in 1990s that it was revealed that solid emboli, composed of thrombus or platelet aggregates, could also be detected using ultrasound [8, 9].

It is believed that embolus (singular of emboli) composition (solid or gaseous emboli) is vital in predicting clinically significant complications [10]. For example, patients on bypass for open-heart surgery are known to encounter gaseous emboli but may also have some solid emboli due to pre-existing cardiovascular disease [10]. Most studies diagnose the risk to these patients by counting the number of emboli detected during surgery without considering how the composition might influence the outcome [11, 12]. These emboli can induce immediate damages like stroke or heart attack, thus the importance of an automatic detection and classification system.

In stroke, embolus detection using Transcranial Doppler (TCD) methods have shown their limits to distinguish between emboli and artifacts, and more importantly to make the differentiation between solid and gaseous microemboli using the backscattered TCD signals [13-16]. Radio-Frequency (RF) ultrasound signals backscattered by the emboli contain additional information on the embolus in comparison to the traditionally used Doppler signals [17]. Gaseous bubbles show a nonlinear behavior under specific conditions of the ultrasound excitation wave, this nonlinear behavior is exploited to differentiate solid from gaseous microemboli.

2. Aim of the thesis

As visual detection and analysis of microemboli Doppler signals by experts are subjective to observer's experience and also very time-consuming, development of computer-based decision support systems that intend to characterize particles whether solid or gaseous emboli is vital in the field of biomedical engineering. This thesis proposes an automatic detection and classification system of circulating microemboli in the bloodstream using Radio Frequency ultrasound signals instead of the traditionally used Doppler signals [18-24]. Due to resonance phenomenon, microbubbles interact actively with the excitation wave exhibiting a nonlinear scattering components. This nonlinear behavior is specific to gaseous emboli and cannot be related to solid emboli and therefore this characteristic can be exploited to characterize gaseous and solid emboli.

In order to verify the usefulness of Radio Frequency ultrasound signal processing for microemboli classification, an in vitro set-up is developed. To imitate the ultrasonic behavior of gaseous emboli, Sonovue micro bubbles are administered into a 200 ml volume of Isoton. A flow phantom containing a tube of 0.8 mm in diameter is exploited in order to approximate the size of a human vessel.

Since solid emboli present acoustic properties comparable to those of biological tissue, the tissue mimicking material surrounding the vessel is chosen to mimic the behavior of solid emboli. In order to reproduce real clinical pathological situations, Sonovue concentration are chosen such that the fundamental scattering from the tissue and from the contrast are identical. The backscattered signals are extracted using a commercially available ultrasound scanner [24].

In the first part of the thesis, we employ Fast Fourier Transform (FFT) and Artificial Neural Network (ANN) to study the nonlinear characteristics of gaseous emboli. The amplitudes and bandwidths of fundamental and 2nd harmonic components are selected as input parameters to two ANN models namely Multilayer Perceptron (MLP) and Radial-Basis Function Network (RBFN). Moreover, the frequency bandwidths of fundamental and 2nd harmonic echoes are approximated by gaussian functions and the coefficients are used as a third input parameter to the neural network models [24].

In the second part, we exploit discrete wavelet transform (DWT) to characterize the behavior of solid and gaseous emboli [25, 26 ,27]. However, the selection of an appropriate mother wavelet for the signal being analyzed is a vital criterion. Consequently, several wavelet functions are evaluated within a microemboli classification system. The effectiveness of the choice of the suitable mother wavelet in the evaluation of the proposed system is assessed [22]. Then, we employ DWT algorithm based on the selected wavelet function and dimensionality reduction techniques based on Differential Evolution Algorithm (DEFS), Fisher Score method, and Principal Component Analysis (PCA) in the analysis and the characterization of the backscattered RF ultrasound signals from the emboli using Support Vector Machines (SVM) classifier [18].

The main contribution of this thesis is twofold: first, we exploit Radio-Frequency (RF) ultrasound signals backscattered by the emboli instead of the traditionally used Doppler signals for the detection and classification of circulating microemboli in the bloodstream. Therefore, we develop an experimental set-up in order to mimic the ultrasonic behavior of gaseous and solid emboli.

Second, we implement signal processing and data mining techniques in order to create an automated microemboli detection and classification system. Involving methods are: FFT, DWT, ANN models (MLP and RBFN), and SVM. Furthermore, we compare the performances of three dimensionality reduction techniques; Differential Evolution algorithm (DEFS), Fisher Score method, and Principal Component Analysis (PCA).

3. Organization of the thesis

The thesis is divided into five chapters. The first part aims at introducing embolism problem and types. The causes of embolism are also highlighted in this section. Furthermore, we introduce the detection techniques and the nonlinear scattering properties of the interaction between ultrasound and gas bubble.

In chapter II, we present a literature review of artificial intelligence methods employed in this thesis. We illustrate three classification algorithms with main focus on: Multilayer Perceptron Neural Networks, Radial Basis Function Neural Networks, and Support Vector Machines. Furthermore, we describe the use of three dimensionality reduction techniques; Differential Evolution algorithm, Fisher Score method, and Principal Component Analysis.

Chapter III presents the experimental set-up realized as part of the cooperation project INSERM (France / Algeria DPGRF) 2007-2008 study and the TASSILI project (14 MDU 909) in the INSERM U930 laboratory at the University of François Rabelais Tours.

The results are presented in Chapters IV and V. In Chapter IV, we focused on the use of FFT approach in the detection and classification of microemboli by exploiting radio frequency signals backscattered by the emboli as an alternative of the commonly used Doppler signals. We employ Multilayer Perceptron and Radial-Basis Function Network models in the classification system.

In order to enlarge the range of the detection system, we investigate in Chapter V wavelet-based approach instead of FFT technique to detect and classify the emboli. Since the performance of the classification system greatly depends on the selection of the mother wavelet, we select the required wavelet filter experimentally among 59 mother wavelet functions. Furthermore, we propose a classification system of microemboli using dimensionality reduction techniques (DEFS, Fisher Score, and PCA algorithms), SVM as a classifier, and the backscattered RF signals. Moreover, the best results are compared to the FFT based neural network approach.

The last section of the thesis draws the conclusions and the perspectives of this experimental study.

Chapter I : Literature Review of Embolism

I.1 Introduction

To prescribe the appropriate treatment and reduce the risk of embolism, several ultrasonic methods using Doppler processing have been used for emboli detection and classification as solid or gaseous matter. Unfortunately, Doppler processing technique, which is commonly used for emboli detection, presents some limitations to distinguish between embolus and artifacts [13-16]. This chapter reports on the types of embolism, the detection techniques, and the interaction between microbubbles and ultrasound.

I.2 Types of embolism

Three general categories of embolism are identified: arterial, gas, and pulmonary embolism, the most common are pulmonary emboli.

I.2-1 Pulmonary Embolism

An embolus, generally formed in the leg, sometimes referred to as deep vein thrombosis (DVT), will lodge in one of the pulmonary arteries. Several emboli are dissolved by the organism and disappear spontaneously, however severe pulmonary embolism can cause death [28, 29] (refer to figure I.1).

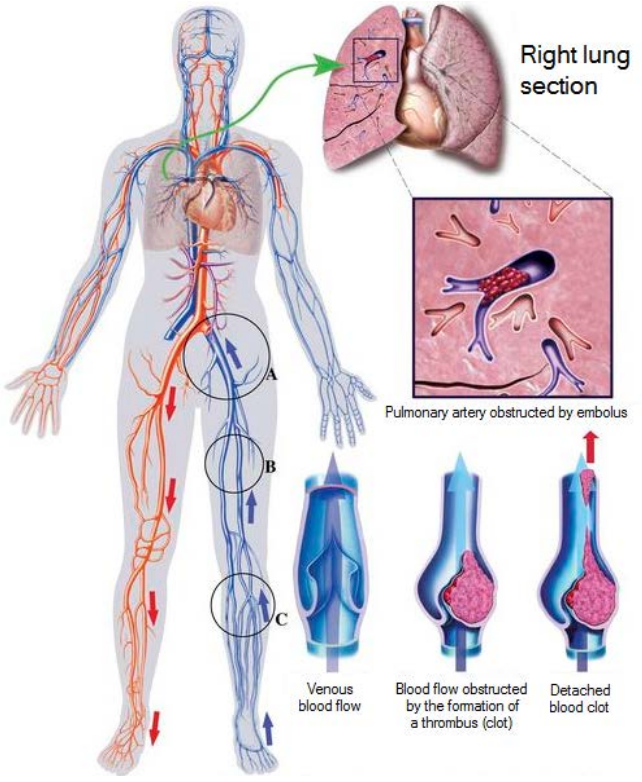

Figure I.1 Formation of a thrombus, A. hip, B. thigh, C. calf [29]

I.2-2 Arterial embolism

Arterial emboli are usually a complication of heart disease. It happens when the blood flow is blocked at the junction of major arteries [30-33]. If a blood clot travels to the brain, it causes a cerebral infarction or transient ischemic stroke which can be fatal [30]. Clots too small to plug a major artery may block the smaller blood vessels that feed the retina at the back of the eye. This results in a sudden loss of vision in one eye [31]. If fat particles or other particles from the bone marrow are introduced into the bloodstream, they can block blood vessels in the same way as a blood clot or air bubble [34].

I.2-3 Gaseous embolism

Underwater divers that rise too quickly to the surface can generate a gas embolism, caused by air bubbles in the blood that can block blood flow in the arteries. It may also occur during surgery and other medical procedures where small amounts of air often get into the blood circulation accidentally (for example a bubble entering an intravenous fluid line) [35].

This often leads to obstruction of blood flow through the heart and pulmonary edema (inflammation of the pulmonary blood vessels). Moreover, this may cause cerebral edema (inflammation of the brain) , heart failure, or stroke (refer to Figure I.2) [35].

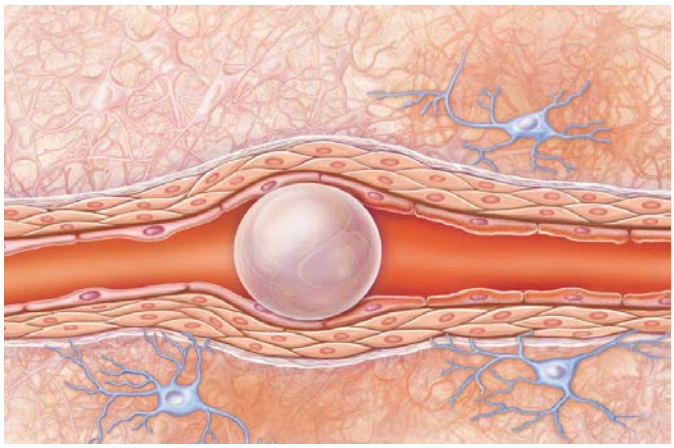

Figure I.2 Bubble Obstructing End-Arterial Flow in a Cerebral Vessel [36].

I.3 Causes of embolism

Most embolisms occur in people who have risk factors for the formation of blood clots, such as smoking or heart disease. For other types of embolism, risk factors include high cholesterol, high blood pressure, and atherosclerosis (the accumulation of fatty plaques in blood vessels). Arterial emboli are usually a complication of heart disease in which blood clots form in the heart's chambers. Rapid changes in environmental pressure that could happen when scuba diving or flying may produce Gas embolism.

The primary cause of most pulmonary embolism is deep vein thrombosis (DVT). It is a condition in which clots develop in the veins of the legs (refer to Figure I.1) [37]. Natural blood agents usually dissolve small clots without blocking. However, some clots are too large to be dissolved and large enough to block major blood vessels in the lungs or in the brain.

Any slowing down of blood flow in the legs can contribute to the formation of clots. A DVT or pulmonary embolus may develop in people who have remained motionless for a long period of time during a long-term flight or as a result of the immobilization of a leg by a plaster or prolonged bed rest without moving the legs. Other factors associated with DVT or pulmonary embolism include cancer, previous surgery, leg or hip fracture, or a genetic predisposition of blood cells that increases the risk of clot formation [29-37].

I.4 Detection techniques

The ultrasound community has experienced dramatic technical advances over the last decades, such as blood flow measurements with elaborate Doppler techniques or real time three-dimensional imaging with 2-D phase array transducers. This is partly ascribed to the advantages of ultrasound over other diagnostic modalities, including its low cost, real-time character and safety.

One of these recent ultrasound technologies is Transcranial Doppler (TCD). TCD is a non-invasive ultrasound method used to assess blood flow velocity in the major basal intracranial arteries on a real-time basis.

Doppler ultrasonography has been proposed for the detection of gas embolism since 1968. The development of transcranial Doppler in the 1980s has allowed wide clinical use in the study of decompression accidents and monitoring of surgical procedures (carotid surgery, extracorporeal circulation) and then in patients with prosthetic heart valves [38-40].

Currently, Transcranial Doppler based techniques rely on the appearance of high intensity transient signals, which are used as indictors of the presence of emboli [41] (Figure.I.3).

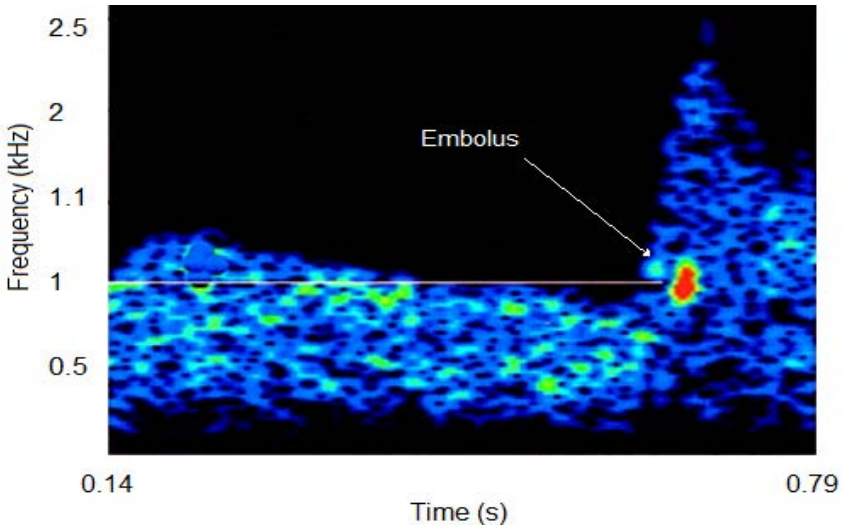

Figure I.3 Sonogram of micro-embolic Doppler signal [42].

Study by E. Roy et al. employed time-frequency representation using spectrogram in order to automatically detect the circulating embolus [43]. However, they stated that Doppler signals found in clinical applications are more complex than their Doppler signals and that their results are applicable just for their simulated signals.

Ping-Wing Lui et al. performed an experiment set up on seven dogs for the detection of venous embolic Doppler signals employing DWT [44]. The method is found useful in the detection of emboli, however the algorithm is not suitably applicable to small emboli detection since the emboli exploited in their study are bigger than the emboli discovered in human body.

Jean-Marc Girault et al. presented an emboli detection method based on parametric signal processing approaches. In their approach, they compared the Doppler embolic signal to its autoregressive model and then they constructed a decision information which contains the signature of the micro-embolus signal [45].

Nizamettin Aydin et al. employed discrete wavelet transform to investigate the transcranial Doppler audio signals for detection of embolic signals [25].

The results of these two approaches [25, 45] are promising however, the challenge remains to distinguish between emboli and artifacts, and more importantly to make the differentiation between solid and gaseous microemboli using the backscattered TCD signals [13-16], especially before performing interventional procedures for neuroprotection where the nature of the emboli is an important diagnostic criterion. This is the case during carotid endarterectomy and cardiac surgery where air and solid emboli are strongly intricate. They can be detected with TCD but it has been very difficult to distinguish solid from gaseous microemboli [13-16].

Solid emboli are potentially far more damaging than gaseous emboli and they imply different therapeutic strategies [4]. Indeed, gaseous emboli are considered as a risk indicator and their detection implies to seek for the cause of the emboli. However, when solid emboli are detected, an anticoagulant or antiaggregant treatment is usually administered.

Although a number of technological developments have been achieved in the microemboli detection area, it is still impossible to reliably distinguish gaseous from solid emboli using Doppler techniques [13-16]. Classification of gaseous and solid microemboli using Doppler approaches rely on the appearance of high intensity transient signal, which is used as indictor of the presence of embolus. However, there is a generally established strategy of rejection of low-intensity micro embolic signals [46]. Consequently, a priori rejection of these embolic signals (ES) may reduce the predictive value and the sensitivity of the whole process. A recent study has revealed that there is a considerable relationship between low and high-intensity micro embolic signals, suggesting that these rejected ESs, because of their low intensity, are real and can predict future occurrence of high-intensity ES [47].

Furthermore, Doppler based techniques are strongly affected by artifacts caused by patient moving the head, coughing, or any movement that causes displacement of the probe which can produce similar signals as solid emboli or gaseous emboli [48].

Therefore, we propose a new approach based on the analysis of backscattered Radio Frequency ultrasound (RF) signals instead of Doppler signals [18-24]. In order to verify the usefulness of Radio Frequency ultrasound signal processing for microemboli detection and classification, we develop an in vitro set-up. Sonovue micro bubbles are used to imitate the ultrasonic behavior of gaseous emboli. In order to approximate the size of a human vessel, a

flow phantom with a tube of 0.8 mm in diameter is exploited. The tissue mimicking material surrounding the vessel is chosen to imitate the behavior of solid emboli.

In order to accurately discriminate gaseous from solid emboli, we exploit the nonlinear characteristics of gaseous emboli under an ultrasound excitation. We employ Fast Fourier Transform (FFT) and artificial neural network for the detection and classification of micro emboli [24].

A number of researchers have reported that discrete wavelet transform (DWT) performs better than Fast Fourier Transform for the analysis and the detection of embolic signals [25, 26, 27]. Therefore, we employ a DWT approach and a dimensionality reduction technique based on differential evolution algorithm, Fisher Score method, and PCA for the analysis of the backscattered RF ultrasound signals from the emboli [18].

I.5 Interaction Ultrasound Gas Bubble

I.5-1 Ultrasound contrast agents

Since the 1970s, researchers have tried to find ways to enhance the ultrasound signal backscattered from blood vessels. The answer has been found in the introduction of small air bubbles, which are at the origin of an increase in reflection. In 1968, Gramiak and Shah observed an enhancement of the echo returned by the blood following the injection of solutions such as green indocyamine, physiological saline, or alkaline serum into the vascular network [49]. This enhancement, which increases the contrast of the image, is a result of the presence of highly echogenic gas bubbles in the injected solution due to their density and compressibility which are very different from those of the blood. Another factor contributing to the enhancement of the collected echo is due to the resonant nature of the gas bubbles subjected to an ultrasonic beam.

However, the use of these primary contrast products was limited by their very short lifetime, once injected, these microbubbles disappeared relatively quickly, not allowing adequate examination (less than one second) in addition to their uncontrollable and inappropriate size preventing their passage through the pulmonary capillaries.

In order to allow optimal use of contrast agents, microbubbles must fulfill certain conditions: they must be administered intravenously and they must be sufficiently small and stable to ensure a lung passage and their lifetime must be long enough to allow ultrasound examination and image acquisition. In order to behave as a perfect tracer, microbubbles must also exhibit the same flow dynamics as blood. In order to comply with these specifications, the physical properties must be carefully selected. These properties concern the diameter of the microbubbles, the physical characteristics of their envelops, and the properties of the gas that composes them. In addition, consideration should be given to the effects of the surrounding environment, such as temperature and hydrostatic pressure [17].

For two decades efforts have been made to develop more stable and smaller contrast agents. Microbubbles composed of heavy gases were then developed to decrease their rate of dissolution in the blood and increase the duration of the examination (a few minutes). In addition, the gas bubble is surrounded by an envelope composed of proteins, phospholipids, surfactants, or polymers in order to protect it. Finally, the developed contrast agents are: non-toxic, non-allergenic, easy to apply (injectable through the peripheral vein), small enough to be able to cross the pulmonary barrier (<8μm), and have a lifetime for ultrasound examination [17].

The first commercialized second-generation ultrasound contrast agents fabricated was Optison (1997). It was later followed by other types of agents, such as; Definity (2001), Sonovue (2001), Luminty (2006), Sonazoid (2007), and Lumason (2014). Over the years, several other agents were developed. However, various types are no longer in production. Table I.1 illustrates the commercial contrast agents currently in clinical use [50].

Sonovue and Lumason consist of microspheres with an outer lipid shell that encapsulates sulfur hexafluoride gas. These types of ultrasound contrast agents are produced by Bracco Imaging S.p.A (Milan, Italy) and they are currently marketed in Europe, North America, Australia, and parts of Asia and South America. These agents can be administered by either bolus or infusion [51].

Table I.1 Currently marketed ultrasound contrast agents [50].

Brand name	Manufacturer	Approved year	Inner gas	Outer shell	Marketed in
Optison	GE Healthcare	1997	Perflutren	Albumin	*USA, Europe*
Definity/Luminity	Lantheus Medical Imaging	2001/2006	Perflutren	Lipid	*USA, Canada, Europe, Australia, parts of Asia*
Sonovue/Lumason	Bracco Imaging S.p.A	2001/2014	Sulfur hexafluoride	Lipid	*North America, New Zealand, Europe, Brazil, parts of Asia*
Sonazoid	GE Healthcare	2007	Perflubutane	Lipid	*Japan, South Korea*

I.5-2 Microbubbles-Ultrasound interaction

The ultrasonic contrast agents modify the physical properties of the tissues and thus the behavior of the ultrasonic waves which pass through them. The mechanism of action associates, to different degrees according to the agents, an increase in the intensity of the backscattered ultrasonic beam, an attenuation of the ultrasound beam, and a decrease in the ultrasound speed. The main effect used by the ultrasonic contrast agents is the increase in the intensity of the backscattered ultrasonic field [17]. This backscattering can be classified into two categories: passive and active. The microbubble passively reflects the incident wave due to the difference in acoustic impedance between the surrounding environment (tissue, water) and the microbubble (gas).

In addition to passive backscattering, the microbubble acts as an active reflector by itself becoming a source of ultrasound. Under ultrasonic wave excitation, the microbubble is submitted to volumetric pulsations. In the simplest case, the size of the microbubble decreases during the compression phase of the ultrasonic wave (positive pressure) and increases during the decompression phase of the wave. The size variations of the microbubble depend on the frequency of the incident wave and are maximum for the resonance frequency. This resonance phenomenon is very important because the resonant microbubble significantly increases the amplitude of the reflected signals [17, 52].

Due to the resonance phenomenon, microbubbles do not respond in the same way to ultrasonic excitations as tissues. Indeed, the microbubbles interact actively with the excitation process. This interaction depends on several parameters, in particular the negative pressure of rarefaction and the incident frequency. The response of the microbubble can thus be separated into three acoustic regimes. For low acoustic pressures, the compression and expansion of the microbubble are symmetrical and of small amplitude. Thus, the size of the microbubble varies slightly but linearly with the amplitude of the acoustic pressure. For higher acoustic amplitudes, the compression of the microbubble is smaller than its expansion. As the rigidity of the microbubble varies locally as a function of the compression and expansion phases, the expansion of the microbubble is then easier than its compression (refer to Figure I.4). This difference in the elastic behavior of the microbubble during the compression and expansion phases generates an asymmetry in its response, characteristic of the generation of nonlinear frequency components, called harmonics (refer to Figure I.5). For higher acoustic pressures, the microbubbles are destroyed [17, 53, 54].

The spectrum of the echo clearly shows a nonlinear component produced at twice the incident frequency, i.e. at 8 MHz. This nonlinear frequency component, called the second harmonic, has a relatively small amplitude compared to the fundamental component (refer to Figure I.5) [17].

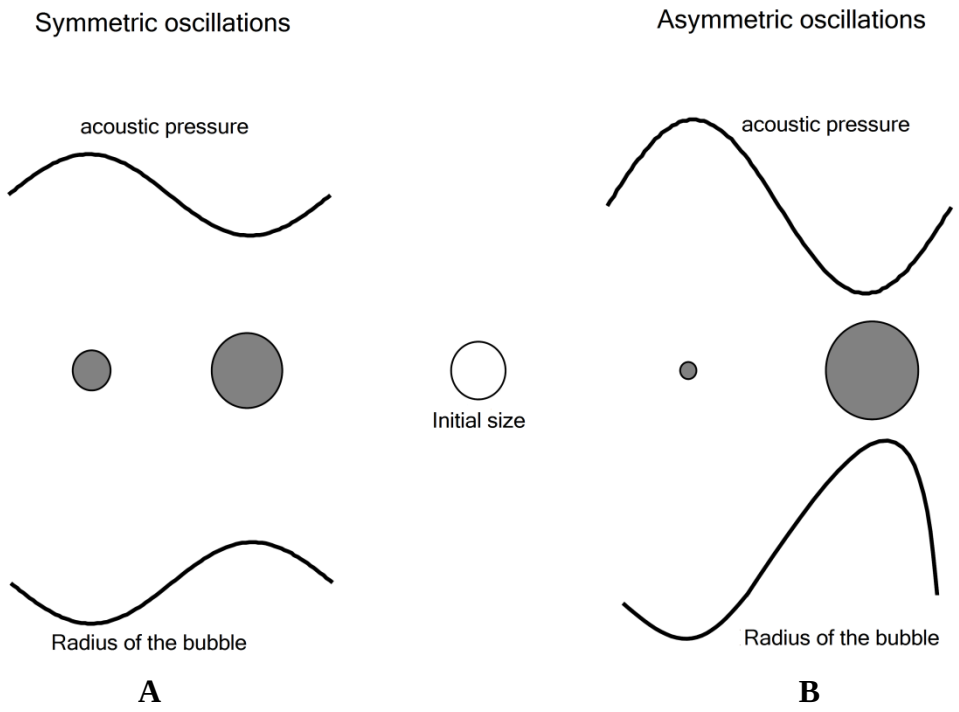

Figure I.4 Oscillations of a bubble subjected to a pressure wave; **A)** symmetrical (linear) oscillations, **B)** asymmetrical (nonlinear) oscillations adopted for this study form [17].

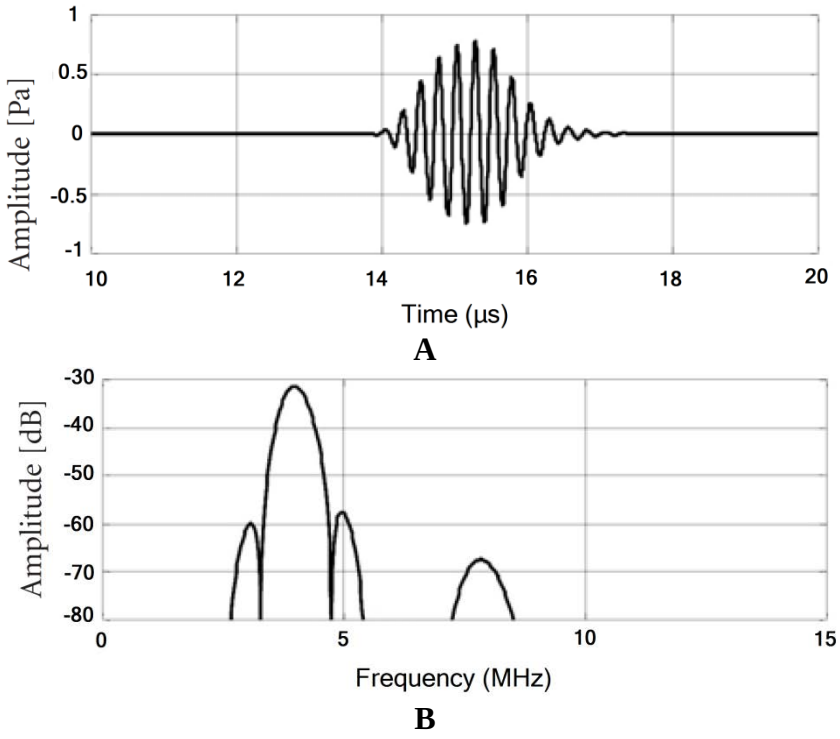

Figure I.5 Acoustic response of a microbubble of 1 μm of initial radius to a wave of 4 MHz of frequency and 5 kPa of amplitude: A) temporal response; B) frequency response adopted for this study form [17].

I.5-3 Mechanical index (MI)

Mechanical index (MI), defined as a safety measure and imposed on ultrasound scanner manufacturers by the US Food and Drug Administration (FDA), expresses the amount of mechanical work performed on a microbubble during half of an ultrasonic period. MI is defined as the negative pressure in megapascal divided by the square root of the ultrasonic frequency in megahertz. Depending on the recommendations for ultrasound use, this index is between 0 and 1.9.

$$MI = \frac{P\_\ (MP)}{\sqrt{f\ (MHz)}}, \qquad (I.1)$$

where $P\_$ is the peak negative pressure (in MPa) of the ultrasound wave at the point of interest, f is the center frequency of the transmitted ultrasound wave (in MHz).

Available MI on ultrasound scanners corresponds to the maximum value of acoustic pressure in the focal length of the probe. Nevertheless, this pressure is not constant on the whole image and varies considerably according to depth and to radial distance.

Figure I.6 summarizes the different microbubble responses and the corresponding acoustic excitations. In fact, these acoustic zones overlap each other according to the type of contrast agents and are therefore not easily separable. These acoustic excitations are grouped according to the acoustic pressure of the ultrasonic field, incident produced by the ultrasound scanner or as a function of MI. At low mechanical indexes, the microbubbles reflect linearly but provide a substantial improvement in ultrasonic echo from the blood vessels, mainly in the Doppler mode. Nevertheless, this mode of imaging, called fundamental or conventional mode, is being used less and less because of its limitations in several applications. When the intensity of the ultrasonic field is increased, at mechanical indexes greater than 0.1, the microbubbles behave nonlinearly generating harmonic frequency components.

These pressures are high enough to induce microbubbles in stable nonlinear vibrations without destroying them. In this regime, the components generated by the microbubbles are stationary nonlinear components and the selective detection of these components represents the basis of the harmonic imaging. This mode has now become the default imaging mode in contrast ultrasonography [17].

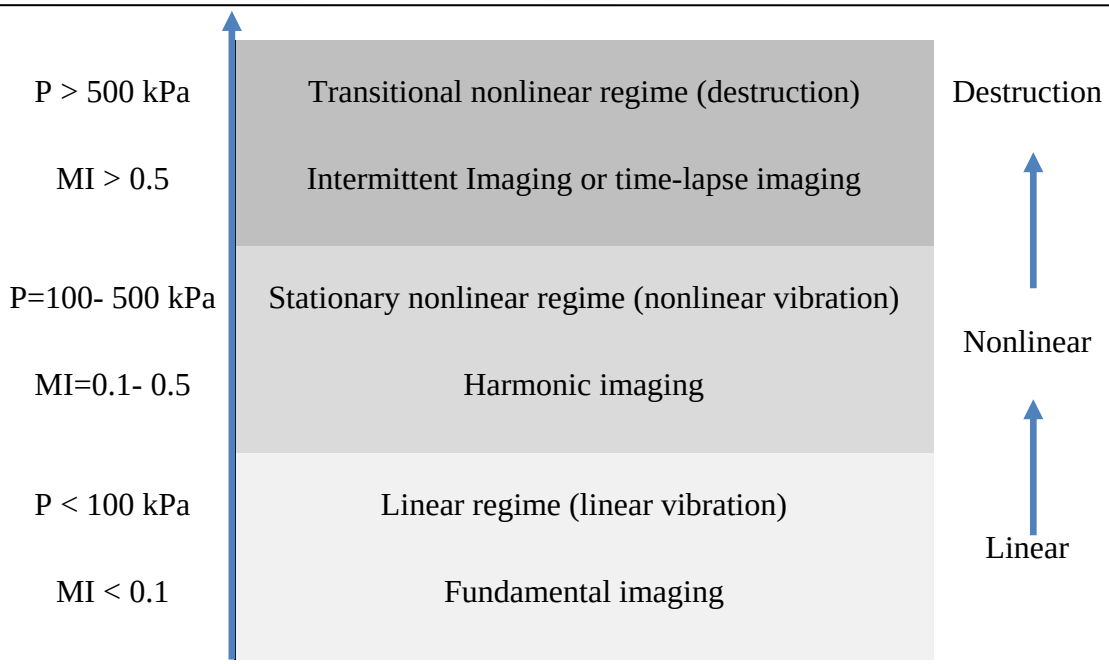

Figure I.6 Acoustic bubble regimes according to the mechanical index [17].

At higher mechanical index (mechanical index above 0.5), the destruction of the microbubbles under the ultrasonic beam is observed. Although the destruction of microbubbles is avoided in most imaging modes, it is also exploited in other applications [55].

I.6 Conclusion

This chapter presents the major types of embolism as well as the current techniques employed for classification of circulating microemboli in the bloodstream. The traditional techniques are largely based on the Doppler techniques. Unfortunately, these methods have shown some limitations to determine clearly the nature of circulating microemboli. Consequently, we propose in the following chapters another approach based on the analysis of radio frequency (RF) ultrasound signals instead of Doppler signals for the detection and classification of circulating microemboli by exploiting the nonlinear behavior of gaseous bubbles.

Chapter II : Literature Review of Artificial Intelligence Methods

II.1 Introduction

Man's intelligent behavior is due in part to his ability to select, classify, and abstract significant information reaching him from his environment by way of his senses. Artificial Intelligence (AI), otherwise known as machine learning or computational intelligence is the science and engineering of creating intelligent machines designed in a way to make computers perform tasks that were earlier thought of human intelligence involvement. AI facilitates and replicates actions and decisions of humans without human shortcomings, such as fatigue, emotion, and limited time. Typically, artificial intelligence techniques use training samples in order to build a model that enables reliable predictions. In this chapter, we present a literature review of artificial intelligence methods employed in this thesis.

II.2 Classification

Classification of data is considered as one of the most vital tasks in real world problems with the objective of finding the underlying patterns of the data and making use of the found patterns [56]. The objective of classification is to predict a class label for an unclassified input. Classification consists of two stages: (i) Model construction; in which the classifier is built by analyzing and learning from the training set. (ii) Model usage; the classifier is used to determine what specific class is assigned to a new input. In this thesis, the evaluation of the classification performances is carried out using cross validation technique.

II.2-1 Model selection (Cross-validation)

Cross-validation is a machine learning method that can be used to select the optimal parameters for a classifier while preventing overfitting the classifier to the training data [57]. We use hold-out-set cross-validation strategy to fix the parameters of the classifiers. While there are other validation techniques, including, but not limited to, bootstrap and leave-one-out, we focus on the more commonly used cross-validation approach in this thesis [57]. Hold-out-set cross-validation works by randomly dividing the dataset, into two subsets learning set and test set (hold-out-set). the testing set is hidden for the most part of the process and it is only used to check the final performance. After that, we randomly generate new training and validation sets from the initial learning set. The classifier parameters that results in a model with highest accuracy, using the validation set, are picked as the best choice of the classification problem (refer to figure II.1). Once the optimal parameters are fixed, the test set is used to validate the selected model.

The experimental evaluation is performed using hold-out-set to avoid overfitting and assure statistical validity of the results [57]. The test set is used only for the assessment of the model selected by the cross-validation algorithm. Therefore, the algorithm has only access to the training and validation sets, the test set is kept unseen in the selection process of the best model.

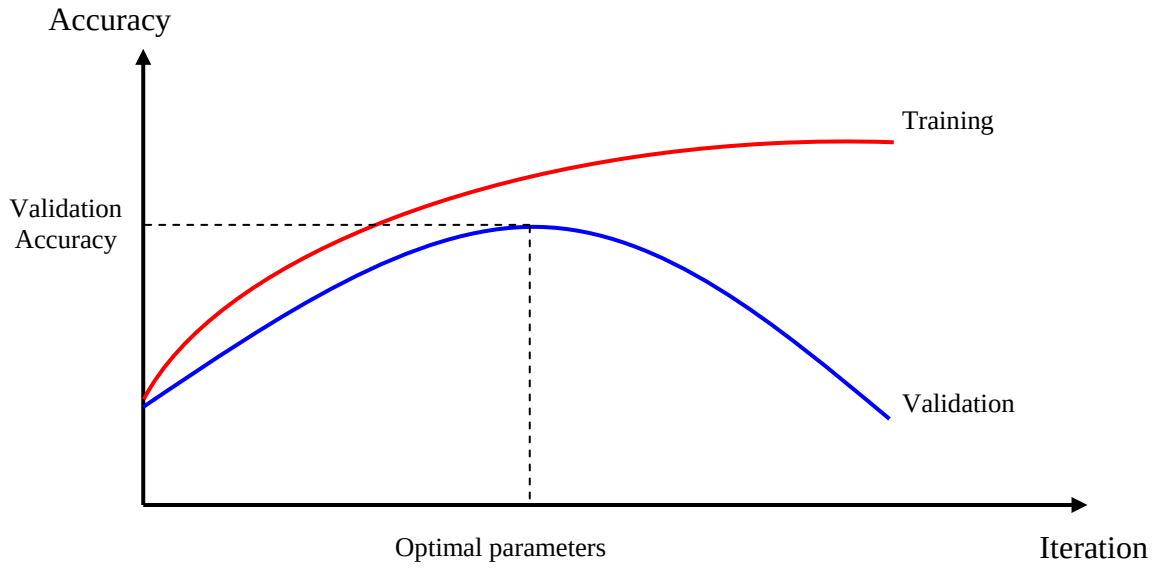

Figure II. 1. Optimal parameters using Cross validation strategy.

In our case, the experimental dataset consists of four acquisitions, each contains 102 samples (51 solid embolus and 51 gaseous embolus). In order to evaluate the predictive ability of a model, we randomly divide the dataset, into three subsets training set, validation set, and test set. The test set, approximately one-third (1/3) of the data (14 solid embolus and 14 gaseous embolus), is used only for the assessment of the model selected by the cross-validation technique, while the rest of the data will belong to the learning set (used for building the models) which will be divided into a training set (approximately two-third) and a validation set (approximately one-third). The validation set is used to tune the classifiers parameter.

In this thesis and in order to evaluate the performance of the proposed system, we employ three types of classification algorithms: Multilayer Perceptron (MLP), Radial Basis Function Neural Networks (RBFN), and Support Vector Machine (SVM). In the next three subsections, we briefly recall the basis of MLP, RBFN, and SVM models.

II.2-2 Multilayer Perceptron Neural Networks

The most widely used neural classifier today is Multilayer Perceptron (MLP) network which has also been extensively analyzed and for which many learning algorithms have been developed. MLP belongs to the class of supervised neural networks. MLP networks are general-purpose, flexible, and nonlinear models consisting of a number of units organized into multiple layers. The complexity of MLP network can be changed by varying the number of layers and the number of units in each layer. Given enough hidden units and enough data, it has been shown that MLPs can approximate virtually any function to any desired accuracy. In other words, MLPs are universal approximators [58, 59].

The multi-layer perceptron neural network model consists of a network of processing elements or nodes arranged in layers. Typically it requires three or more layers of processing nodes: an input layer which accepts the input variables used in the classification procedure, one or more hidden layers, and an output layer with one node per class, which in this thesis two classes (gaseous and solid embolus). The principle of the network is that when data from an input pattern is presented at the input layer the network nodes perform calculations in the successive layers until an output value is computed at each of the output nodes. This output signal should indicate which is the appropriate class for the input data i.e. we expect to have a high output value on the correct class node and a low output value on all the rest. Every processing node in one particular layer is usually connected to every node in the layer above and below. The connections carry weights which encapsulate the behavior of the network and are adjusted during training. The operation of the network consists of two stages. The ``*forward pass*" and the ``*backward pass*" or ``*back-propagation*". In the ``*forward pass*" an input pattern vector is presented to the network and the output of the input layer nodes is precisely the components of the input pattern. For successive layers the input to each node is then the sum of the scalar products of the incoming vector components with their respective weights. That is the input to a node *j* is given by [58].

$$input_j = \sum_i w_{ji} out_i \ , \qquad \text{(II.1)}$$

where w_{ji} is the weight connecting node *i* to node *j* and out_i is the output from node *i*. The output of a node *j* is

$$out_j = f\left(input_j\right), \qquad \text{(II.2)}$$

Which is then sent to all nodes in the following layer. This continues through all the layers of the network until the output layer is reached and the output vector is computed. The input layer nodes do not perform any of the above calculations. They simply take the corresponding value from the input pattern vector. The function $f(x)$ denotes the activation function of each node. A sigmoid activation function is frequently used,

$$f(x) = \frac{1}{1+\exp(-x)}, \tag{II.3}$$

where x is $input_j$.

The multi-layer feed-forward neural network is trained by supervised learning using the iterative back-propagation algorithm. In the learning phase a set of input patterns, called the training set, are presented at the input layer as feature vectors, together with their corresponding desired output pattern which usually represents the classification for the input pattern. Beginning with small random weights, for each input pattern the network is required to adjust the weights attached to the connections so that the difference between the network's output and the desired output for that input pattern is decreased. Based on this difference the error terms or δ terms for each node in the output layer are computed. The weights between the output layer and the layer below (hidden layer) are then adjusted by the *generalized delta rule* [58].

$$w_{kj}(t+1) = w_{kj}(t) + \eta(\delta_k out_k), \tag{II.4}$$

where $w_{kj}(t+1)$ and $w_{kj}(t)$ are the weights connecting nodes k and j at iteration $(t+1)$ and t respectively, η is a learning rate parameter. Then the δ terms for the hidden layer nodes are calculated and the weights connecting the hidden layer with the layer below (another hidden layer or the input layer) are updated. This procedure is repeated until the last layer of weights has been adjusted. The δ term in Equation II.5 above is the rate of change of error with respect to the input to node k, and is given by:

$$\delta_k = (d_k - out_k) f'(input_k), \tag{II.5}$$

for nodes in the output layer, and:

$$\delta_j = f'(input_k) \sum_k \delta_k w_{kj}, \tag{II.6}$$

for nodes in the hidden layers, where d_k is the desired output for a node *k.* The back-propagation algorithm is a gradient descent optimization procedure which minimizes the mean square error between the network's output and the desired output for all input patterns *P.*

Several studies applied MLP neural networks in the diagnosis of emboli. D. Shanthi, et al. used MLP in predicting the Thrombo-embolic stroke disease for 50 patients who have symptoms of stroke disease [60], they obtained an overall predictive accuracy of 89%.

S. Matos et al. employed Multilayer Perceptron Neural Networks for the classification of cerebral embolic signals using transcranial Doppler ultrasound. The results obtained in this study show that the MLP based approach is a suitable tool for characterizing cerebral embolic signals [61].

Tourassi, G. D. et al. investigated the use of three-layer perceptron neural network as a computer-aided diagnostic tool for predicting pulmonary embolism from ventilation-perfusion lung scans and chest radiographs. The results illustrated that MLP neural network can be trained to successfully perform the diagnostic task [62].

II.2-3 Radial Basis Function Neural Networks

Radial-basis function neural networks can be used for a wide range of applications mainly due to the fact they can approximate any regular function and their training is faster compared to the multilayer perceptron [63]. The training of RBFN networks can be split into an unsupervised part and a linear supervised part. Unsupervised updating techniques are straightforward and relatively fast. Moreover, the supervised part of the learning invokes solving a linear problem. Therefore, it is fast and it avoids local minima encountered when using the multilayer perceptron [24, 63-65]. RBFN consists of an input layer, a hidden layer (radial basis function layer), and an output layer [66].

A RBFN network is a two-layered ANN and it is defined as:

$$\hat{f}(\mathrm{x}) = \sum_{j=1}^{K} \lambda_j \phi_j \left(\left\| \mathrm{x}_i - \mathrm{c}_j \right\| \right), \qquad \text{(II.7)}$$

where

$$\phi_j\left(\left\|\mathbf{x}_i - \mathbf{c}_j\right\|\right) = \exp\left(-\frac{1}{2}\left(\frac{\left\|\mathbf{x}_i - \mathbf{c}_j\right\|}{\sigma_j}\right)^2\right). \quad \text{(II.8)}$$

According to Equations II.7 and II.8, the model is characterized by three types of parameters. The c_j are called centers (centroids), they are chosen into dense regions of the input space, via a vector quantization technique [63, 67]. The number *K* represents the number of centers in the hidden layer while σ_j is the width (spread) of each center. The centers c_j are chosen regardless of the outputs $f(x) = 0$ (gaseous embolus) or $f(x) = 1$ (solid embolus), the choice of c_j is based only on the properties of the distribution of the inputs space x. Finally, the weights λ_j between the hidden layer and the output layer are found by linear regression analysis (by minimizing the mean squared difference between the network's output and the desired output value) [63].

The input nodes in the input layer are equal to the dimension of the input vector. The optimal number of neurons in the hidden layer as well as the spread of the RBFN Gaussian are determined experimentally using cross validation technique. The combination (number of neurons in the hidden layer, spread of the RBFN Gaussian) that results in a model with highest validation accuracy is picked as the best choice of the classification problem. Once the optimal parameters are fixed, the test set is used to validate the selected RBFN model.

Radial Basis Function Neural Networks have been used in Several studies for characterizing micro emboli.

Adem Karahoca, et al. performed an embolic signal detection system using a data set obtained with Doppler signals including 100 embolic signals, 100 speckle, and 100 artifacts. The results indicated that Radial Basis Function Neural Networks provides better classification rates than MLP [68].

N. Benoudjit, et al. conducted an experimental comparative study of microemboli classification based on radio frequency signals using Multilayer Perceptron (MLP) and Radial-Basis Function Network (RBFN). The results demonstrate the opportunity to classify emboli based on neural network analysis and Radio Frequency ultrasound signals instead of Doppler signals [24].

II.2-4 Support Vector Machines

Support Vector Machine (SVM) [69] is a novel machine learning technique based on a statistical learning theory proposed by Vapnik's group in 1995. SVM has gained increasing attention in areas that range from pattern recognition to regression estimation due to its remarkable learning performance. On the basis of the structural risk minimization principle [70], SVM can improve the generalization ability of a learning machine. At the same time, an optimization problem can be transformed into a convex quadratic programming problem. The solution of a quadratic programming problem is the unique optimization solution of the whole. Hence, SVM does not have the problems with local extrema that are present for traditional neural networks, which require large numbers of training samples.

SVM performs pattern recognition for two classes problems by determining the hyperplane of separation $w.x+b=0$ that best separates the two classes with the maximum distance $\frac{2}{\|w\|}$ to the narrowest points (support vectors) (refer to Figure II.2) [69, 71].

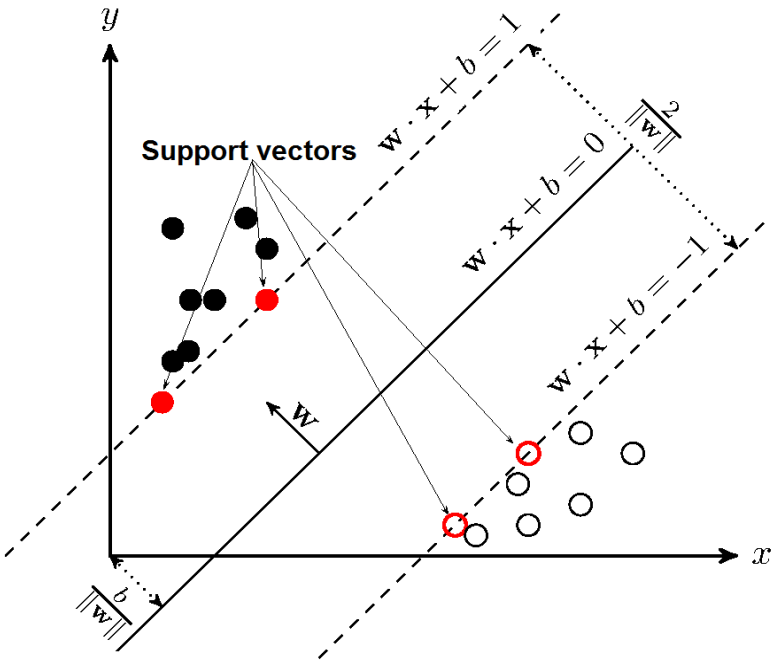

Figure II. 2. Separation of two classes by SVM.

where $\frac{b}{\|w\|}$ is the offset of the hyperplane from the origin along the normal vector.

Figure II.2 shows the hyperplane of separation and margins for an SVM trained with samples from two classes. Samples on the margin are called the support vectors. *M* (margin) is the distance from the hyperplane to the closest point for both classes of data points [71]. SVM is originally designed for linear binary classification. In practice, several applications of SVM are nonlinear classification problems. For nonlinear classification problems, we can use nonlinear transforms. A transformation, $\Phi(x)$, maps the data from the input space to a feature space that allows linear separation. One then seeks the optimization separation plane in feature space in addition to an inner product operation within the feature space. The inner product operation may be implemented by function (called a kernel function). In SVM, we introduce a kernel function $K(x_i, x_j)= \Phi(x_i) \bullet \Phi(x_j)$ to perform the transformation [72,73]. Then the basic form of SVM can be obtained [72,73]:

$$f(x)=\sum_{i=1}^{l}\alpha_i y_i K(x_i, x_j)+b. \qquad \text{(II.9)}$$

where $\alpha=[\alpha_1, \alpha_2, ..., \alpha_l]$ is the vector of Lagrange multipliers and $K(x_i, x_j)$ is a kernel function. In SVM literature, several kernels functions such as linear, polynomial, and radial basis function (RBF) are introduced. In our case, radial basis kernel is used to differentiate between gaseous and solid embolus and it is given as below:

$$K(x_i, x_j)=\exp\left(-\gamma \left\| x_i - x_j \right\|^2\right). \qquad \text{(II.10)}$$

where γ is the width of RBF kernel function. More details about recent developments of SVM can be found in [74].

The kernel parameter γ and the penalty parameter C are the two major parameters of the RBF applied in SVM-RBF which have to be set appropriately in order to improve SVM learning. γ is the width of RBF kernel. C is the regularization parameter of error which allows one to trade off training error vs. model complexity.

In this thesis, γ and C are optimized using grid search algorithm [75]. The evaluation of the classifier performances is carried out using hold-out-set cross validation technique. We carried out experiments by trying exponentially growing sequences of C and γ ($C = 2^{-3}, 2^{-2}, ..., 2^9, 2^{10}$, $\gamma = 2^{-3}, 2^{-2}, .., 2^4, 2^5$) [75]. For each pair of (C, γ) we train the SVM classifier with the training data, and then we use the SVM to classify the validation data. The combination that results in a model with highest validation accuracy is picked as the best choice of the

classification problem. Therefore, the algorithm only has access to the training and validation sets, the test set is kept unseen in the selection process of the best model. The testing accuracy is obtained by applying the selected SVM model on the testing data.

Support vector machines classifier has been exploited in several emboli characterization systems using transcranial Doppler signals. G. Serbes, et al. proposed an emboli detection system using Doppler ultrasound signals recorded from both forward and reverse flow of blood, the highest performance where achieved when they exploited SVM in the classification process [76].

N. Ghazali, et al. used a transcranial Doppler (TCD) system simulator for the classification of microembolus from the background signal of three virtual patients. They obtained a classification performance of 83.04% using SVM as a classifiers and principal component analysis as a dimensionality reduction technique [77].

F. Douak, et al. proposed an experimental study, in which a wavelet optimization approach for microemboli is conducted using RF signals, genetic algorithm, and SVM classifier [19].

K. Ferroudji, et al. proposed an empirical mode decomposition system for the detection and classification of microemboli using RF signals and SVM [20]. Furthermore, the authors used FFT approach and a Non-linear Kernel Support Vector Machines for microemboli classification using RF signals [21]. Then, they suggested a strategy to select the suitable wavelet filter among 59 mother wavelet functions for microemboli classification using SVM and the same RF signals, the results indicate that Daubechies 6 is the most appropriate wavelet function for this application [22].

II.3 Dimensionality Reduction

The performance of machine learning methods relies heavily on how well the characteristics of signals are represented by a feature vector. This step may provide a high dimensional feature vector; such feature vector is normally too large to be handled properly by a classifier during training thus the need of a dimensionality reduction method.

The main reasons for using a dimensionality reduction algorithm are explained by:

- The need to reduce number of features in order to eliminate poor features by reducing pairwise correlation and perform a more accurate training and an optimal classification.
- The limitation of the training set: high dimensional data requires a very large number of training data to uncover and optimally estimate the model parameters for classification.
- The decrease of the learning and prediction computational complexity.

In sight of these requirements, and to overcome the "curse of dimensionality", we perform two approaches of dimensionality reduction techniques: feature selection and feature generation.

Dimensionality reduction can be performed either by removing feature closely related with other feature in the dataset (feature selection), or combining features to create a smaller set of features while minimizing the information loss (feature generation). In either case, the goal is to find a low-dimensional representation of the data that preserves (most of) the information.

The feature selection methods performed in this thesis are Differential Evolution algorithm (DEFS), and Fisher score algorithm. Feature generation is achieved by the use of principal components analysis.

Feature selection techniques usually fall into three main categories; filter, wrapper, or embedded methods. Filter approaches perform feature selection using the intrinsic properties of the data independently of the learning algorithm. Wrapper approaches conduct feature selection using a learning algorithm as part of the evaluation function to estimate the

relevance of a given set of features, in embedded approaches the search for an optimal set of features is built into the learning algorithm construction [78].

II.3-1 Feature selection

II.3-1.1 Differential Evolution algorithm

Differential Evolution algorithm (DEFS) is a wrapper dimensionality reduction technique. DEFS algorithm is a population-based stochastic search method, it belongs to the family of evolutionary algorithms, it was initially proposed by Storn and Price in 1995 [79, 80].

Later it has been successfully applied to a large number of problems such as remote sensing images [81], classification rule discovery [82], and features selection [83]. To solve an optimization problem, DEFS starts by iteratively modifying a randomly generated initial population of candidate solutions using of floating-point encoding instead of binary numbers [84]. This process is then enhanced using selection, mutation, and crossover operations (refer to Figure II.3). DEFS combines different, randomly chosen populations (X_{r0}, X_{r1} and X_{r2}) to create a mutant element ($V_{i,g}$) from the current generation g:

$$V_{i,g} = X_{r0,g} + F \times (X_{r1,g} - X_{r2,g}), \tag{II.11}$$

where $F \in (0,1)$ is a scale factor that controls the rate at which the population evolves.

In addition, DEFS also uses discrete recombination (crossover), in order to construct trial vectors out of parameter values that have been copied from two different populations.

$$U_{j,i,g} = \begin{cases} V_{j,i,g} \; if \; rand(0,1) \leq C_r \; or \\ \qquad X_{j,i,g} \; Otherwise \end{cases} \tag{II.12}$$

$U_{j,i,g}$ is the j^{th} trial element along i^{th} dimension from the current population g.

$C_r \in [0, 1]$ is the crossover probability which controls the fraction of parameter values that are copied from the mutant.

If the newly generated element results in a better fitness (classification accuracy) than the predetermined population member, then the resulting element replaces the vector with which it was compared.

The block diagram of the used DEFS algorithm is shown in Figure II.3, and it is defined by the following steps:

• Generate new population elements from the original population.

- Create a new mutant vector for each position in the population matrix.
- A trial vector is obtained by crossing the mutant vector with the original vector.
- The corresponding position in the new population will contain either:
  - The trial vector or its corrected version
  - or the original target vector depending on which one of them achieved a better fitness.
  - The process is repeated until each of the population elements have competed against a randomly generated trial element
- Generate new population elements from the original population.

A roulette wheel weighting scheme is utilized [85] to prevent two dimensions from settling at the same feature coordinates. This is achieved using a features distribution factor to aid in the replacement of the duplicated features which gives higher weights to features that make enhancement in the pending iteration compared with the previous one. Furthermore, it aims to keep features that are relevant in the two iterations, even without making any improvement [84].

Once the last trial element has been evaluated, the survivors of the population pairwise competitions become parents for the next generation in the evolutionary cycle. For further details on the above DEFS method, please refer to [83, 86].

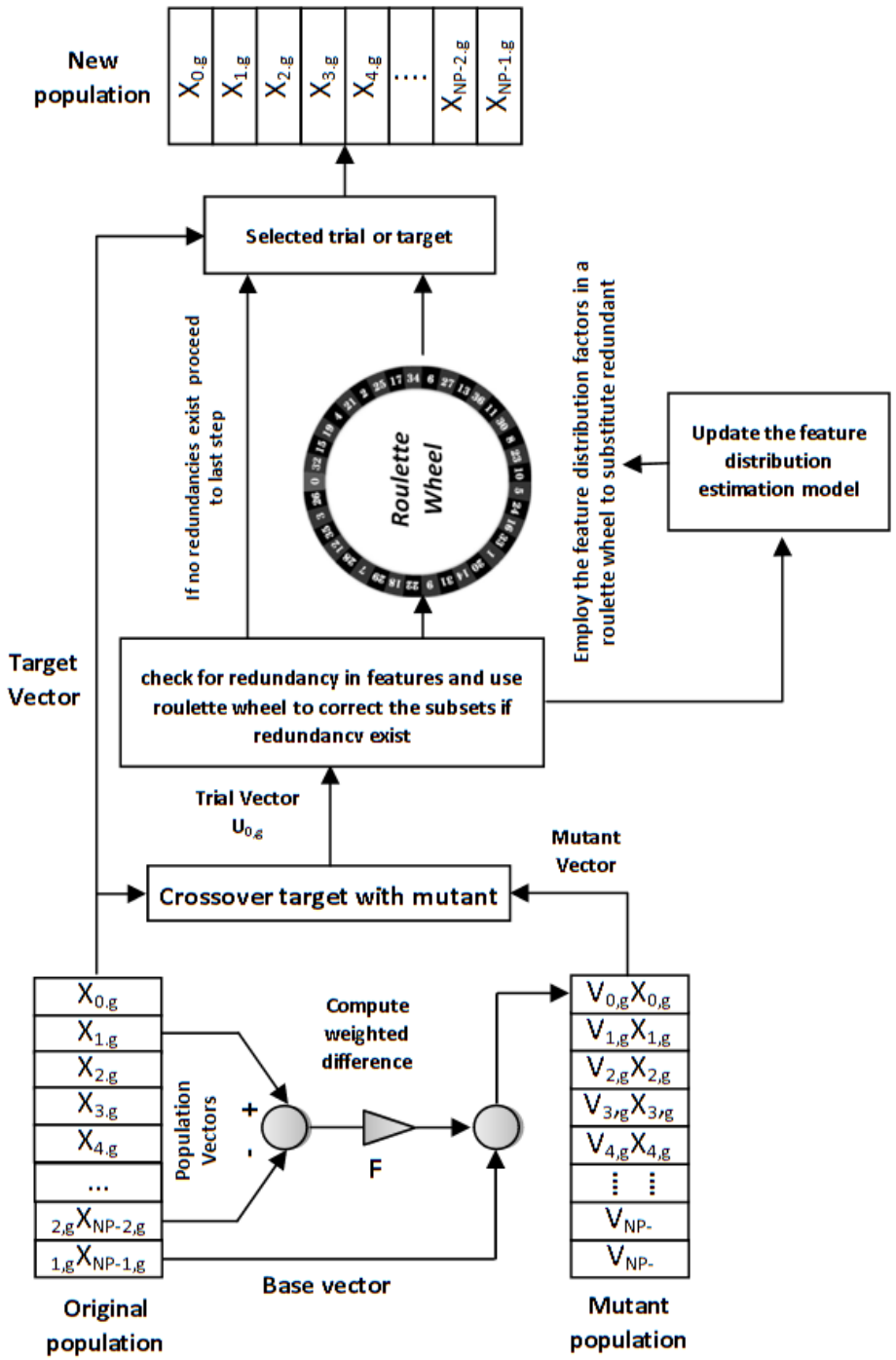

Figure II. 3. Block diagram of the DEFS Algorithm [83, 86].

DEFS algorithm has been employed in microemboli detection field in [18], in which K. Ferroudji, et al. conducted an experimental study on how micro emboli problem can be detected and characterized using discrete wavelet transform and DEFS algorithm, the results indicate that DEFS approach is suitable for this application [18].

II.3-1.2 Fisher Score algorithm

Fisher score is a supervised filter feature selection technique, it is one of the most widely used supervised feature selection techniques due to its general good performance. Given class labels, *y ={y1,...yn},* Fisher Score selects each feature independently by which the within-class distance is minimized and the between-class distance is maximized [64]. The evaluation criterion used in Fisher Score can be formulated as:

$$SC_F(f_i) = \frac{\sum_{j=1}^{c} n_j (\mu_{i,j} - \mu_i)^2}{\sum_{j=1}^{c} n_j \sigma_{i,j}^2} \ , \qquad \text{(II.13)}$$

where

μ_i is the mean of the feature f_i,

n_j is the number of samples in the j^{th} class.

$\mu_{i,j}$, $\sigma^2_{i,j}$ are the mean and the variance of the feature f_i in class j, respectively.

Fisher score seeks features that are efficient for discrimination. In order to select the most significant features, they are sorted according to the decreasing order of their Fisher criterion (refer to Figure II.4). It assigns the highest score to the feature on which the data points of different classes are far from each other while requiring data points of the same class to be close to each other. Consequently, Fisher score algorithm provides a ranked list of all features.

Figure II.4 draws the separability (SC_F) of each component of feature, in blue the features are sorted according to the decreasing order of their Fisher criterion. The original order of the features is presented in red.

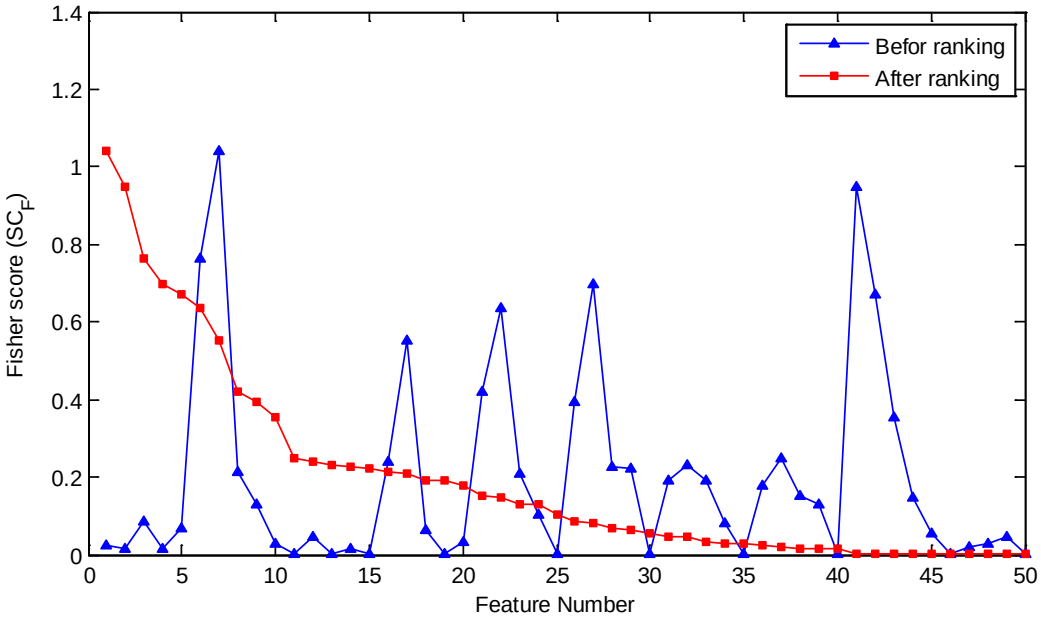

Figure II. 4. Separability (SCF) of each component of feature with concentration of microbubbles (0.025 µl / ml) at low MI (0.2).

II.3-2 Feature generation

II.3-2.1 Principal Component Analysis (PCA)

Principal Component Analysis (PCA) is a statistical technique of dimensionality reduction that is used to approximate a large dataset and decrease its complexity while retaining as much of its information as possible (the information is measured here by the total variance of the data points). Approximation of the data patterns is obtained by creating new, mutually independent, features that are mathematically represented by linear combinations of the original features.

Given a dataset of *n* dimensions, PCA aims to create a linear subspace of dimension *d* lower than *n* such that the data points are positioned mainly on this linear subspace. The linear subspace is defined by *d* orthogonal vectors that form a new coordinate system, called the "principal components".

The new orthogonal dataset which is linearly projected to another dimension contains a series of principal components. These principal components are sorted in the descending order of the eigen vectors based on the respective eigen values. The eigen vector or the principal component which has the highest eigen value is selected as the first principal

component followed by the second principal component and so on till the last column based on the decreasing eigen values. The eigen vectors or the principal components whose respective eigen values are very small are discarded, thereby producing a new matrix *Y*. In such case the initial data set *X* which was of the dimension $r \times c$ is finally transformed and reduced to a matrix Y with dimension $r \times k$, where *k* is less than *c* [87].

The PCA algorithm is performed using the following procedure:

Step 1. Data preparation

In this step, the dataset X_{rxc} (data matrix) is prepared with *r* rows where each row represents a sample with *c* features.

Step 2. Mean subtraction

In this step, the mean of each column in the dataset X_{rxc} is calculated and subtracted from every data of their respective columns. Therefore, the new dataset is zero mean.

$$M_j = \frac{1}{r}\sum_{i=1}^{r} X_{ij} \qquad j = 1,2,3 \dots, c \tag{II. 14}$$

$$X = X - IM \tag{II.15}$$

Here, I_{rx1} is a unity column vector and M_{1xc} is a row vector with all the mean values of each column $[M_j]$.

Step 3. Covariance matrix

Covariance is a practical measure which finds out the variance of the data from the mean with reference to other data in that row. The covariance of a data with itself is equal to the variance of that data. For example, a 3-dimensional data set (x_1,x_2, x_3), the covariance that can be obtained are $cov(x_1, x_2)$, $cov(x_2, x_3)$ and $cov(x_1, x_3)$. Consequently, a covariance matrix *C* is produced with $c \times c$ dimension. This is represented as:

$$C = \begin{bmatrix} cov(x_1, x_1) & cov(x_1, x_2) & cov(x_1, x_3) \\ cov(x_2, x_1) & cov(x_2, x_2) & cov(x_2, x_3) \\ cov(x_3, x_1) & cov(x_3, x_2) & cov(x_3, x_3) \end{bmatrix} \tag{II.16}$$

$$cov(x_1, x_2) = cov(x_2, x_1) \tag{II.17}$$

$$cov(x_1, x_2) = \frac{\sum_{i=1}^{r}\{(x_{1,i} - M_1)(x_{2,i} - M_2)\}}{(r-1)} \quad \text{(II. 18)}$$

Computationally, a much simpler way of doing this calculation is

$$C = X^T X \quad \text{(II.19)}$$

$$X = [X_1, X_2, \dots, X_r]^T \quad \text{(II.20)}$$

$$X_i = (x_{i1}, x_{i2}, \dots x_{iC}) \qquad i = 1,2, \dots, r \quad \text{(II.21)}$$

Step 4. Eigen vectors and eigen values

In view of the fact that the covariance matrix is a square matrix, the calculation of eigen vectors and eigen values are possible. The eigen vectors are sorted based on the descending order of their respective eigen values (*k*). The first column in the eigen vector matrix is the first principal component and is the one with the biggest variance. All eigen vectors are orthogonal to each other. The second column in the eigen vector matrix is called the second principal component and so on.

Step 5. Selection of basis vectors

This step is vital for undergoing dimensionality reduction of the data set as the cut-off factor number or column number eventually selects the basis vectors of the reduced eigen vector matrix. This selection should be carried out in an optimized manner where dimensionality reduction is achieved without the loss of important information. The basis vectors from all the eigen vectors are selected based on a threshold value α which is dependent on the problem statement. This threshold value is compared with the sum of the eigen values (b_k).

$$b_k = \sum_{i=1}^{k} \lambda_i \quad \text{(II. 22)}$$

If b_k is greater than the threshold value α and *k* is the cut-off factor number, then the first *k* eigen vectors are selected as basis vectors.

These basis vectors form a new matrix named B_{cxk} where *k* is less than *c*. A scree test also helps in deciding the k-value or cut-off factor number [88].

Step 6. Final projected data set

The initial X_{rxc} data set is finally projected on to a new structure with a new set of data matrix Y_{rxk}.

$$Y_{rxk} = X_{rxc} \times B_{cxk} \quad \text{(II.23)}$$

This produces a new data set with reduced dimensionality.

Principal component analysis is employed in [89] as a dimensionality reduction technique together with SVM as a classifier, SERBES, et al. used Doppler ultrasound signals recorded from both forward and reverse flow of blood for the classification of embolic signals.

Moreover, Da Xu, et al. proposed an emboli detection system for the classification of three kinds of clinical signals: the normal blood flow signal, the signal containing emboli (embolic signal), and the signal containing disturbance noises. They employed PCA, fuzzy sets and Doppler ultrasound signals in the classification system [90].

II.4 Performance Metrics

In order to evaluate the performance of our model we use information collected from the confusion matrix (CM). CM illustrates the number of correct and incorrect predictions made by the classifier compared with the true labels in the test data. Furthermore, the performance of the proposed model is evaluated by comparing the predicted values with the actual class values using different statistical indexes such as Recall (Sensitivity), Specificity, Precision, Kappa, F-measure, overall accuracy, and AUC (Area Under Curve).

Table II. 1. Confusion matrix for binary classification model.

		Predicted	
		Gaseous emboli	Solid emboli
Actual class	Gaseous emboli	**TP**	**FP**
	Solid emboli	**FN**	**TN**

where

- True Positive (TP): The classifier predicts a label as gaseous emboli and the actual class is gaseous emboli.
- True Negative (TN): The classifier predicts a label as solid emboli and the actual class is solid emboli.
- False Positive (FP): The classifier predicts a label as solid emboli and the actual class is gaseous emboli.
- False Negative (FN): The classifier predicts a label as gaseous emboli and the actual class is solid emboli.

II.4-1 Accuracy

Accuracy (ACC) is a widely used metric for measuring the performance of a classifier. ACC is the percentage of the correctly classified positive and negative labels. However, ACC does not discount the correct match between the reference and the predicted data obtained by pure chance. It is expressed as:

$$Accuracy = \frac{TP+TN}{TP+TN+FP+FN} \quad \text{(II.24)}$$

II.4-2 Sensitivity or Recall

Recall (r) is defined as the number of actual positives divided by the total number of samples that actually belong to the positive class (the proportion of actual positives which are predicted positive) it can be expressed as:

$$r = \frac{TP}{TP+FN} \quad \text{(II.25)}$$

II.4-3 Specificity

Specificity (Spe) is the proportion of actual negative which are predicted negative:

$$Spe = \frac{TN}{TN+FP} \quad \text{(II.26)}$$

II.4-4 Precision

In the actual context, the precision (*P*) is defined as the number of true positives divided by the total number of elements categorized as belonging to the positive class:

$$P = \frac{TP}{TP+FP} \quad \text{(II.27)}$$

II.4-5 F-measure

The F-measure (*F*) combines the two ratios known as recall and precision [91]. F-measure represents the harmonic mean of precision (*P*) and recall (*r*); it is expressed as follows:

$$F = (1+\beta^2) \times \frac{p \times r}{(\beta^2 \times p)+r} \quad , \quad \text{(II.28)}$$

where

P: is the Precision

r: is the recall

The precision, recall, and F-measure vary from 0 to 1. The F-measure reaches its best value at 1 whenever *P* and *r* are simultaneously equal to 1. The parameter β allows one to weight either precision or recall more heavily, and they are balanced when β = 1. In most experiments, there is no particular reason to favor precision or recall, therefore In this section, the value of β is set to 1.

II.4-6 Kappa coefficient

Another measure which can be extracted from a confusion matrix is the Kappa coefficient. It is a statistical measure of inter-raters agreement [91, 92]. This measure is more robust than the accuracy measure since it subtracts the agreement occurring by chance. This coefficient is expressed as:

$$Kappa = \frac{P(a)-P(e)}{1-P(e)} \, , \quad \text{(II.29)}$$

where

P(a): is the probability of relative observed agreement among raters,

P(e) : is the probability of chance agreement.

The range of the kappa values is [-1,1], although it usually falls between 0 and 1. The value 1 represents perfect agreement, indicating that the raters agree in their classification in every case. The value 0 indicates agreement no better than chance, as if the rater has simply "guessed" every rating. A negative Kappa would indicate agreement worse than chance.

II.4-7 ROC curve

Furthermore, we investigated other statistical measure which better estimates the accuracy of a given trial test by analyzing sensitivity and specificity simultaneously, this approach is the area under curve (AUC) associated to the Receiver Operating Characteristic curve (or ROC curve) [93]. AUC allows to quantify the ROC curve performance using a single value. It is well known that the higher the AUC value, the more efficient the classifier. Efficient classifier's areas should have an AUC value larger than 0.5.

II.4-8 Determination coefficient

The determination coefficient (R^2) indicates the strength of the fitting model that illustrates the relationship between the measured and predicted values (R^2 indicates of how well the model fits the data) [94] and is computed from the sums-of-squares terms:

$$\sum_{i=1}^{n}(y_i - \bar{y})^2 = \sum_{i=1}^{n}(f_i - \bar{y})^2 + \sum_{i=1}^{n}(f_i - y_i)^2 \qquad (II.30)$$

$$SS_{Tot} = SS_{Reg} + SS_{Res} \qquad (II.31)$$

$$R^2 = \frac{SS_{Reg}}{SS_{Tot}} = 1 - \frac{SS_{Res}}{SS_{Tot}}, \qquad (II.32)$$

where

y_i : The data set values.

$\bar{y}$: Average value of the data set values.

$$\bar{y} = \frac{1}{n}\sum_{i=1}^{\infty} y_i, \qquad (II.33)$$

where

f_i: Predicted model values.

n : length of the data set

SS_{Tot} : The total sum of squares (proportional to the variance of the data).

SS_{Reg} : The regression sum of squares, also called the explained sum of squares.

SS_{Res} : The sum of squares of residuals, also called the residual sum of squares.

If the regression is perfect, all residuals are zero, SS_{Res} is zero, and $R^2 = 1$ if there is no linear relationship between the predicted and the actual values, then R^2 is equal to 0.

II.5 Conclusion

This chapter presents a literature review of available artificial intelligence techniques that have been employed in this thesis. In order to evaluate the performance of the proposed system, we evaluate three classification algorithms with main focus on: Multilayer Perceptron Neural Networks, Radial Basis Function Neural Networks, and Support Vector Machines. Furthermore, we compare the performances of three dimensionality reduction techniques; Differential Evolution algorithm, Fisher Score method, and Principal Component Analysis. The motivation of dimensionality reduction approach is that the more powerful among the existing machine learning algorithms tend to get confused when supplied with a large number of features. In order select the optimal parameters of the proposed models and to avoid the overfitting of the classifiers, we use Cross-validation technique with several evaluation metrics.

Chapter III : Experimental set-up and data acquisition

III.1 Introduction

As part of the cooperation project INSERM (France / Algeria DPGRF) 2007-2008 and the TASSILI project (14 MDU 909), the acquisition of echo signals is made in the INSERM U930 laboratory at the University of François Rabelais Tours, France under the direction of Professor A. Bouakaz. In this chapter we present the experimental set-up as well as the acquisition of the embolic signal used in this thesis.

III.2 Experimental set-up

In order to verify the usefulness of RF ultrasound signal processing for microemboli classification, an in vitro set-up is developed. It consists of a Doppler flow phantom containing 3 tubes of 0.2, 0.4 and 0.8 mm in diameter. The tube of 0.8 mm is chosen since its size approximates the size of a human vessel (Figure III.1). In order to mimic the ultrasonic behavior of gaseous emboli, contrast agents consisting of microbubbles are used in our experimental setup. Indeed, several studies have revealed that the acoustic behavior of gaseous emboli and microbubbles are similar, mainly the nonlinear behavior [16, 18, 24]. Hence, a continuous flow carries Sonovue microbubbles [51, 95] (contrast microbubbles) through the insonified vessel is exploited in the experimental set-up. We used Sonovue microbubbles since it is the only commercially available contrast agent in Europe. The concentration of microbubbles and the flow are controlled by the operator. In clinical situations, the scattering amplitude of emboli approaches that of blood, hence we fixed the concentration of Sonovue microbubbles such as its scattering amplitude at the fundamental frequency is comparable to the scattering of the surrounding tissue at the same frequency.

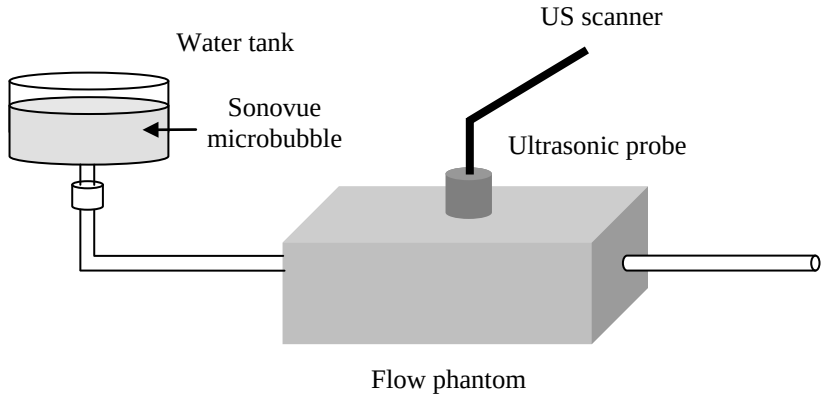

Figure III. 1. Experimental set-up

However, solid emboli present acoustic properties comparable to those of biological tissue, in their scattered signal no harmonic components can be seen, therefore the scattering of solid emboli is purely linear. Thus, the tissue mimicking material surrounding the vessel is chosen to mimic the behavior of solid emboli. Moreover, the applied acoustic pressures are not sufficiently high to induce nonlinear propagation effects and does not generate any harmonic components during ultrasound propagation.

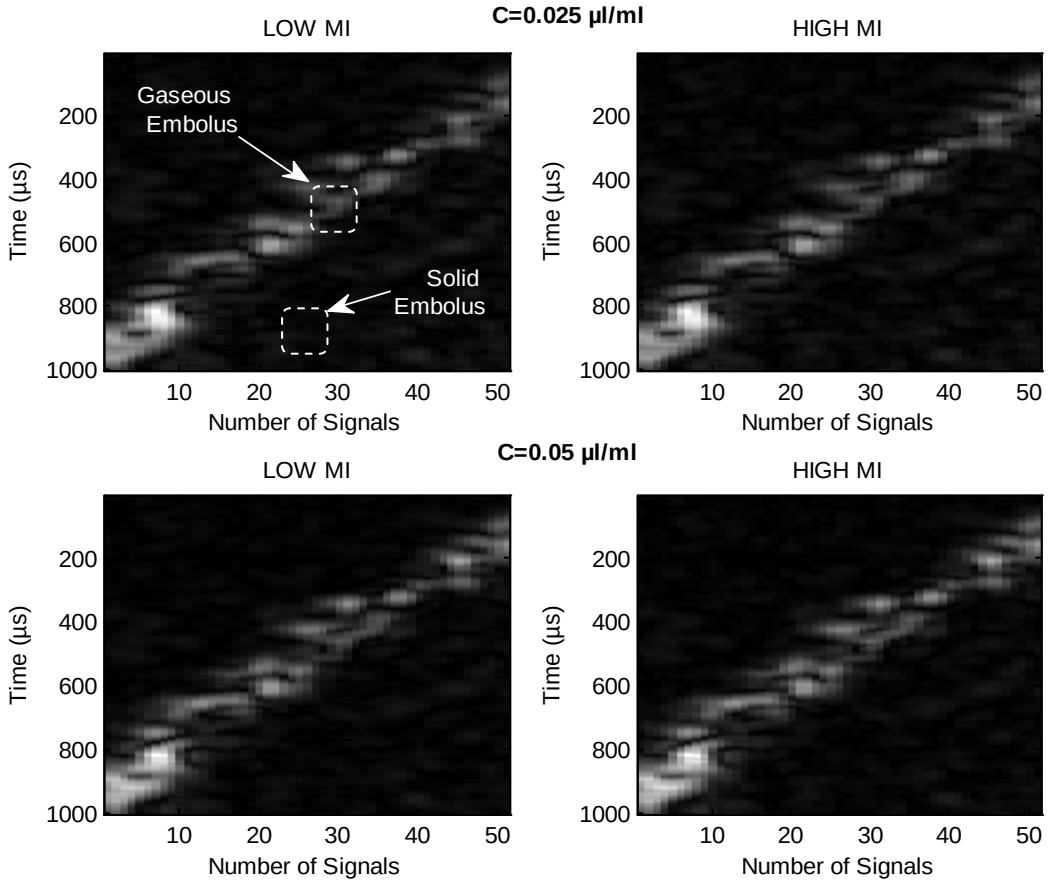

Figure III. 2. Grayscale images acquired: A. MI= 0.2, B. MI= 0.6 for two microbubbles concentrations

The ultrasound waves are generated by a VF13-5 probe connected to a Siemens Antares scanner (Anthares, Siemens, MV, CA). The acquisitions are carried out at 1.82 MHz transmit frequency in Tissue Harmonic Imaging (THI) mode using 14 fps frame rate, and 20 MHz as the sampling rate of the signals. The acoustic focus is set at 2 cm which is the depth at which the flowing contrast microbubbles are situated. Ultrasound waves are transmitted at two different intensities corresponding to mechanical indices (MI) of 0.2 (low MI) and 0.6 (high MI).

The User Research Interface is used to grab the unfiltered RF signals to a personal computer for further analysis. The microbubbles are administered into a 200 ml volume of Isoton. Two concentrations of contrast agent/Isoton are used: 0.025µl/ml and 0.05µl/ml [18, 24]. The regions of interests where RF signals corresponding to gaseous embolus and solid embolus are shown in Figure III.2.

From Figure III.2, it is clear that the white spots represent microbubbles, i.e the gas embolus and the remaining is the solid embolus.

Examples of radio frequency (RF) signals extracted from the ultrasound images are shown in Figures III.3 and III.4.

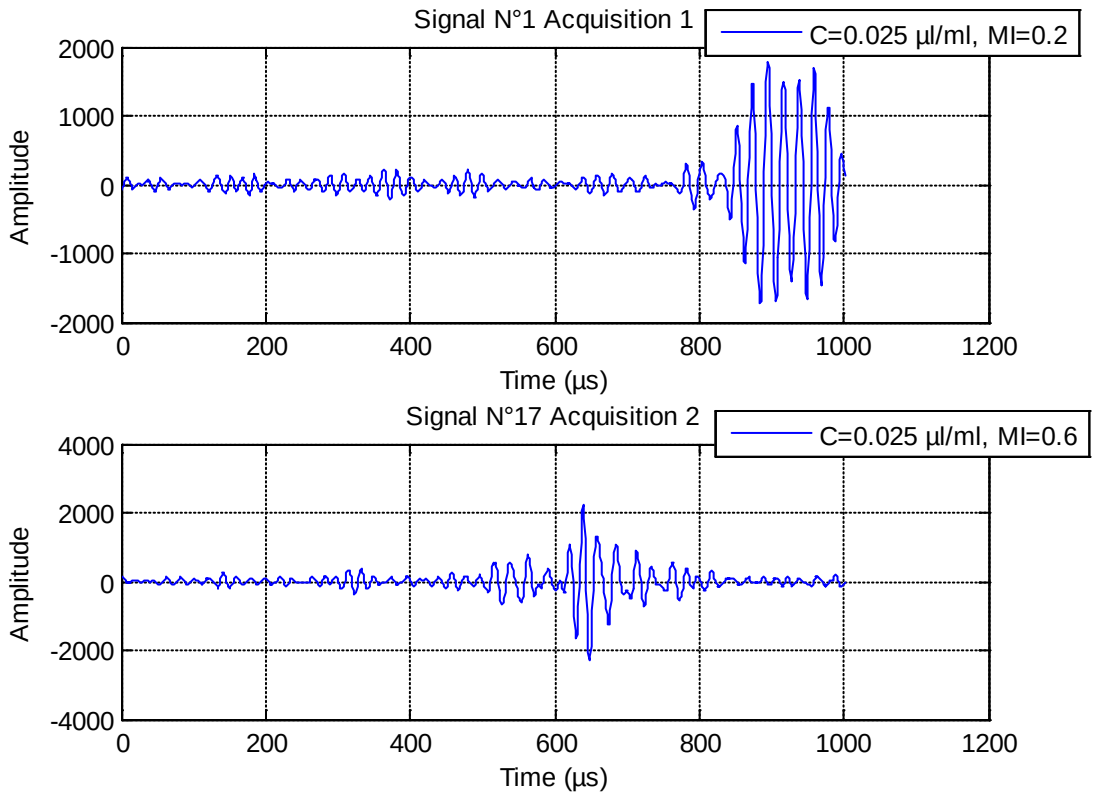

Figure III. 3. RF Signals Acquisition 1 and 2.

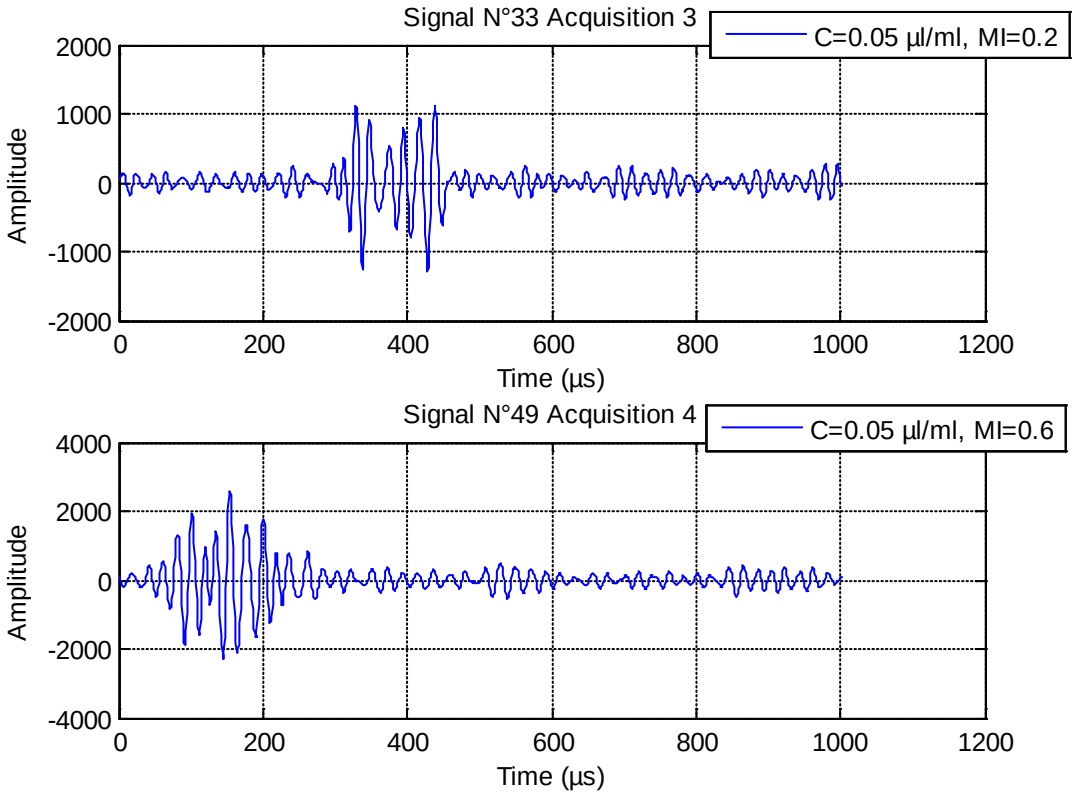

Figure III. 4. RF Signals Acquisition 3 and 4.

Each echo of the four acquisitions consists of 51 radio frequency signals. In the next section we extract the gas and solid intervals from the RF signals constituting the ultrasound image.

III.2-1 Gas and solid intervals

III.2-1.1 Gas intervals

In the following, we describe the steps that we have performed to create the gas interval:

1- Take a time segment of signal whose width is equal to 223 µs (a time window), and move it along the global interval and calculate the energy of the signal in each iteration.

$$E_x = \sum_{i=1}^{51} \left| \left(x(N:M,i) \right) \right|^2, \qquad \text{(III. 1)}$$

where:

E_x : energy of the RF signal.

x : Radio frequency signal.

N : The minimum value of the interval (Initially equal to 1).

M : The maximum value of the interval (Initially equal to 223).

2- We choose the interval which gives maximum energy.

3- What remains is the solid interval

Once the window passes over the entire signal, we obtain 51 gas signals and 51 solid signals of size equal to 223 µs and 778 µs respectively.

The results are shown in the Figures III.5, III.6, III.7, and III.8.

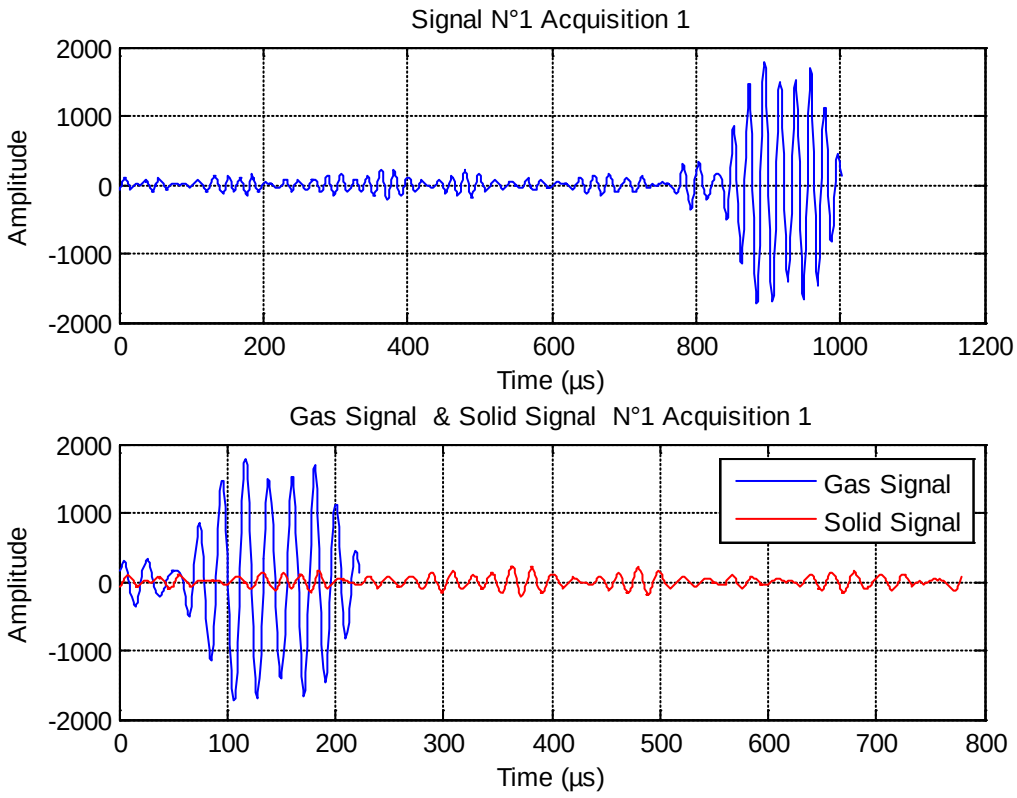

Figure III. 5. Gas and solid signals Acquisition 1.

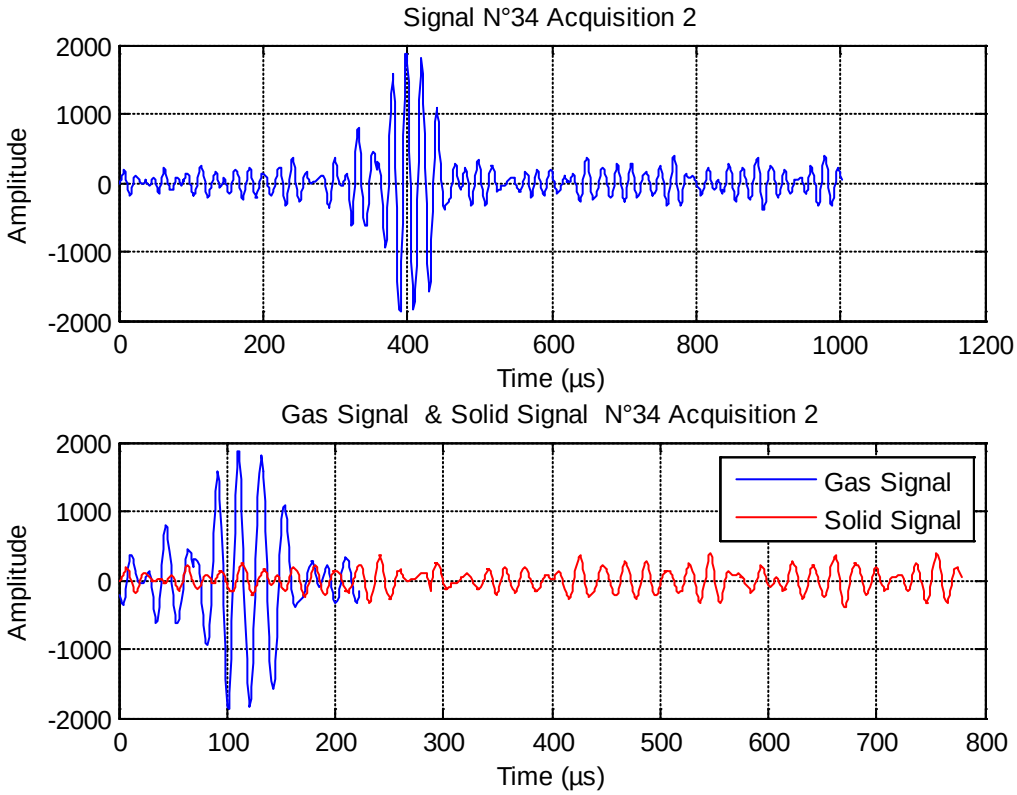

Figure III. 6. Gas and solid signals Acquisition 2.

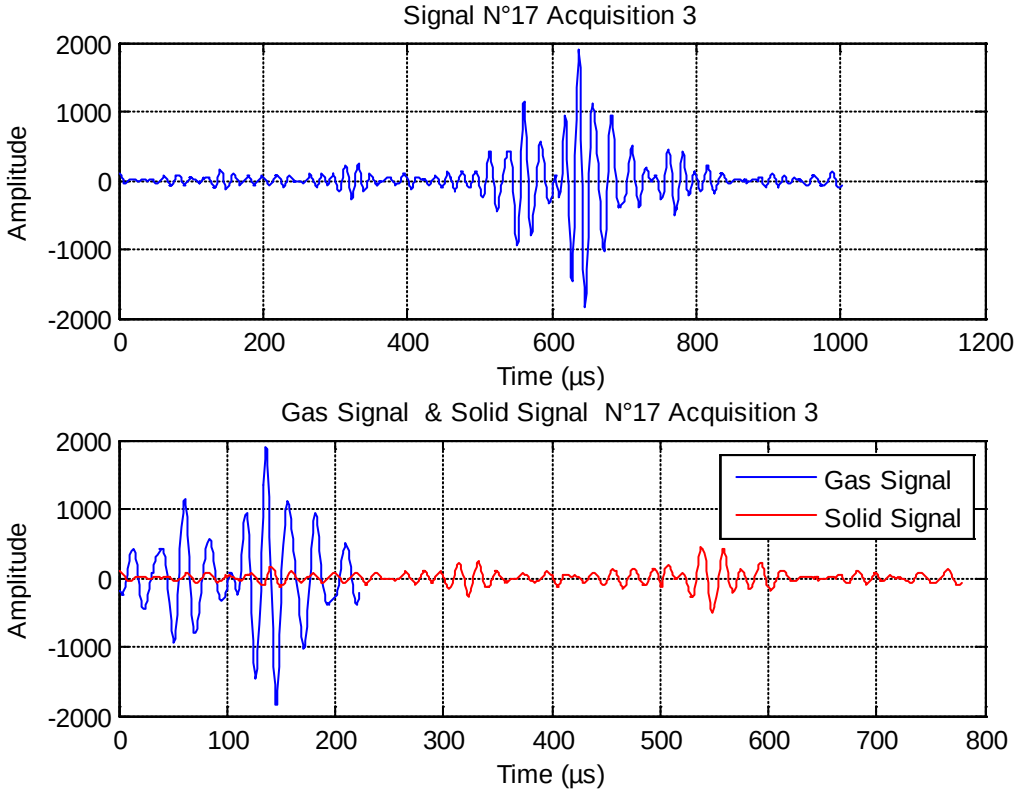

Figure III. 7. Gas and solid signals Acquisition 3.

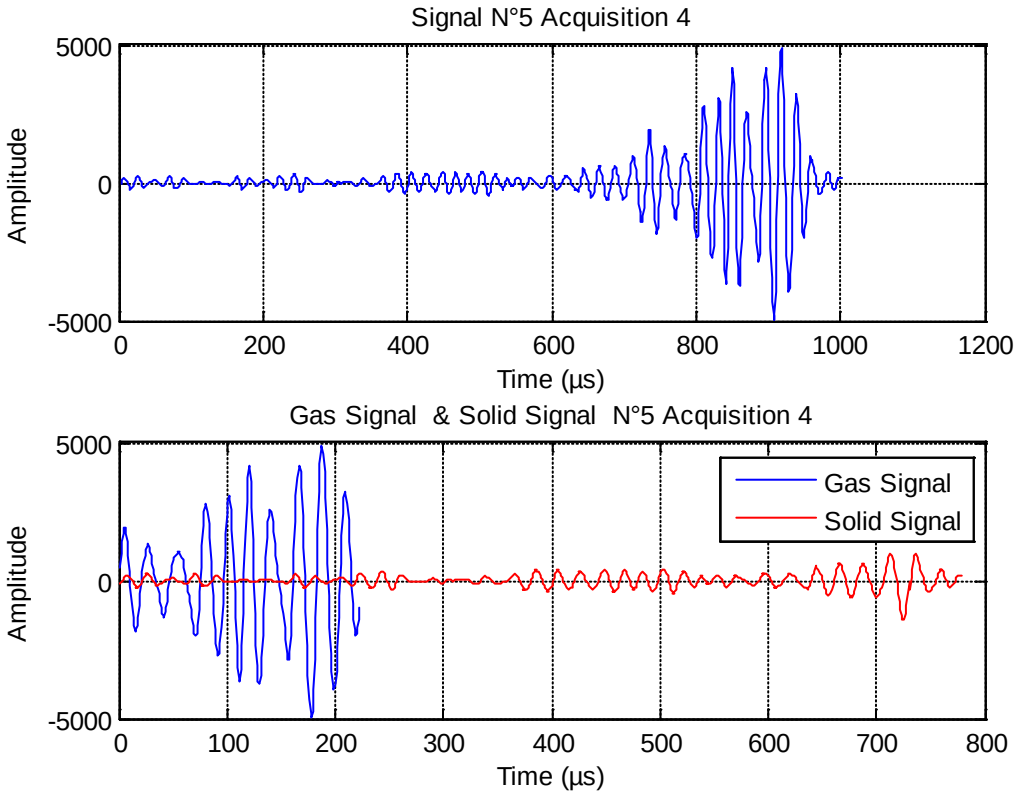

Figure III. 8. Gas and solid signals Acquisition 4.

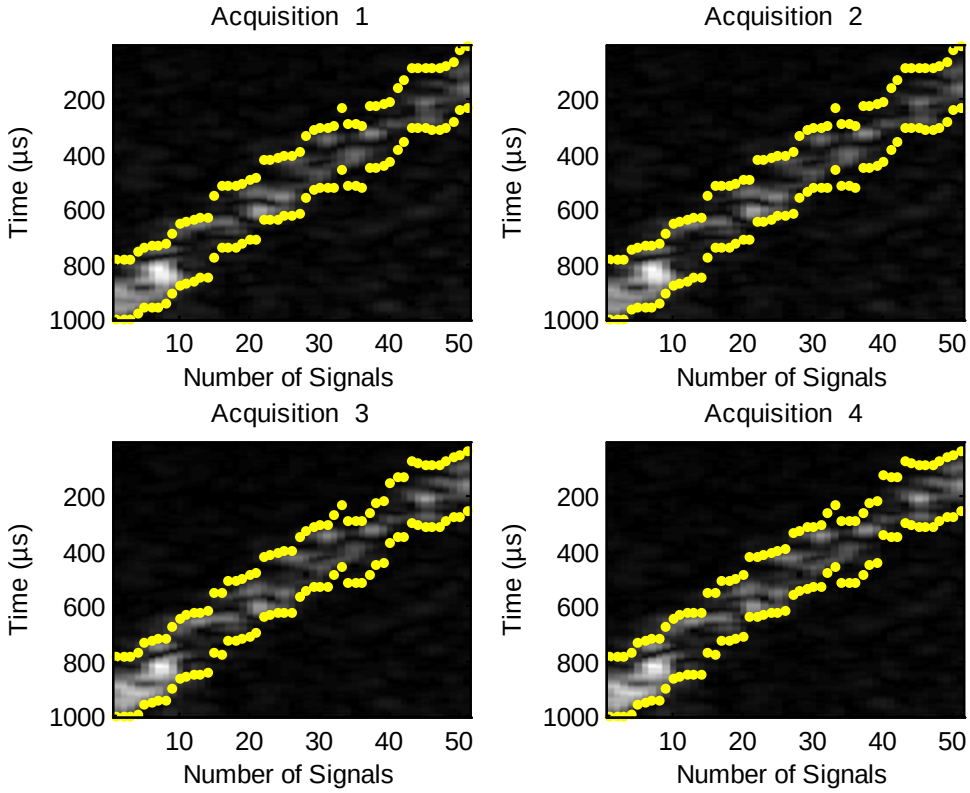

Figure III. 9. Gas intervals for the four Acquisitions.

The intervals of RF gas signals for the two concentrations of microbubbles 0.025µl/ml and 0.05µl/ml at two mechanical indices (MI) of 0.2 (low MI) and 0.6 (high MI) are shown in Figure III.9.

III.2-1.2 Solid intervals

Once the gas intervals are calculated, it remains the calculation of the solid intervals which must has the same size as gas intervals. In order to do so, we chose the solid intervals which has the same depth as that of the gas intervals (refer to Figure III.10).

Figure III.11 shows the gas and solid intervals that will be used to extract gas signals (stand for gas emboli) and solid signals (stand for solid emboli).

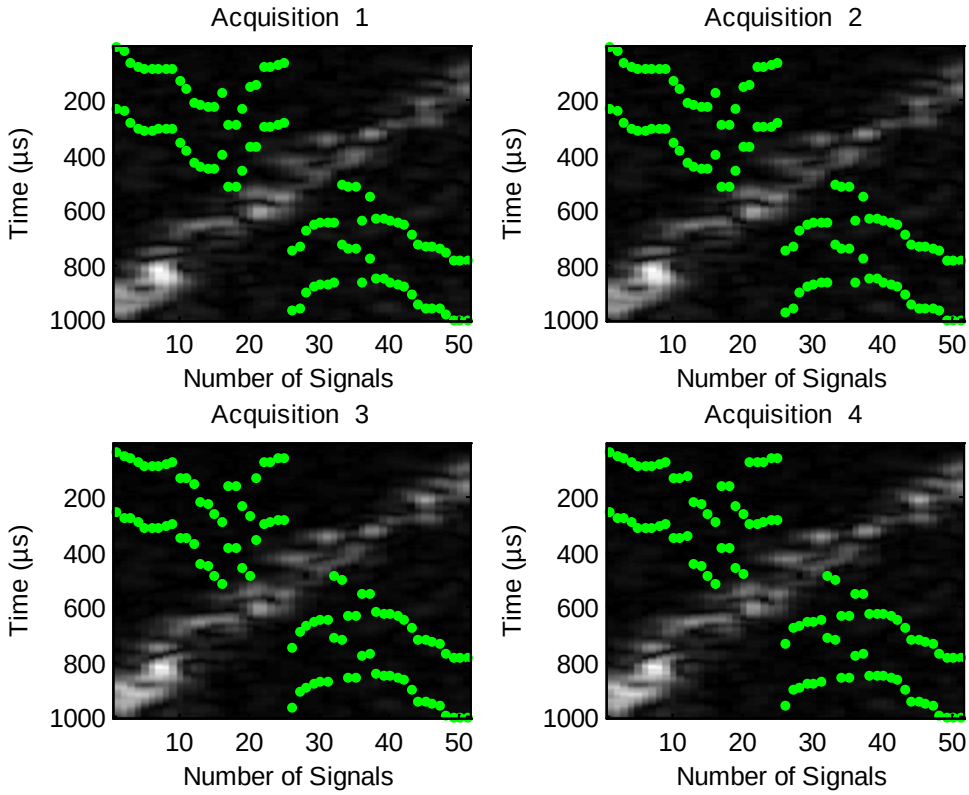

Figure III. 10. Solid intervals for the four Acquisitions.

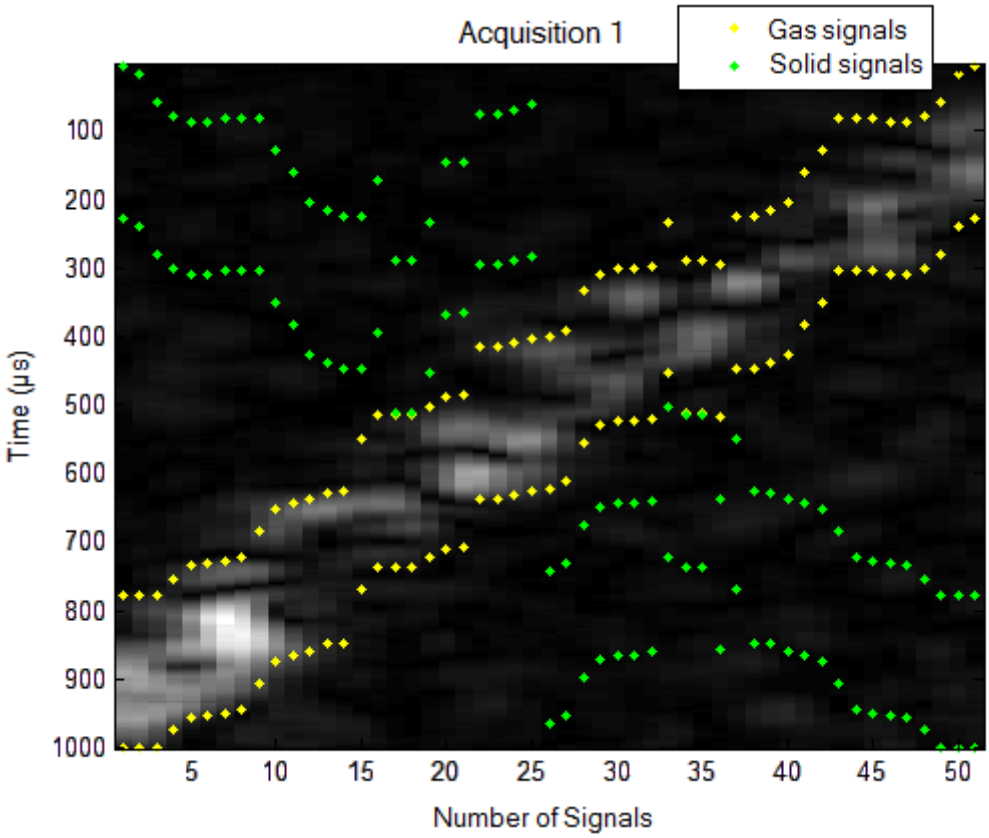

Figure III. 11. Gas and solid intervals for the Acquisition 1.

In previous work of N. BENOUDJIT et al. on the same ultrasound images the classification rates were 100% this is due to the fact that the amplitudes of the gas signals are clearly superior to those of the solid signals [96]. In our work, and in order to get closer to the reality that corresponds to the acquisition of ultrasounds on the capillaries whose diameter is too small which gives a very low distinction between the gas and the tissue. We have opted for the normalization of gas signals (gaseous emboli) and solid signals (solid emboli)

III.2-1.3 Normalization

Normalization is a pre-processing performed on all time segments of RF signals. It is employed to restrict the values of all features within predetermined ranges. It consists in normalizing the amplitude of the signal to the unit value [97].

The normalization of the gas and solid signals is performed according to the following two equations:

$$x_{gaz\_Nor} = \frac{x_{gaz}}{max|x_{gaz}|} \qquad \text{(III. 2)}$$

$$x_{solid\_Nor} = \frac{x_{solid}}{max|x_{solid}|}, \quad \text{(III. 3)}$$

where:

x_{gaz} , x_{gaz_Nor} : Are the gas signals before and after normalization respectively.

x_{solid} , x_{solid_Nor} : Are the solid signals before and after normalization respectively.

The following figure (Figure III.12) shows the effect of normalization on the four ultrasound images. It should be noted that the distinction between contrast (gaseous emboli) and tissue (solid emboli) is very difficult.

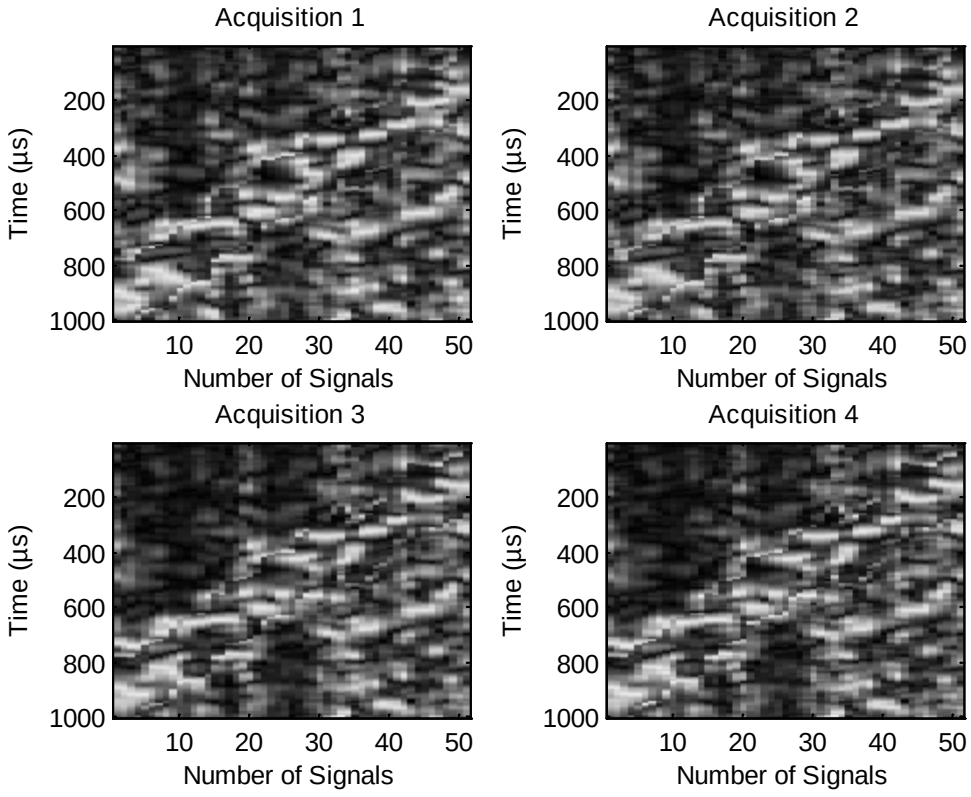

Figure III. 12. Grayscale images acquired after normalization: A) MI= 0.2, B) MI= 0.6 for two microbubbles concentrations.

Once the gas and solid intervals are selected and the normalization of the signals is done, we construct our dataset which contains 51 gas signals and 51 solid signals for each acquisition.

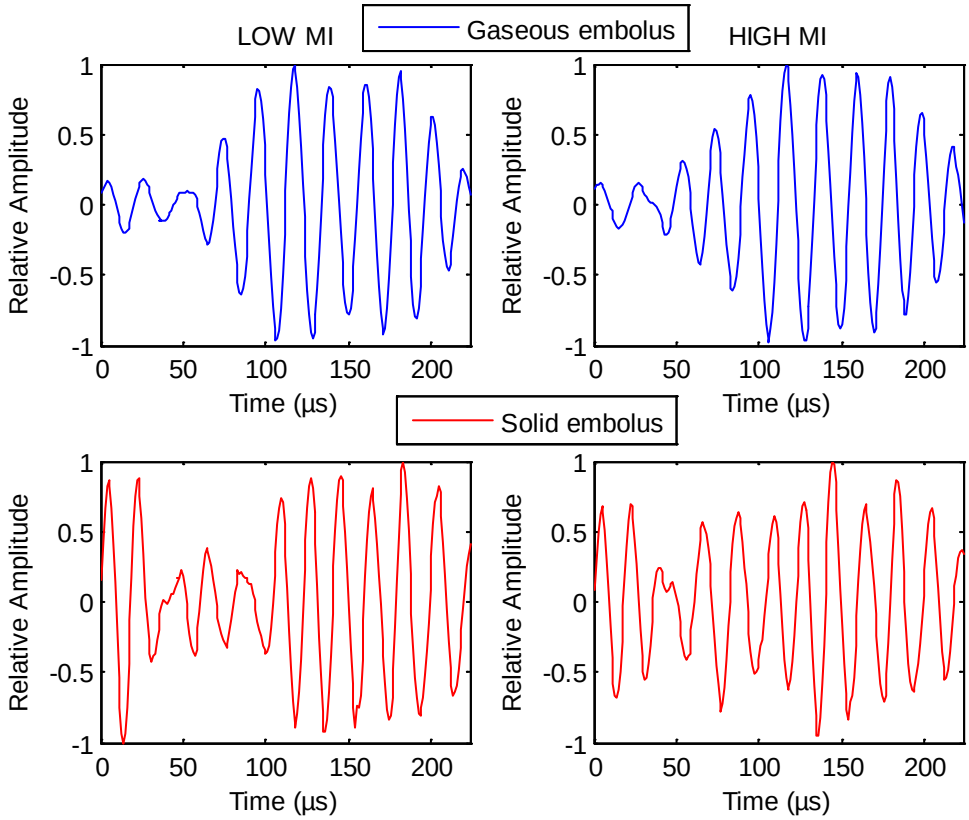

Figure III. 13. Examples of normalized RF signals A) MI= 0.2, B) MI= 0.6.

Figure III.13 illustrates two types of normalized RF signals extracted from the obtained grayscale images. Panel A shows RF signal backscattered by gaseous and solid embolus at low MI (0.2). Panel B illustrates the RF signal of each type of embolus at higher MI (0.6).

III.3 Conclusion

In this chapter, an in vitro set-up is developed in the INSERM U930 laboratory at the University of François Rabelais Tours, France under the direction of Professor A. Bouakaz. As a result, we obtain four datasets, each dataset consists of 102 samples (51 solid emboli and 51 gaseous emboli). In next sections several features are extracted from these signals in order describe the acquired datasets by a number of discriminative features good for classification.

Chapter IV : Particle Characterization Using FFT Based Approach and Artificial Neural Networks

IV.1 Introduction

In this chapter, we propose a new approach to detect and classify microemboli using artificial neural networks and the backscatter RF (Radio-Frequency) signals instead of Doppler signals [24]. We evaluate the predictive power of a set of three feature extraction methods and two different classifiers. The amplitudes and bandwidths of the fundamental (f_0) and the 2nd harmonic components ($2f_0$) are selected as input parameters to the Multilayer Perceptron (MLP) and Radial-Basis Function Network (RBFN) models. Moreover the frequency bandwidths of the fundamental and the 2nd harmonic echoes are approximated by Gaussian functions and the coefficients are used as a third input parameter to the neural network models.

IV.2 Detection algorithm

Figure IV.1 shows the general block diagram of the FFT based neural network classification model employed in this chapter. The input backscatter RF signals are first detected and collected (signal acquisition). In the feature extraction stage and for each gas or solid signal, a vector containing the values of the parameters (amplitude, bandwidth, or the Gaussian coefficients) is constructed. This vector is used as an input to the MLP or RBFN model which provides in its output a value of 1 or 0 for gaseous or solid emboli respectively.

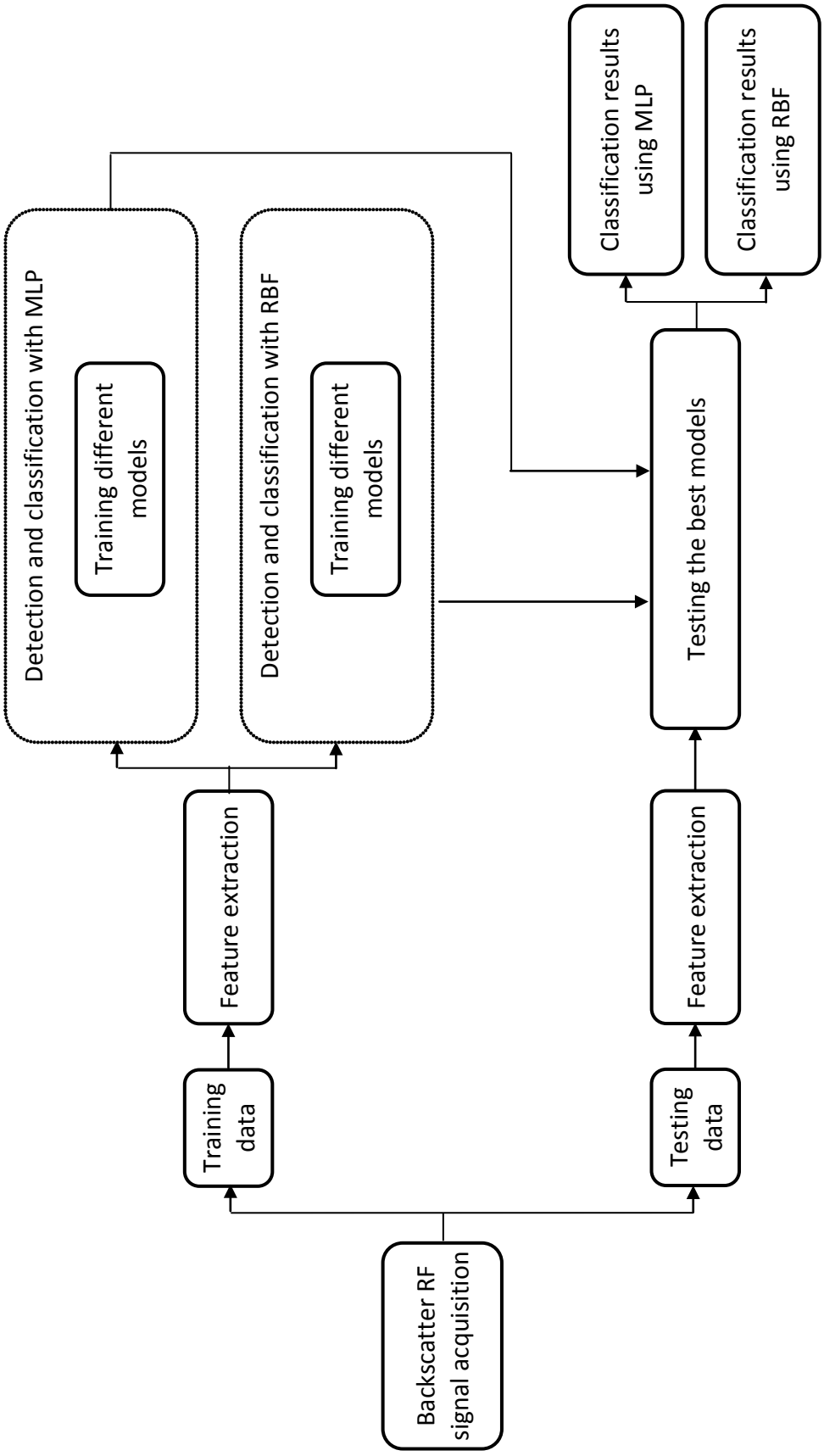

Figure IV.1. Block diagram of the FFT-based detection system.

IV.2-1 Feature extraction

In pattern recognition research, we always aim to reach the best classification rate according to the characteristics required. Feature extraction greatly affects the performance and design of the classification model, and it is one of the core issue of pattern recognition research.

Feature extraction aims to describe the acquired signals by a number of discriminative features good for classification

The following parameters are selected as input to the models:

1- The bandwidths of the scattered RF signals at the fundamental and at the second harmonic frequencies.

2- For every RF signal scattered from the microbubbles (gas emboli) or surrounding tissue (solid emboli), its FFT is calculated. The amplitudes at the fundamental frequency (f_0) and at the second harmonic frequency ($2f_0$) are selected. These values are used as an input parameter.

3- The frequency spectra of the fundamental and the second harmonic are approximated by a Gaussian shape function using the following equation:

$$g(\mathrm{x}) = a_1 \, exp\left(-\left(\frac{(\mathrm{x} - b_1)}{c_1} \right)^2 \right) \qquad \text{(IV.1)}$$

where :

a_1, c_1, and b_1 are the amplitude, width, and center of the Gaussian respectively.

The Gaussian coefficients a_1, b_1 and c_1 are used as a third input parameter.

IV.2-1.1 Amplitudes of gas and solid signals at f_0 and $2f_0$

In order to extract the amplitudes at the frequencies f_0 and $2f_0$, we filter the normalized gas and solid signals by a Butterworth filter.

The normalized RF signals are band-pass filtered by Butterworth filter, then the amplitudes of the signals f_0 and $2f_0$ are estimated from the filtered RF signals at the frequency bands: [1.5-2.5 MHz] and [3-4.5 MHz], the transmit frequency is 1.82 MHz.

This type of filter is designed to have as flat a frequency response as possible in the passing band. The module square of the frequency response of a low pass Butterworth filter is given by [98]:

$$|H(jw)|^2 = \frac{1}{1 + \left(\frac{w}{w_c}\right)^{2n}} \qquad \text{(IV. 2)}$$

where :

H(jw) : *is the* frequency response of the filter.

ω : is the angular frequency and is equal to $2\pi f$.

ω_c : is the cutoff frequency.

n : represents the filter order.

The implemented filter for the acquired signals is a band-pass third-order Butterworth filter. This choice is because the Butterworth approximation has a monotonic function in the pass-band and suppression-band. The Butterworth filter that we have used is characterized by:

f_{h1} = 2.5 MHz: High cutoff frequency.

f_{b1} = 1.5 MHz: Low cut-off frequency

} filtering around the fundamental frequency f_0=1.82 MHz

and,

f_{h2} = 4.5 MHz: High cutoff frequency.

f_{b2} = 3 MHz: Low cut-off frequency

} filtering around the second harmonic $2f_0$ $2f_0$=3.64 MHz

After the application of the Butterworth filter on the four acquisitions, the obtained gas and solid signals before and after filtering at the frequencies f_0 and $2f_0$ are illustrated in the Figures IV.2 to IV.9:

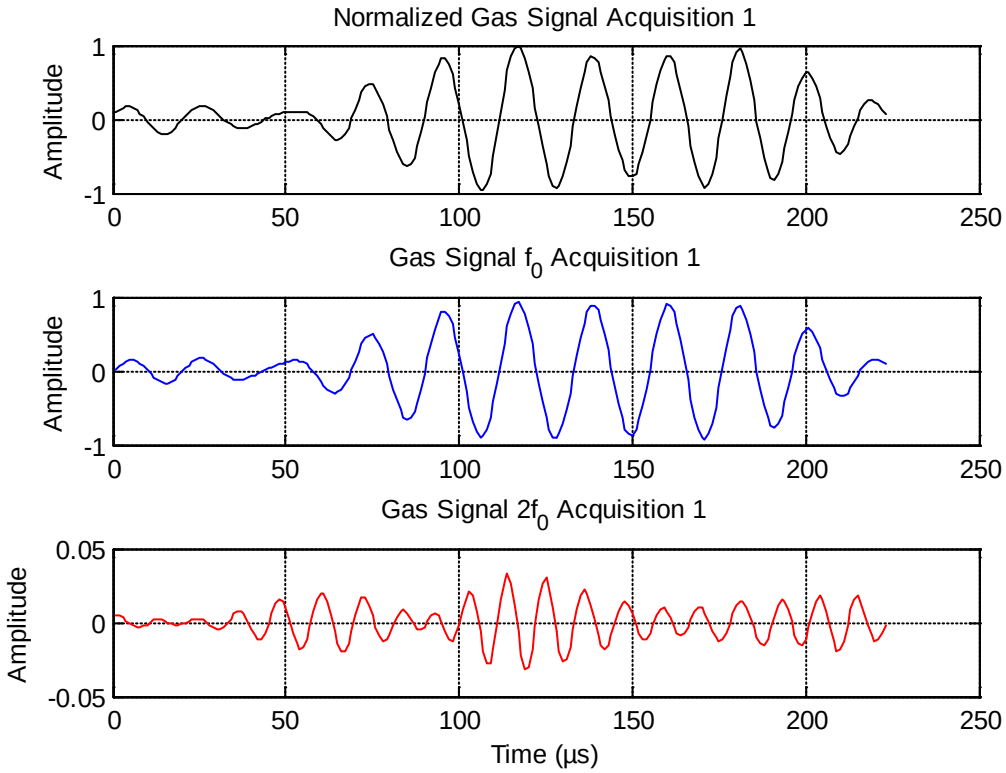

Figure IV.2. Gas signals filtered at f_0 and $2f_0$ for acquisition 1.

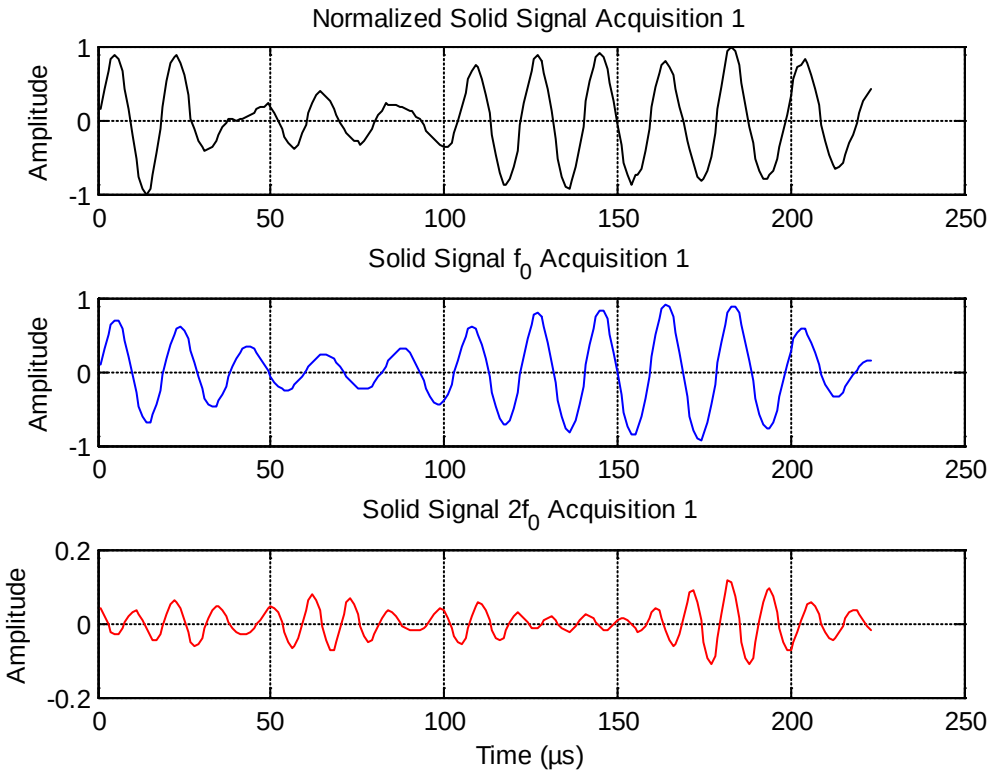

Figure IV.3. Solid signals filtered at f_0 and $2f_0$ for acquisition 1.

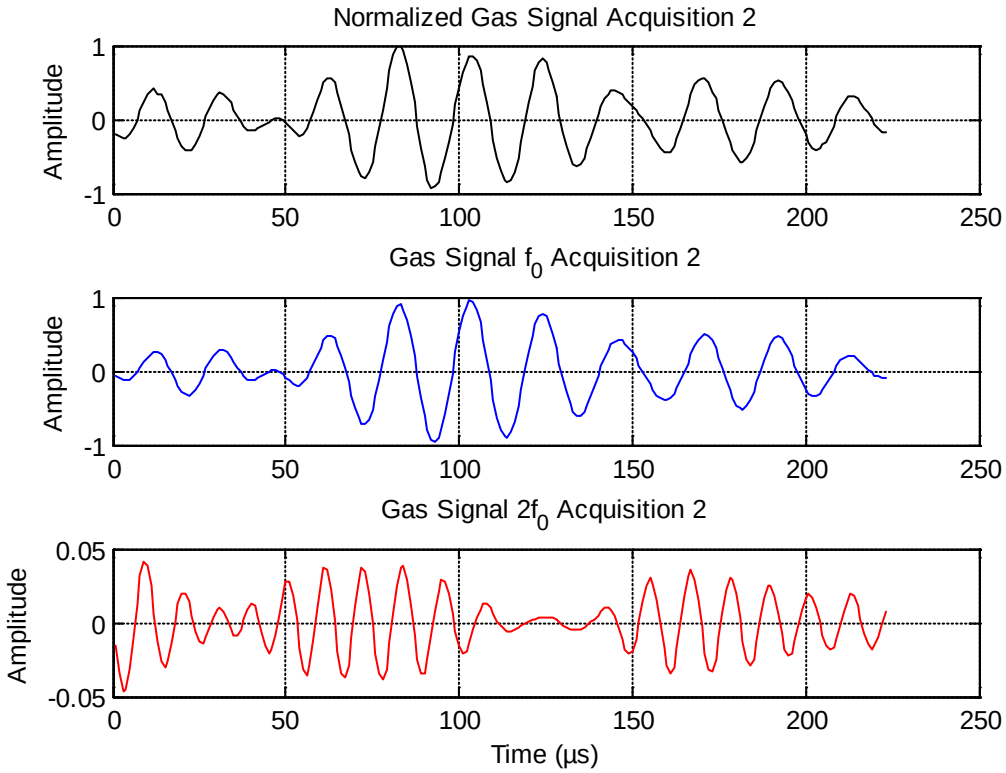

Figure IV.4. Gas signals filtered at f_0 and $2f_0$ for acquisition 2.

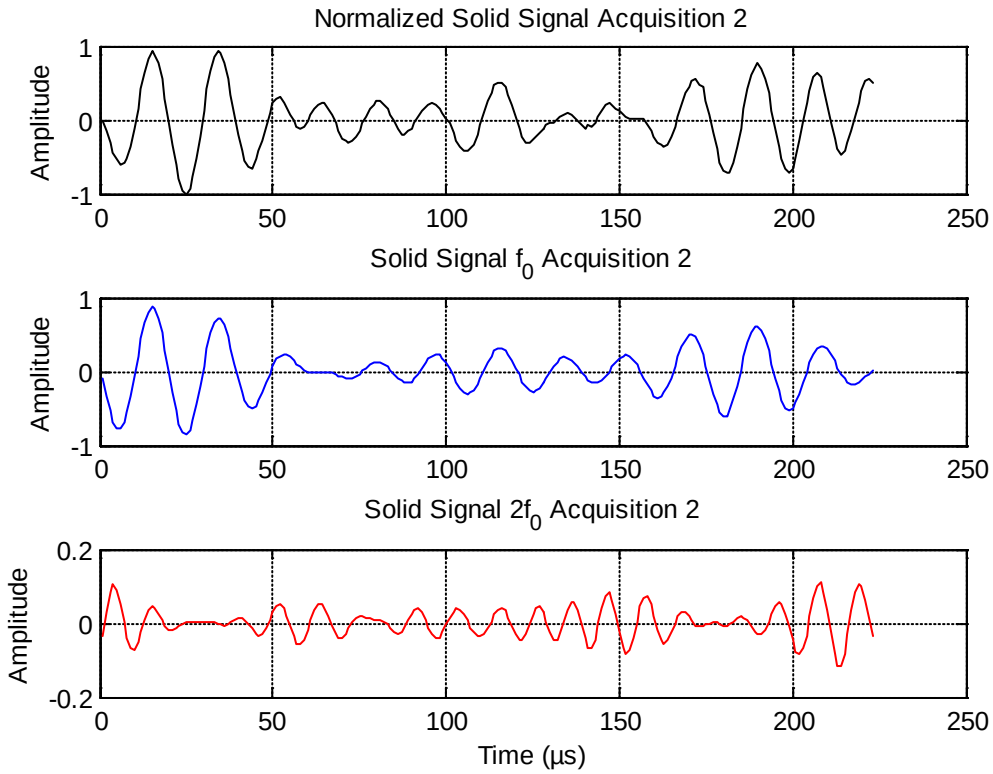

Figure IV.5. Solid signals filtered at f_0 and $2f_0$ for acquisition 2.

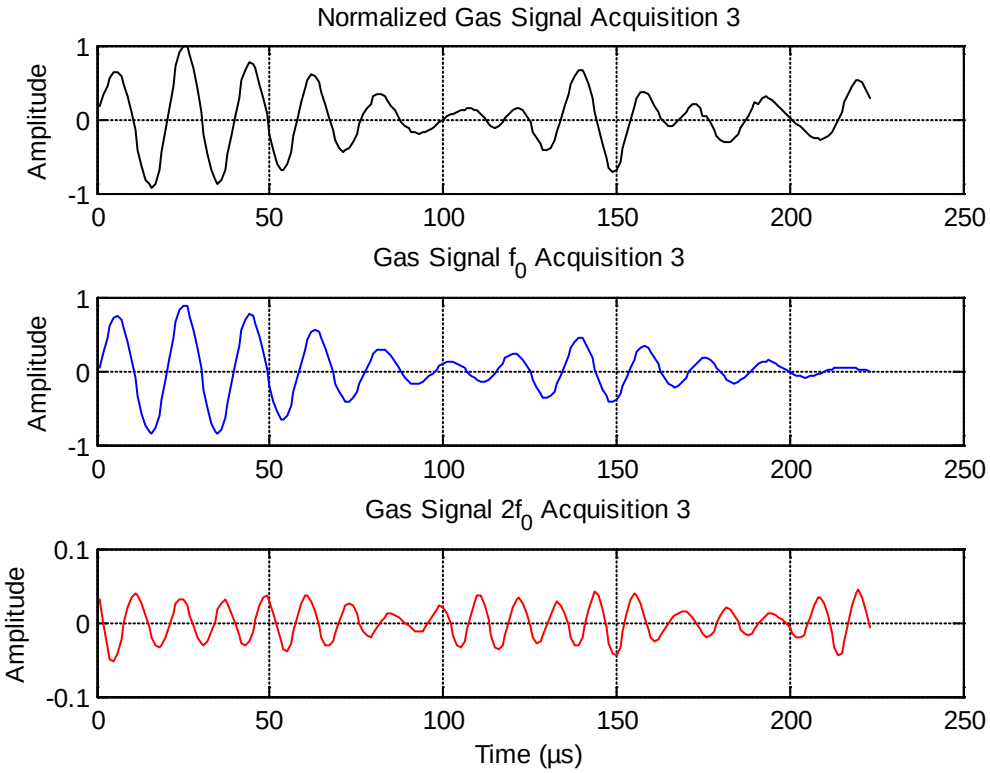

Figure IV.6. Gas signals filtered at f_0 and $2f_0$ for acquisition 3.

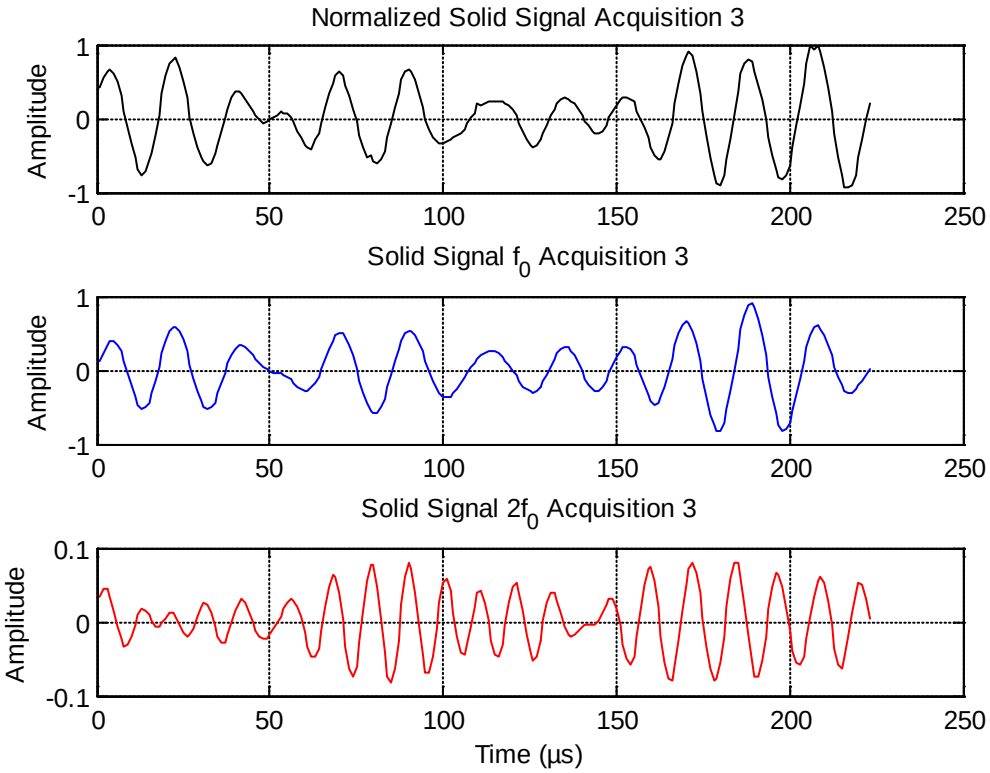

Figure IV.7. Solid signals filtered at f_0 and $2f_0$ for acquisition 3.

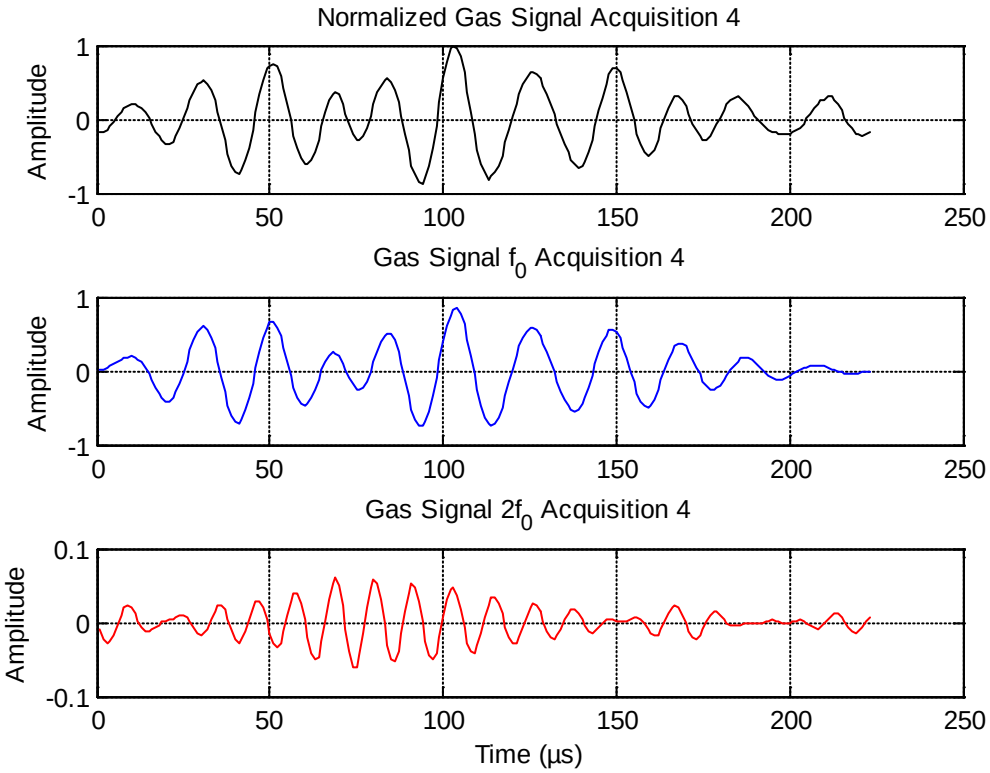

Figure IV.8. Gas signals filtered at f_0 and $2f_0$ for acquisition 4.

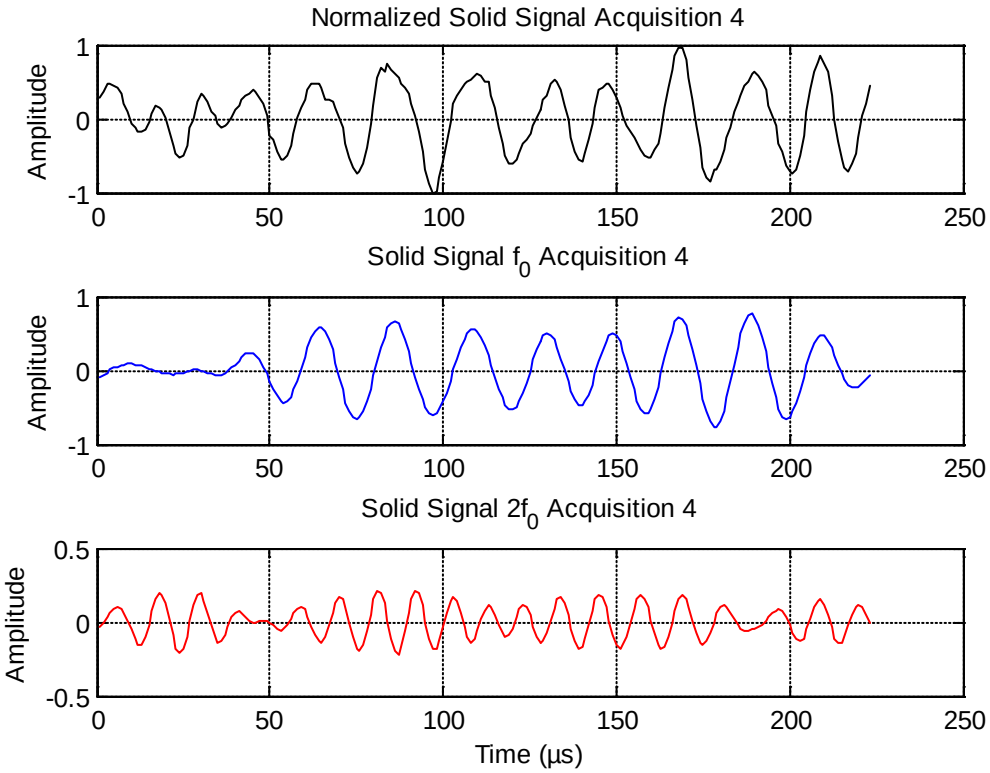

Figure IV.9. Solid signals filtered at f_0 and $2f_0$ for acquisition 4.

In order to extract the amplitudes at the frequencies f_0 and $2f_0$ of the gas and solid signals, we use the Hilbert transform.

The Hilbert transform is a mathematical tool widely used in signal processing for the computation of signal envelope. In mathematics and in signal processing, the Hilbert transform *(Hi)* of a function with real variable *x(t)* is obtained by convolution of the signal *x(t)* with $\frac{1}{\pi.t}$ [99], which gives $\hat{x}(t)$:

$$\hat{x}(t) = Hi[x(t)] = x(t) * \frac{1}{\pi t} = \frac{1}{\pi t}\left[\int_{-\infty}^{+\infty} x(\tau) \cdot \frac{1}{(t-\tau)} \cdot d\tau\right] \qquad \text{(IV. 3)}$$

The envelope of the signal *x(t)* is simply the modulus of *y(t)* [99] where :

$$y(t) = x(t) + jHi[x(t)] \qquad \text{(IV. 4)}$$

Figures IV.10, IV.11, IV.12, and IV.13 show an example of envelopes for gas and solid signals at frequencies f_0 and $2f_0$ for the four acquisitions.

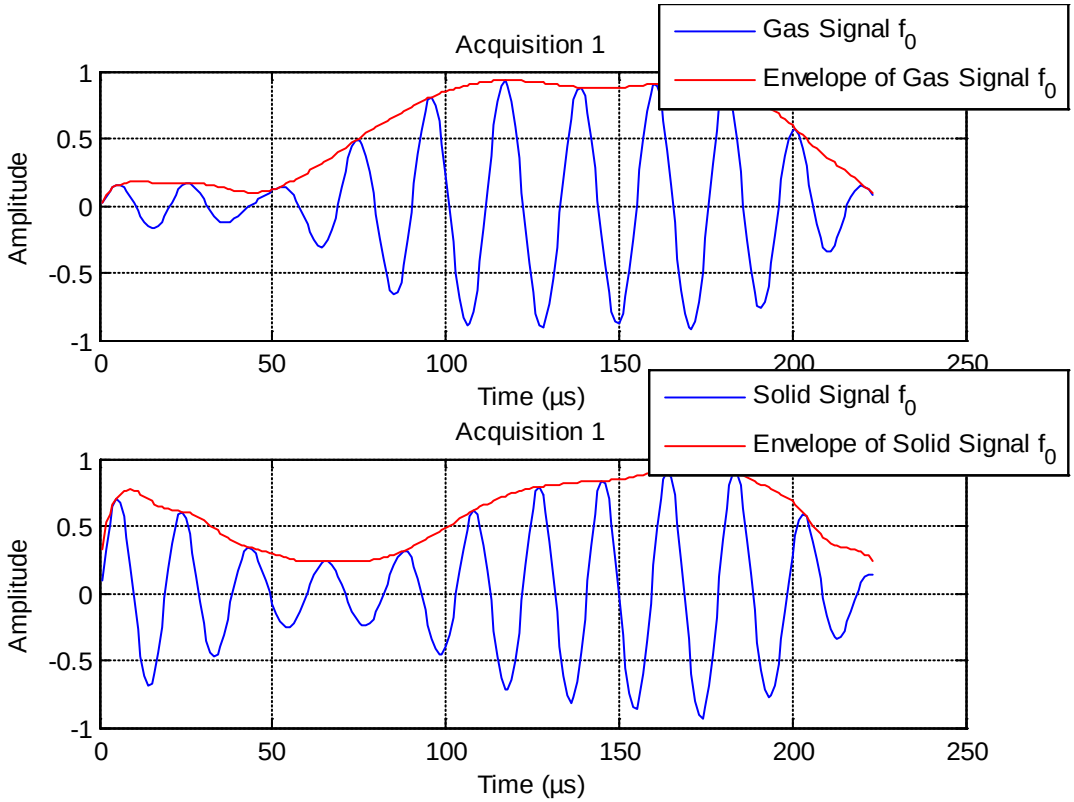

Figure IV.10. Envelope of gas and solid signals at f_0 acquisition 1.

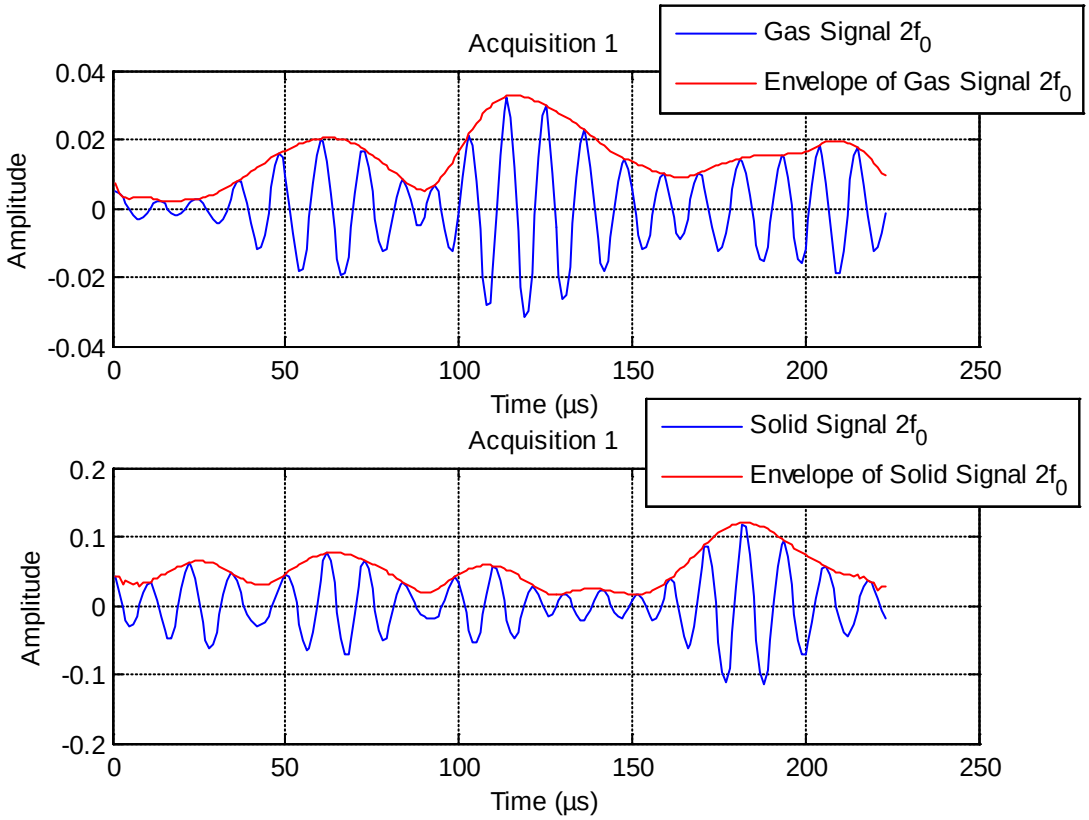

Figure IV.11. Envelope of gas and solid signals at $2f_0$ acquisition 1.

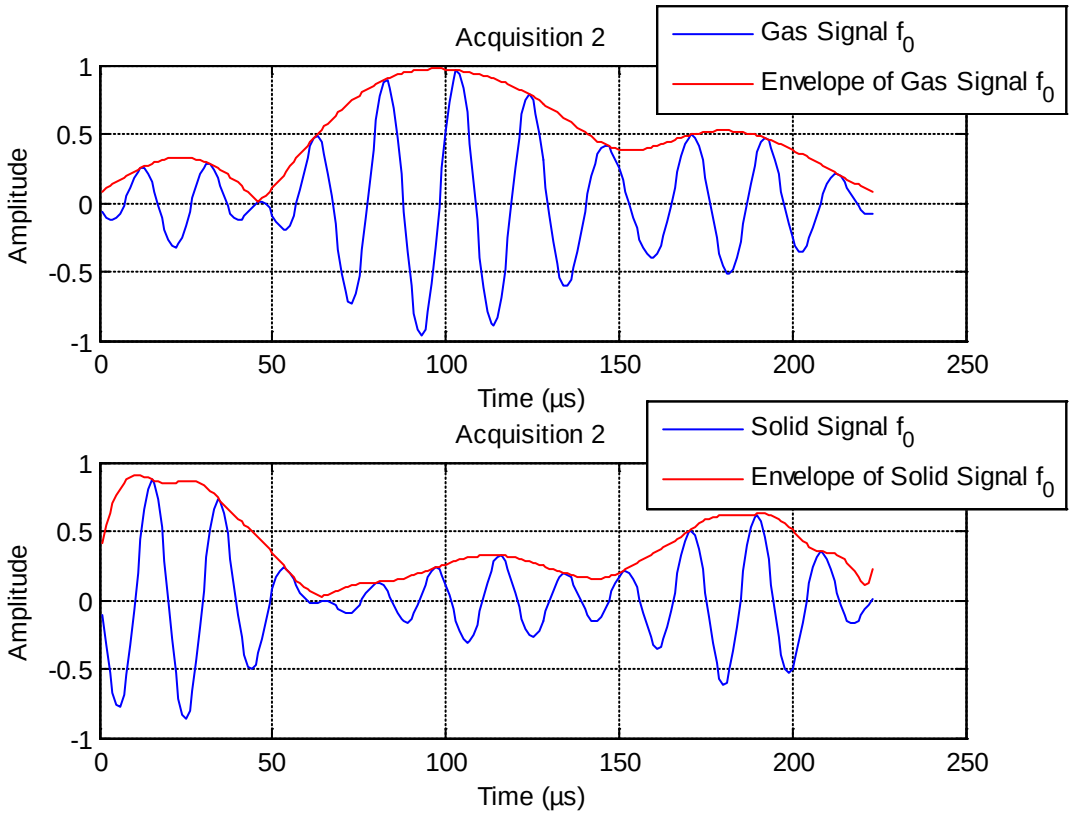

Figure IV.12. Envelope of gas and solid signals at f_0 acquisition 2.

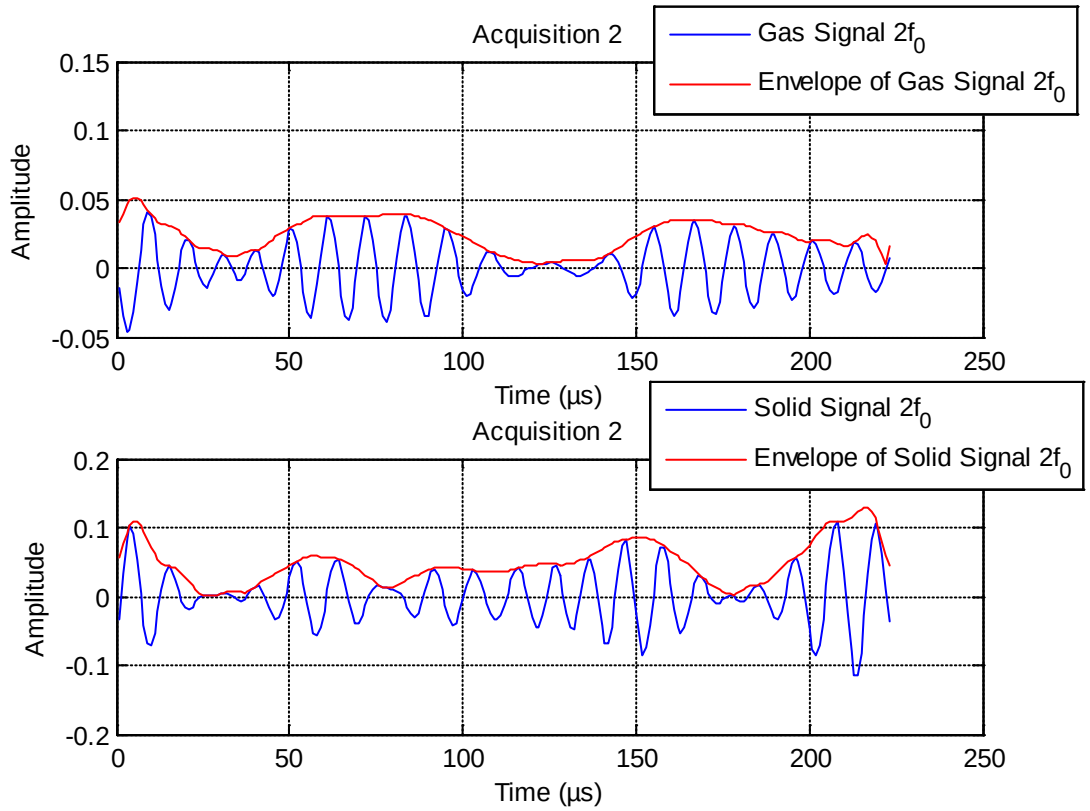

Figure IV.13. Envelope of gas and solid signals at $2f_0$ acquisition 1.

Then the amplitudes at the frequencies f_0 and $2f_0$ are calculated using the following equations:

$$Amp_{f_{0_{gaz}}} = max\left[enveloppe\left(signal_{f_{0_{gaz}}}\right)\right] \quad (IV.5)$$

$$Amp_{2f_{0_{gaz}}} = max\left[enveloppe\left(signal_{2f_{0_{gaz}}}\right)\right] \quad (IV.6)$$

$$Amp_{f_{0_{solid}}} = max\left[enveloppe\left(signal_{f_{0_{solid}}}\right)\right] \quad (IV.7)$$

$$Amp_{2f_{0_{solid}}} = max\left[enveloppe\left(signal_{2f_{0_{solid}}}\right)\right] \quad (IV.8)$$

where,

$Amp_{f_{0_{gaz}}}$, $Amp_{2f_{0_{gaz}}}$: are the amplitudes of gas signals at frequencies f_0 and $2f_0$ respectively.

$Amp_{f_{0_{solid}}}$, $Amp_{2f_{0_{solid}}}$: are the amplitudes of solid signals at frequencies f_0 and $2f_0$ respectively.

IV.2-1.2 Bandwidths of gas and solid signals at f_0 and $2f_0$

Bandwidth is the frequency interval within which the amplitude is not attenuated by more than -3 dB (or half-power bandwidth), which is a factor of $\sqrt{2}$, This can be deduced graphically from Figure IV.14. Indeed, it is sufficient to draw on the *H(dB)* axis a line (*H*=-3dB) and we calculate the difference between the two curves *H(dB)* (frequency response of the filter) and $H = -3dB$ [100].

$$H_{dB} = 20 * log_{10}\left(\frac{|H|}{max|H|}\right), \qquad \text{(IV. 9)}$$

where :

H : Is the frequency response of the filter.

H_{dB} : is the frequency response of the filter in dB.

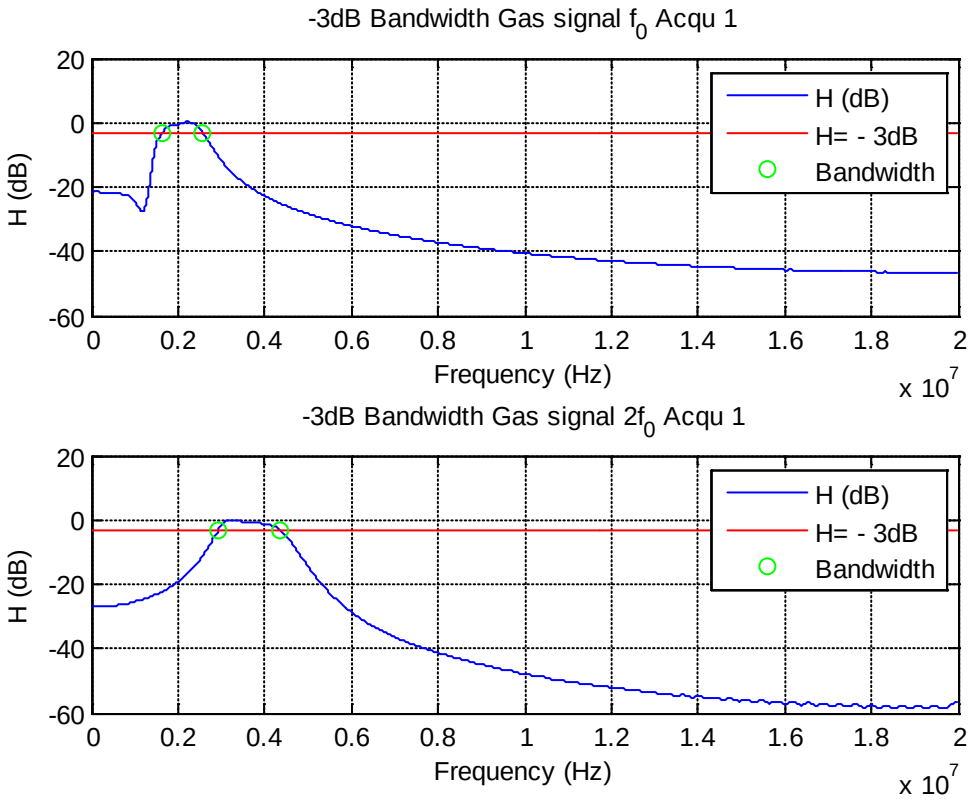

Figure IV.14. Bandwidth of gas signal at f_0 and $2f_0$ acquisition 1.

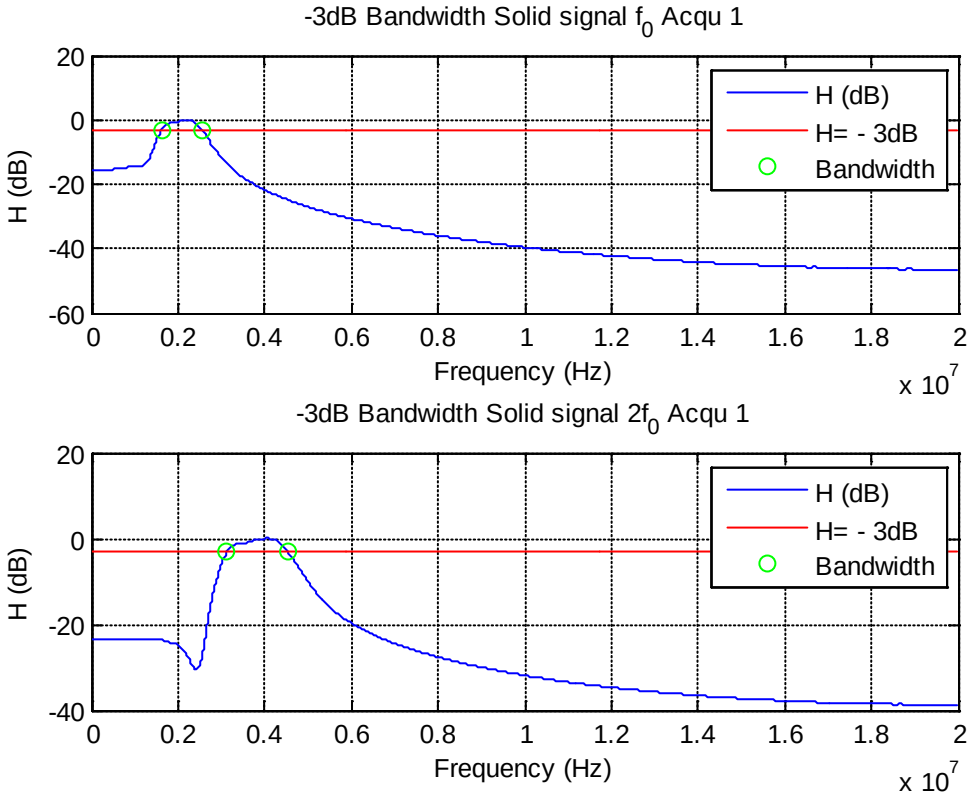

Figure IV.15. Bandwidth of solid signal at f_0 and $2f_0$ acquisition 1.

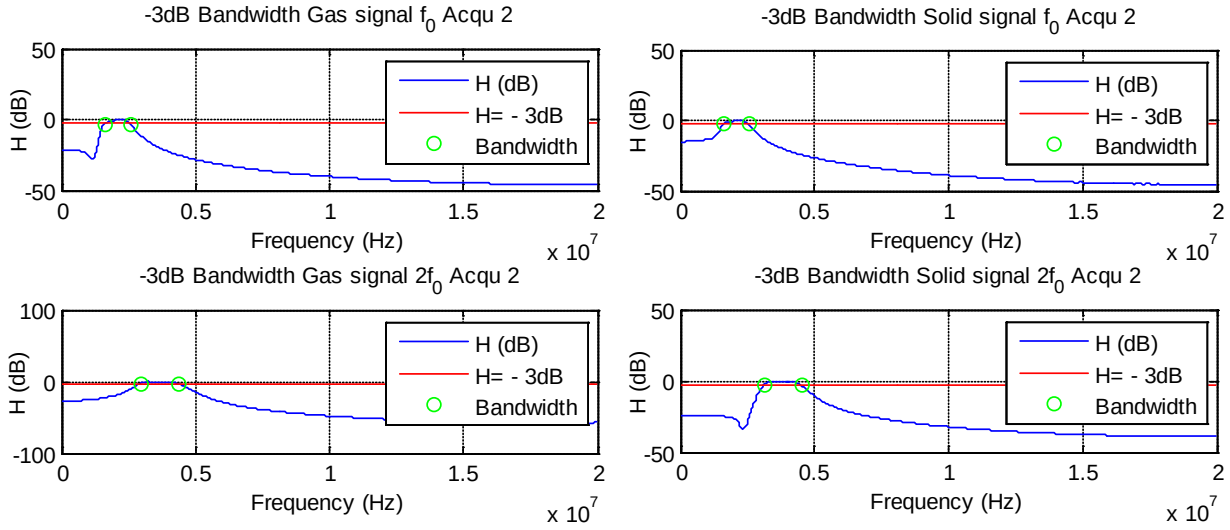

Figure IV.16. Bandwidth of gas and solid signals at f_0 and $2f_0$ acquisition 2.

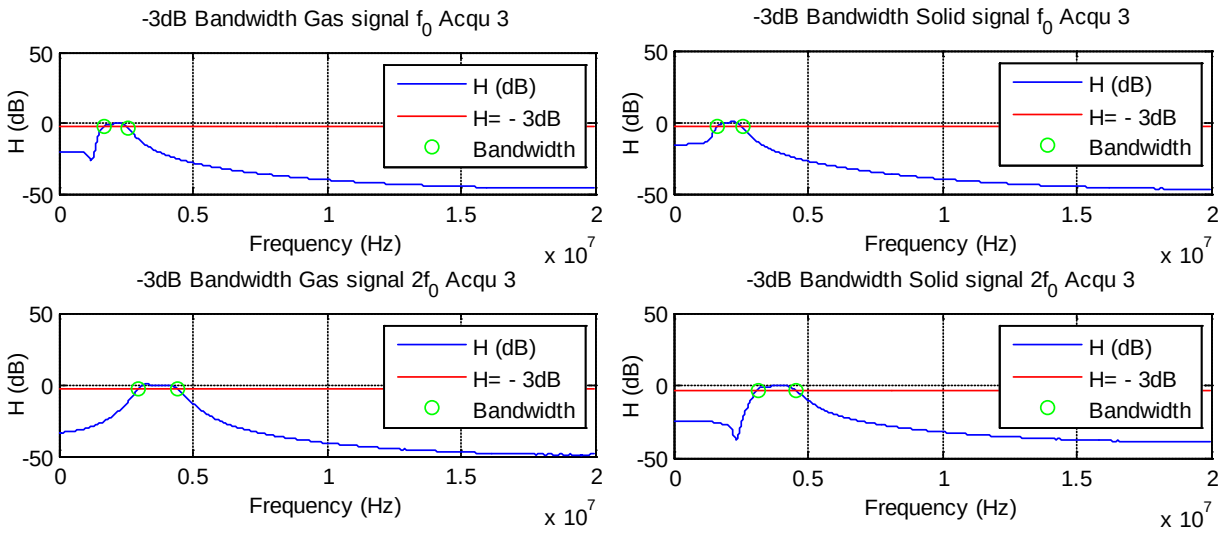

Figure IV.17. Bandwidth of gas and solid signals at f_0 and $2f_0$ acquisition 3.

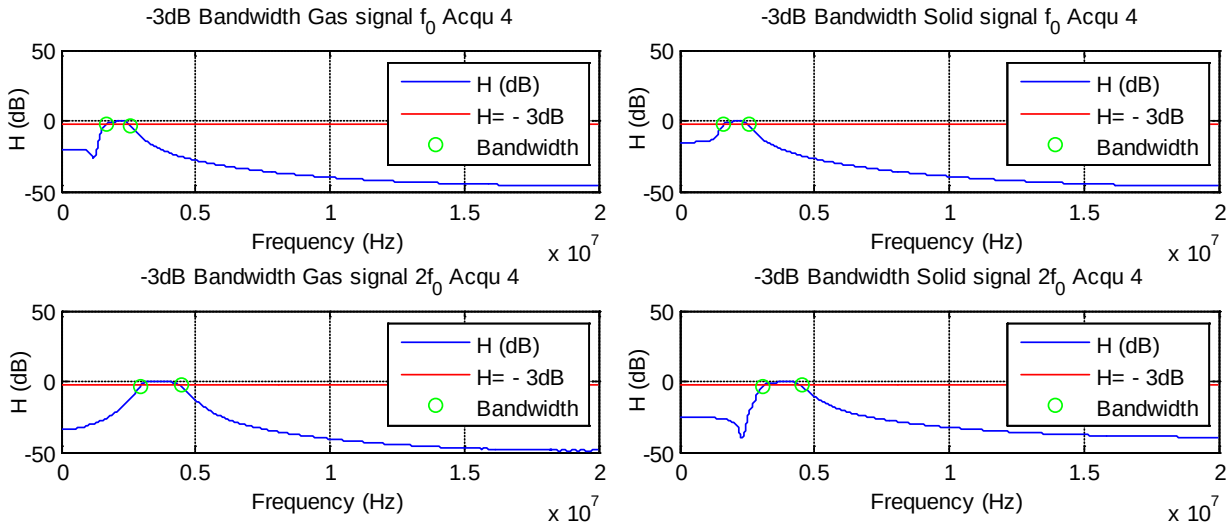

Figure IV.18. Bandwidth of gas and solid signals at f_0 and $2f_0$ acquisition 4.

Figures IV.14, IV.15, IV.16, IV.17, and IV.18 illustrate the obtained bandwidths of gas and solid signals acquired at frequencies f_0 and $2f_0$ for two microbubbles concentrations and two mechanical indices 0.2 and 0.6.

IV.2-1.3 Approximation of the frequency spectra of the fundamental and the second harmonic

In this section the frequency spectra of the fundamental (f_0) and the second harmonic ($2f_0$) are approximated by a Gaussian function (refer to Figure IV.19). In order to perform this approximation, we first need to determine Fourier transform for the filtered gas and solid signals.

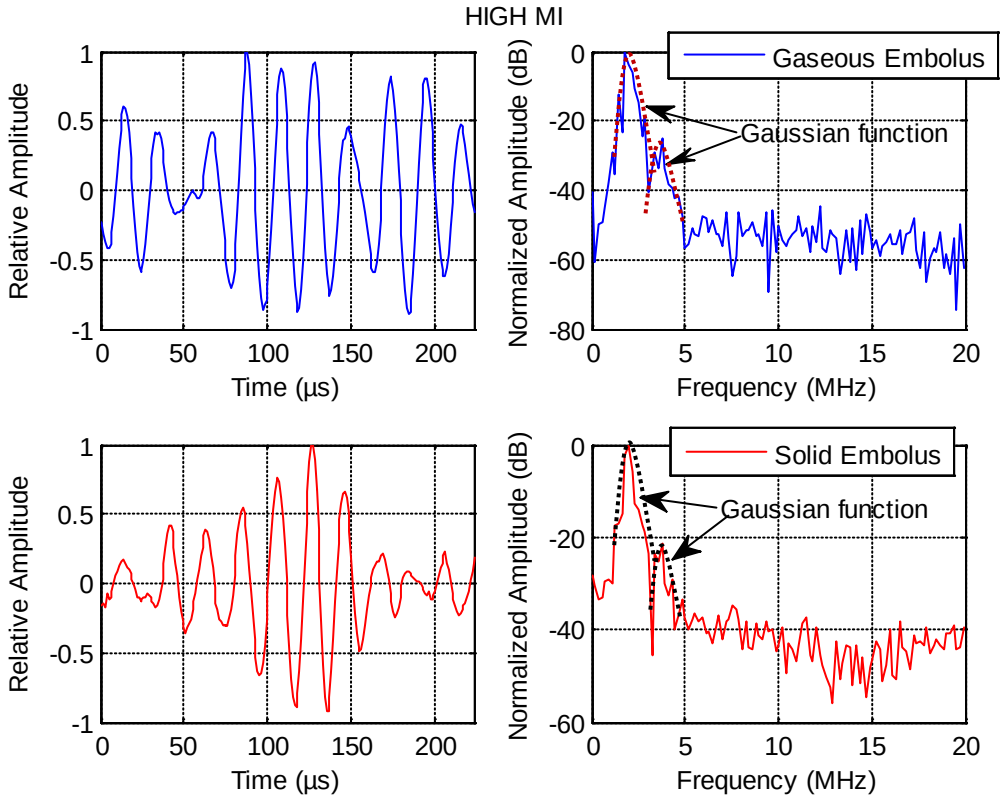

Figure IV.19. Examples RF signals and their corresponding frequency spectrum represented with the Gaussian approximation (dashed line) at high MI

A- Fourier Transform

Lets *s(t)* a deterministic, finite energy signal. Its Fourier transform is a generally complex function of the variable *f* and defined by:

$$S(jf) = TF[s(t)] = \int_{-\infty}^{+\infty} s(t) \cdot e^{-j2\pi ft} \cdot dt \qquad \text{(IV. 10)}$$

Figure IV.20 and IV.21 illustrate Fourier transform of gas signals at frequencies f_0 and $2f_0$ respectively for acquisition 1.

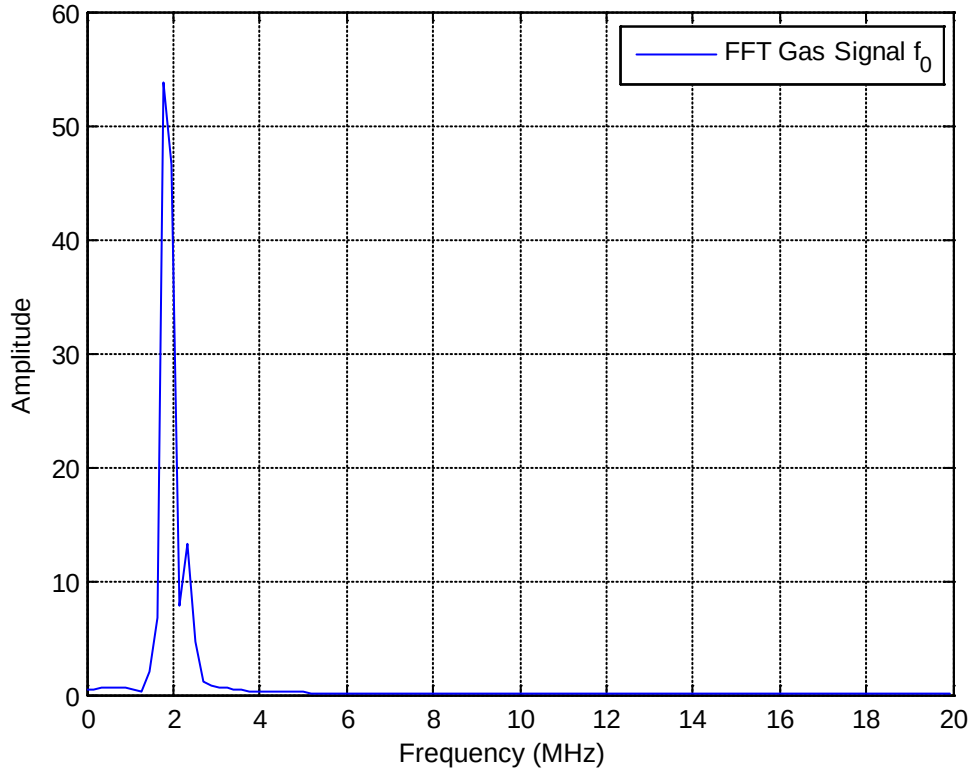

Figure IV.20. Fourier transform of gas signal at fundamental frequency (f_0) Acquisition 1.

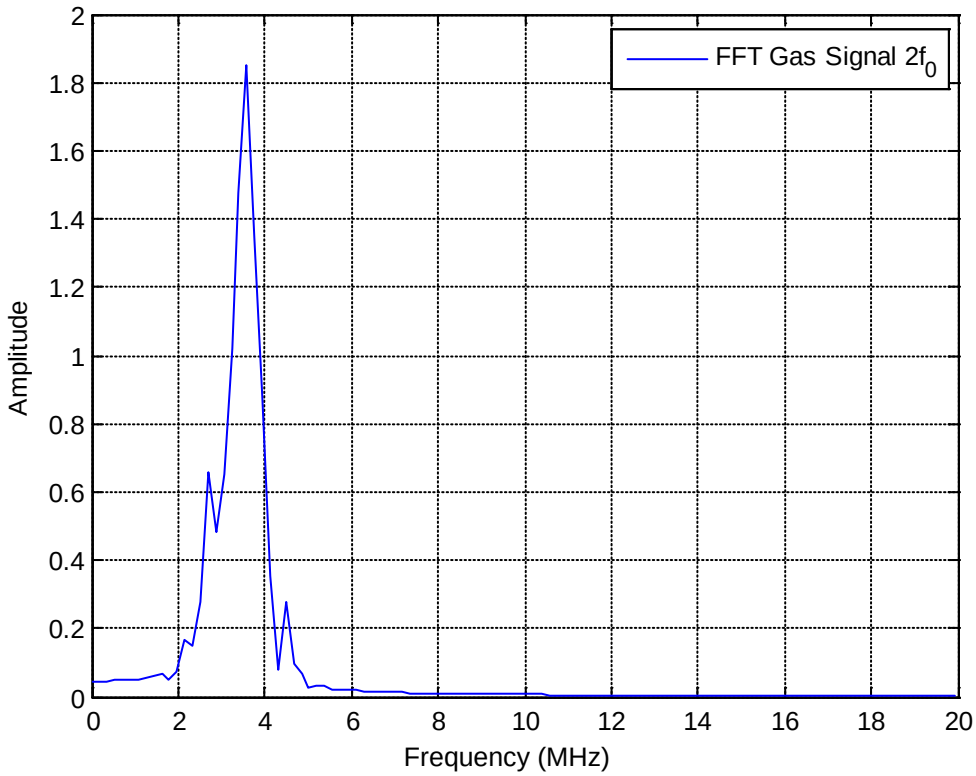

Figure IV.21. Fourier transform of gas signal at second harmonic ($2f_0$) Acquisition 1.

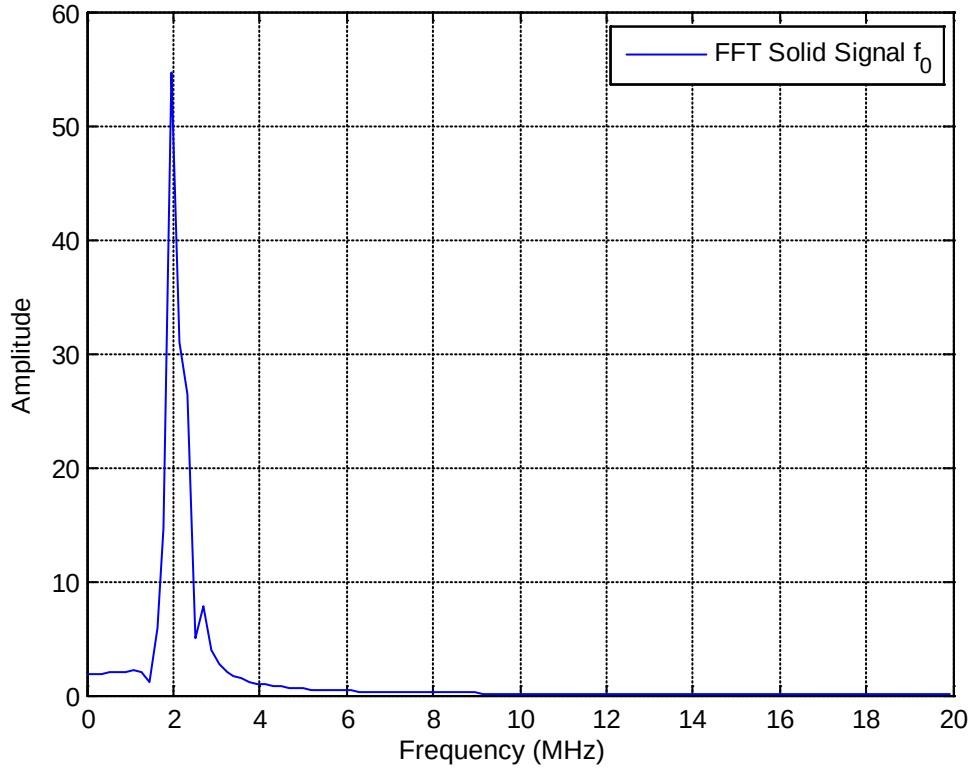

Figure IV.22. Fourier transform of solid signal at fundamental frequency (f_0) Acquisition 1.

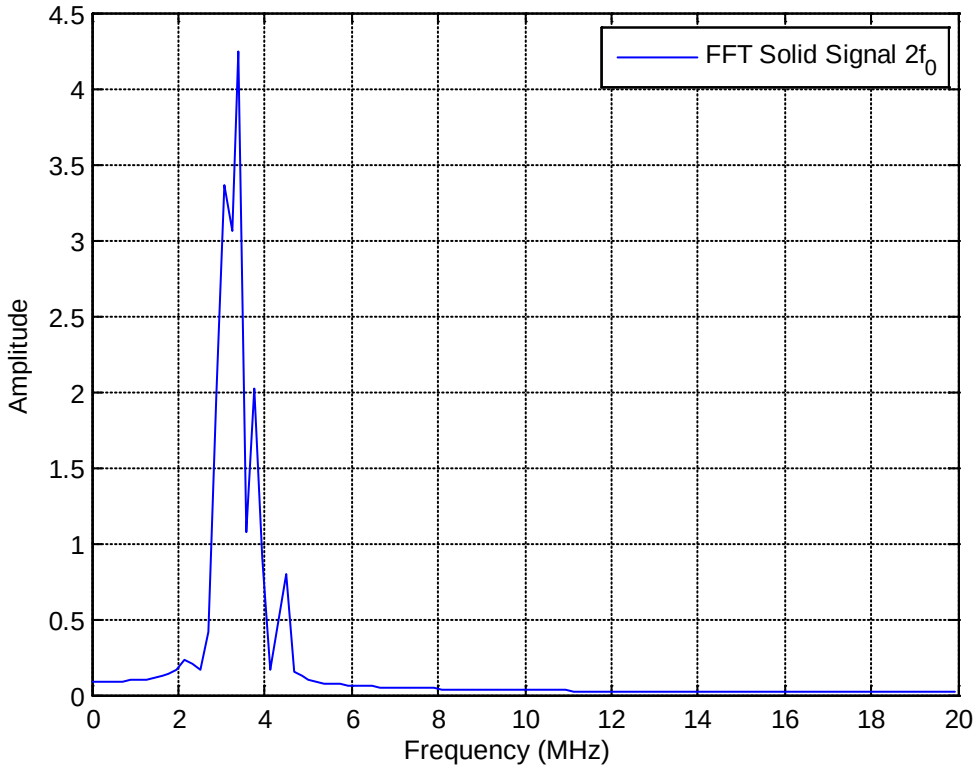

Figure IV.23. Fourier transform of solid signal at second harmonic ($2f_0$) Acquisition 1.

Figure IV.22 and IV.23 illustrates Fourier transform of solid signals at frequencies f_0 and $2f_0$ respectively for acquisition 1.

B- Approximation

In the following, the frequency spectra of the fundamental and the second harmonic are approximated by a Gaussian shape function using the following equation:

$$g(x) = a_1 exp\left(-\left(\frac{(x-b_1)}{c_1}\right)^2\right) \qquad (IV.11)$$

where,

a_1: is the amplitude of the Gaussian,

c_1: is the width of the Gaussian, and

b_1 : is center of the Gaussian.

Once these coefficients are calculated, they are used as input parameter to the classifiers.

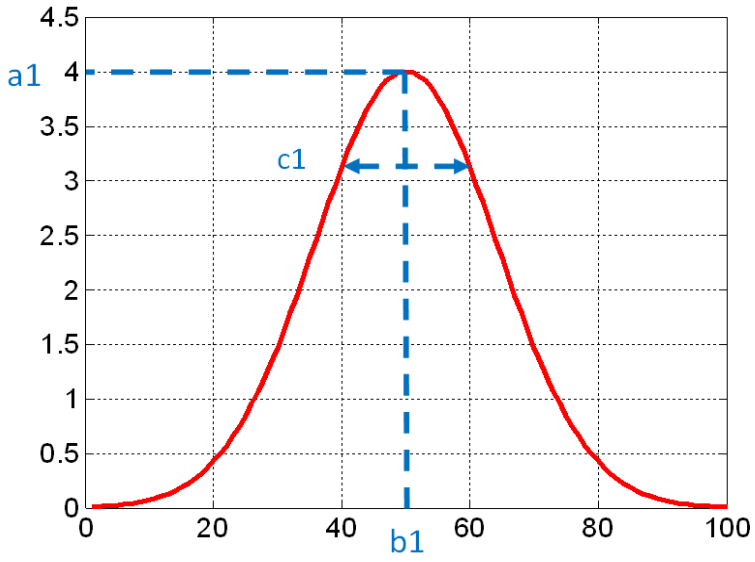

Figure IV.24. Gaussian function with a_1 = 4, b_1 = 50 and c_1 = 20.

Figure IV.24 shows an example of the Gaussian function with a_1 = 4, b_1 = 50, and c_1=20.

C- Quality of adjustment

Once the approximation by the Gaussian functions is constructed, it is vital to check the quality of the adjustment of the models, this can be done using the determination coefficient (R^2) which indicates the strength of the fitting model that illustrates the relationship between the measured and predicted values (R^2 indicates of how well the model fits the data) [94]. The determination coefficient is defined in chapter II section II.4-8.

If the regression is perfect: $R^2 = 1$, if there is no linear relationship between the predicted and the actual values, then R^2 is equal to 0.

The approximation results for the four acquisitions 1, 2, 3 and 4 are shown in Figures IV.25, IV.26, IV.27 and IV.28.

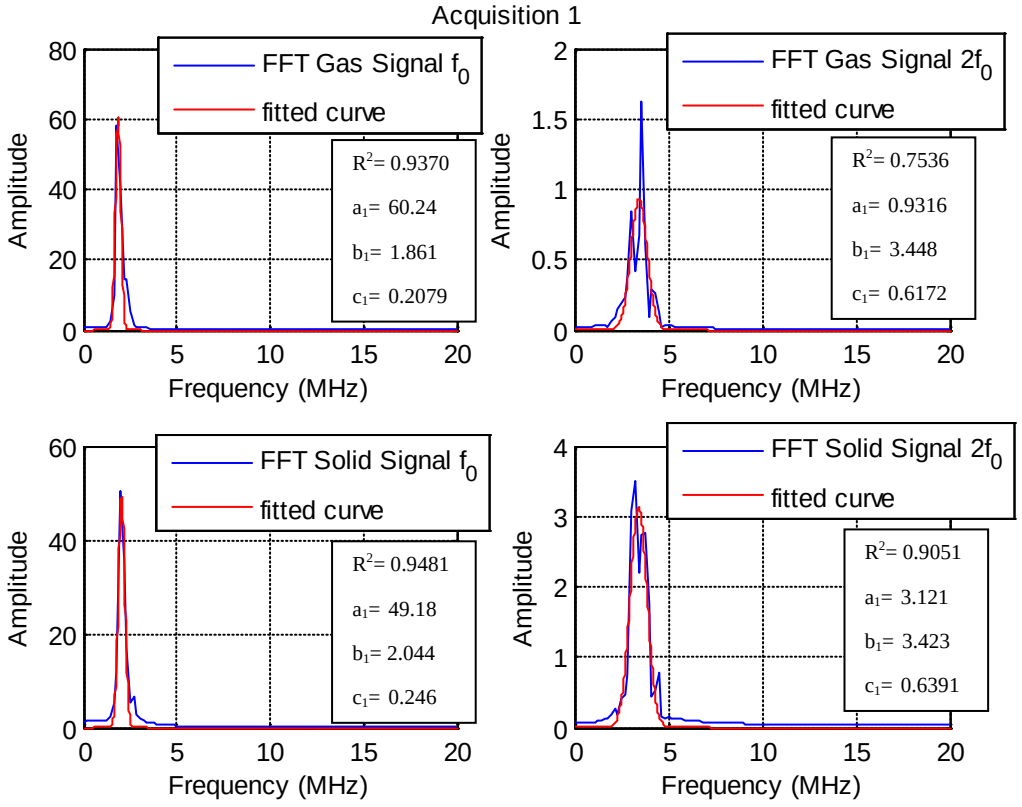

Figure IV.25. Fourier Transforms and their approximations acquisition 1.

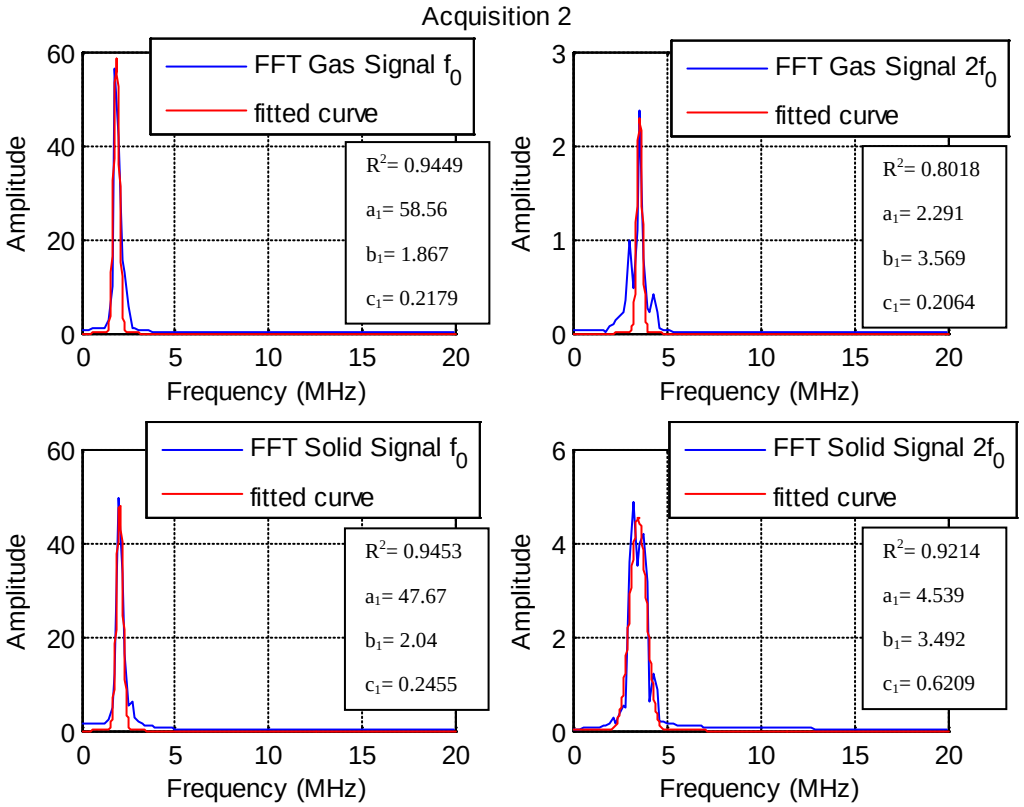

Figure IV.26. Fourier Transforms and their approximations acquisition 2.

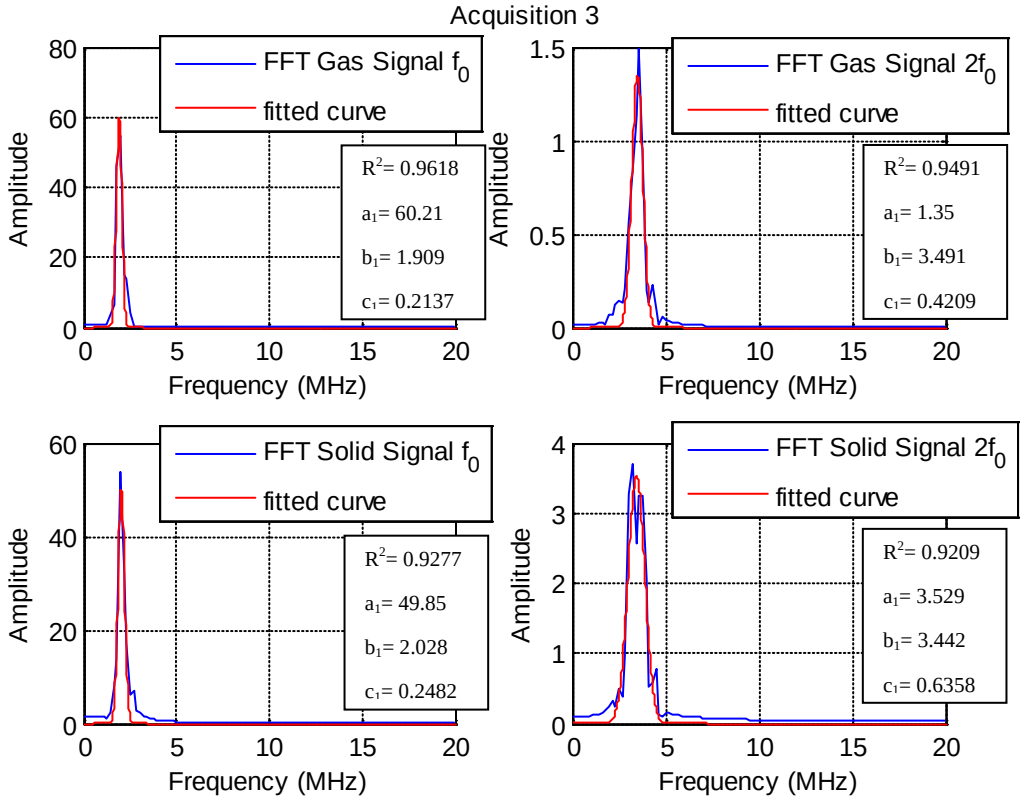

Figure IV.27. Fourier Transforms and their approximations acquisition 3.

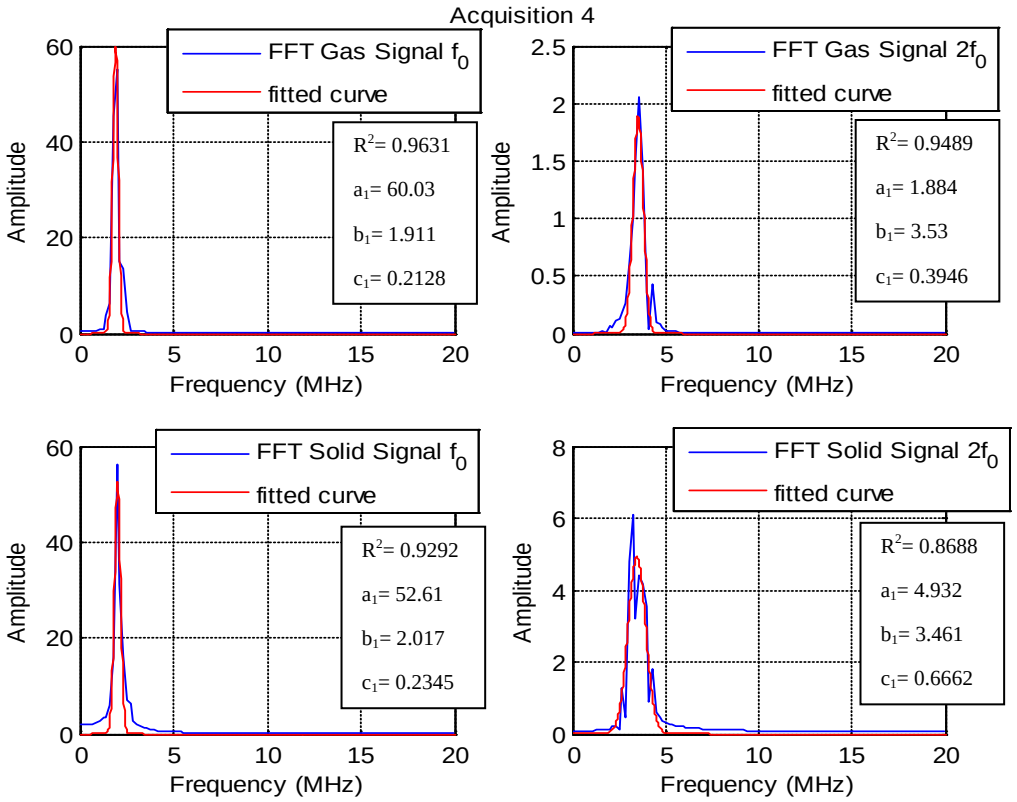

Figure IV.28. Fourier Transforms and their approximations acquisition 4.

Finally, after the construction of feature vector, we obtain four databases each consists of 102 samples (51 solid embolus and 51 gaseous embolus) with a dimension of 10 features (refer to Table IV.1).

Table IV. 1. The obtained 10 features:

1	*BP* f_0	Bandwidth of the scattered RF signals at the fundamental frequency
2	*BP* $2f_0$	Bandwidth of the scattered RF signals at the second harmonic frequency
3	*Amp* f_0	Amplitude at the fundamental frequency
4	*Amp* $2f_0$	Amplitude at the second harmonic frequency
5	*a1* f_0	Amplitude of the Gaussian at the fundamental frequency
6	*b1* f_0	Widths of the Gaussians at the fundamental frequency
7	*c1* f_0	Center of the Gaussian at the fundamental frequency
8	*a1* $2f_0$	Amplitude of the Gaussian at the second harmonic frequency
9	*b1* $2f_0$	Width of the Gaussian at the second harmonic frequency
10	*c1* $2f_0$	Center of the Gaussian at the second harmonic frequency

IV.3 Classification

For binary classification problems with limited number of samples it is crucial to validate the classification model with cross validation technique. Before building the classification model, the samples are often subdivided into three subsets training set, validation set, and test set. The test set is used only for the assessment of the model selected by the cross-validation technique, while the validation set is used to tune the classifiers parameter. Therefore the algorithm has only access to the training and validation sets, the test set is kept unseen in the selection process of the best model.

Our experimental data consists of 102 samples (51 solid embolus and 51 gaseous embolus). In order to evaluate the predictive ability of a model, we randomly divide the dataset, into three subsets training set, validation set, and test set. The test set, approximately one-third (1/3) of the data (14 solid embolus and 14 gaseous embolus), is used only for the assessment of the model selected by the cross-validation technique, while the rest of the data will belong to the learning set (used for building the models) which will be divided into a training set (approximately two-third) and a validation set (approximately one-third). The validation set is used to tune the classifiers parameter.

Artificial Neural Networks (ANN) are widely used in applications involving classification or function approximation. It has been proven that several classes of ANN such as Multilayer Perceptron (MLP) and Radial-Basis Function Networks (RBFN) are universal function approximators. In the next two subsections, we briefly recall the basis of MLP and RBFN models. In order to evaluate the performance of the proposed system, we employ two types of classification algorithms: Multilayer Perceptron and radial basis function neural networks presented in chapter II section II.2.

IV.3-1 Multilayer Perceptron Neural Networks

The most widely used neural classifier today is Multilayer Perceptron (MLP) network which has also been extensively analyzed and for which many learning algorithms have been developed [58]. The MLP (presented in chapter II section II.2.2) belongs to the class of supervised neural networks. MLP networks are general-purpose, flexible, nonlinear models consisting of a number of units organized into multiple layers. The complexity of the MLP network can be changed by varying the number of layers and the number of units in each layer.

IV.3-2 Radial Basis Function Neural Networks

Radial-basis function neural networks (defined in chapter II section II.2.3) can be used for a wide range of applications mainly due to the fact they can approximate any regular function [63] and their training is faster compared to the multilayer perceptron (MLP).

The input nodes in the input layer are equal to the dimension of the input vector. The optimal number of neurons in the hidden layer as well as the spread of the RBFN Gaussian are determined experimentally using cross validation technique. The combination (number of neurons in the hidden layer, spread of the RBFN Gaussian) that results in a model with highest validation accuracy is picked as the best choice of the classification problem. Once the optimal parameters are fixed, the test set is used to validate the selected RBFN model.

IV.4 Results and discussion

Figure IV.29 shows an example of a typical grayscale images obtained at an MI of 0.2 (panel A) and an MI of 0.6 (panel B) for a concentration of microbubbles equal to 0.025µl/ml. The regions of interest corresponding to gaseous and a solid emboli are shown on each of the images.

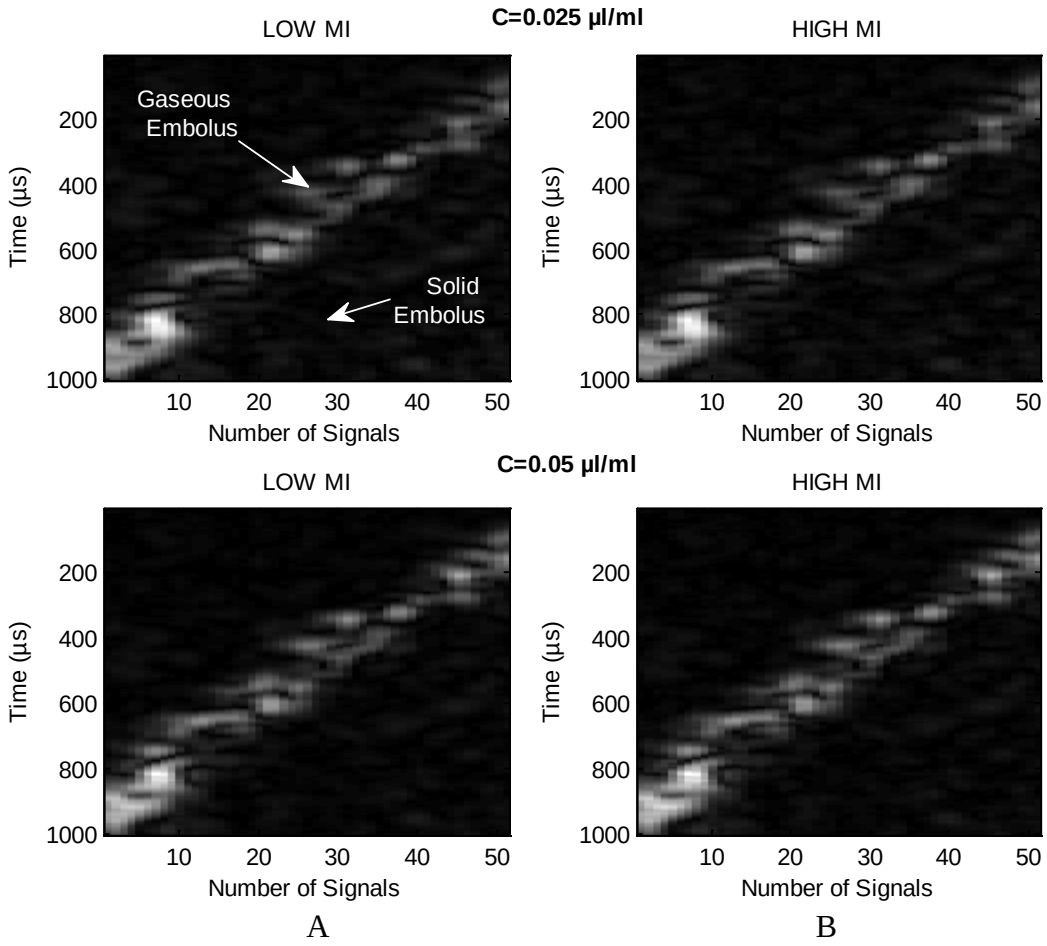

Figure IV.29. Examples of grayscale images acquired: A) at low MI (0.2) and B) high MI (0.6) for two concentrations of microbubbles.

Figure IV.30 displays two examples of RF signals extracted from the regions of interest at the two different mechanical indices. The acoustic pressures are given through the mechanical index as displayed on the scanner monitor. The mechanical index is defined as the peak negative pressure (in MPa) divided by the square root of the frequency (in MHz). Figure IV.30.A displays an RF signal backscattered by solid and gaseous emboli at MI of 0.2. The frequency spectra of both signals include only a component at the fundamental frequency. The acoustic pressure is not sufficiently high to generate nonlinear microbubbles oscillations characterized by the formation of a second harmonic component. Thus the solid embolus responds linearly to the ultrasound excitation in a similar way as the gaseous embolus. At this mechanical index and frequency (0.2 and 1.8 MHz respectively), the peak negative pressure is 260 kPa. The frequency spectra of the scattered signals from the region of the microbubbles do not show any harmonic components and thus we assume that at this acoustic pressure the microbubbles scatter only linearly [24].

Figure IV.30.B shows the scattered RF signals of both solid and gaseous emboli at a higher MI (0.6). We observe for this excitation pressure the generation of nonlinear components at the second harmonic frequency by both gaseous and solid particles. For the case of a gaseous embolus, this component is produced by the nonlinear oscillations of the microbubbles and therefore is considered as a classification parameter since solid embolus scatters only linearly. Nevertheless, at high acoustic pressure (or MI's), which is the case at MI of 0.6; the propagation of an ultrasound wave becomes nonlinear, meaning that harmonic components (2^{nd}, 3^{rd} and higher) are generated in the propagation path. As a consequence, a solid embolus that is located at a distance from the transducer will be hit not only by the main (or fundamental) component but also by the harmonics that are generated during the propagation path. Since a solid embolus scatters linearly, it will scatter all the impinging components including the fundamental and the second harmonic. Thus, and at this applied MI, a generated second harmonic component does not necessarily indicate that a gas bubble is present since it can be generated during the nonlinear propagation process. Therefore the frequency spectrum of the signal backscattered by a solid embolus will also include some nonlinear components. Since these nonlinear propagation effect will contaminate the scattering nonlinearity of the gas microbubbles, the harmonic generation cannot be used as the only discrimination factor between solid and gaseous matter [24].

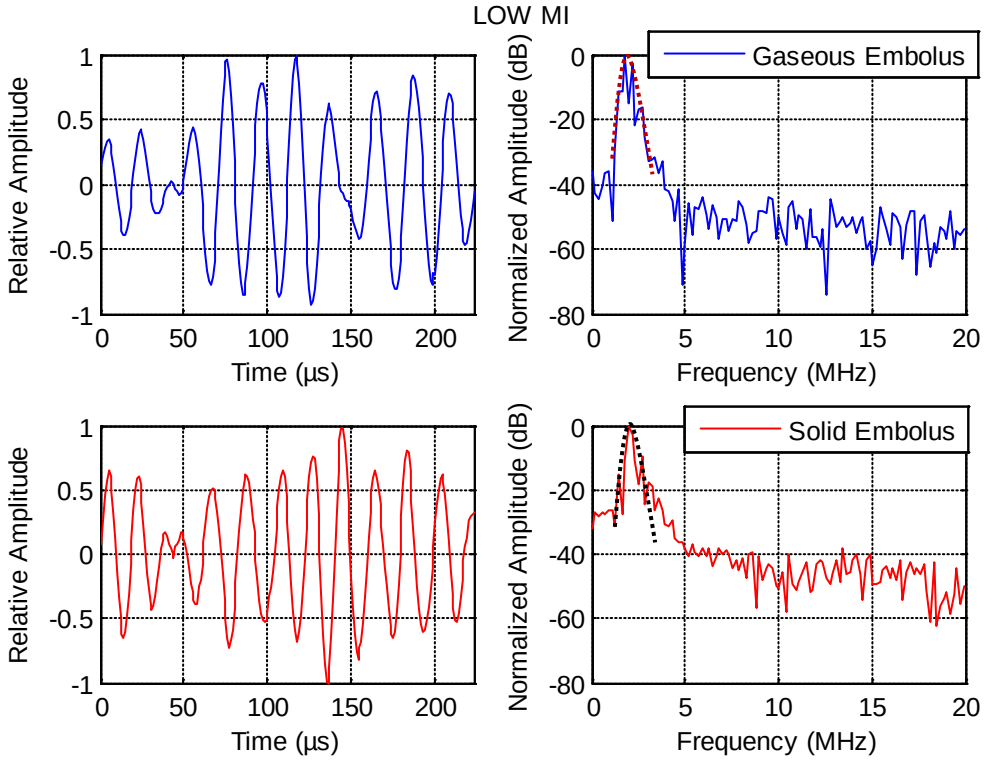

A

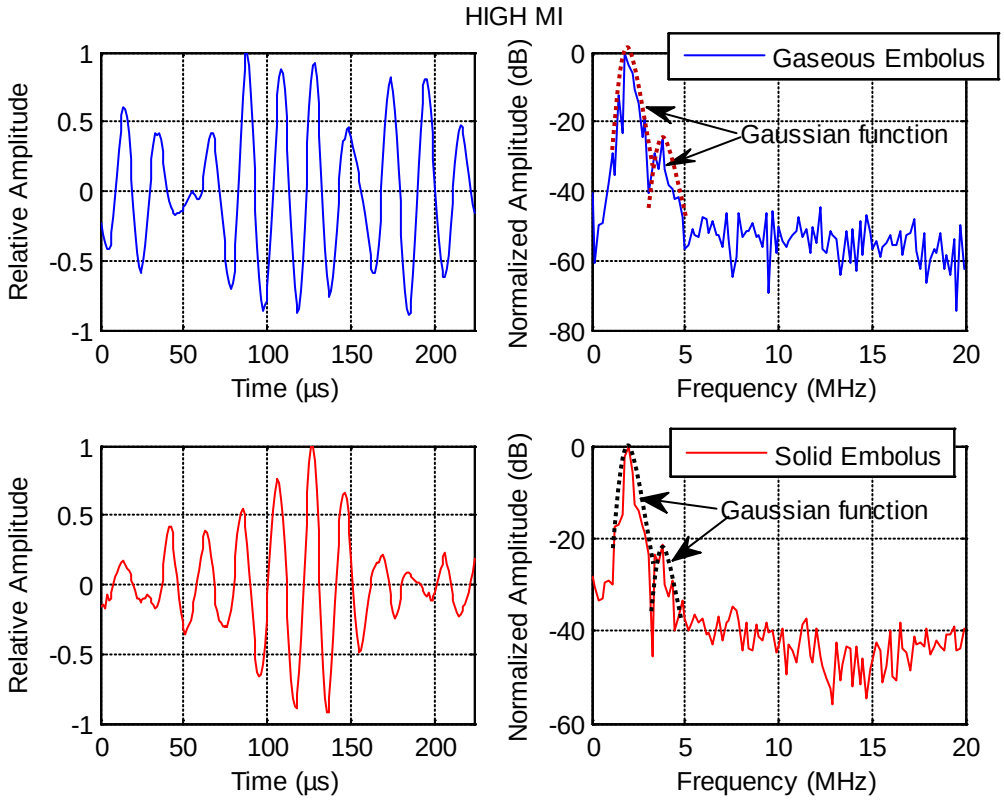

B

Figure IV.30. Examples RF signals and their corresponding frequency spectrum represented with the Gaussian approximation (dashed line) : A) at low MI ; B) high MI.

Table IV.2 and Table IV.3 summarize the percentage of correct classification of microemboli using the MLP and RBFN analysis as a function of the different input parameters and the mechanical index for the two microbubble concentrations 0.025µl/ml and 0.05µl/ml.

The bandwidths of the linear and nonlinear components for the two concentrations do not provide a significant average rate of classification neither at the low MI (0.2) and nor at the high MI (0.6). Only 50% of classification rate is obtained for both models (RBFN and MLP) using the bandwidths as input parameter. When amplitudes of the fundamental and the second harmonic components are introduced as input parameters into the neural networks models, the correct average rate of classification of microemboli at high MI (0.6) reached 87.5% for the RBFN classifier and 82.14% for the MLP classifier for the higher concentration. At the low microbubble concentration (0.025µl/ml), the correct average rates of classification for microemboli at high MI (0.6) are 83.13% and 78.56% for RBFN and MLP models respectively. Here, we talk about RF signal scattered from the microbubbles (gas emboli) or surrounding tissue (solid emboli), its FFT is calculated. The amplitudes at the fundamental frequency and at the second harmonic frequency are selected. These values are used as an input parameter [24].

Figure IV.31 shows the results of classification for the Gaussian coefficients of the spectral envelopes when used as input parameters in both neural network models (RBFN and MLP). The highest classification rate reached a value of 92.85% for the RBFN model at high MI (0.6). Using the MLP model, the Gaussian coefficients provided a classification rate of 89.28% at high MI (0.6) for both microbubble concentrations. These high classification rates might be ascribed to the fact that the coefficients of the spectral envelopes contain additional information about the bandwidths and the amplitudes of the linear and nonlinear components of the backscattered signals from both solid and gaseous emboli [24].

Table IV. 2. Classification rates of the MLP and RBFN models with concentration of microbubbles (0.05µl/ml) at low MI (0.2) and high MI (0.6) for three different input parameters: the bandwidths and the amplitudes of the fundamental and the second harmonic and the Gaussian parameters issued form Equation (IV.11) [24]:

Results with MLP C =0.05µl/ml	Bandwidths		Amplitudes		Gaussian Coefficients	
	Low MI	High MI	Low MI	High MI	Low MI	High MI
Gaseous Emboli	0%	0%	100%	100%	85.71%	78.57%
Solid Emboli	100%	100%	64.28%	64.28%	85.71%	100%
Average rate	50%	50%	82.14%	82.14%	85.71%	**89.28%**
Results with RBFN C =0.05µl/ml	Bandwidths		Amplitudes		Gaussian Coefficients	
	Low MI	High MI	Low MI	High MI	Low MI	High MI
Gaseous Emboli	0%	0%	78.57%	85.71%	92.85%	85.71%
Solid Emboli	100%	100%	71.42%	85.71%	78.57%	100%
Average rate	50%	50%	74.99%	85.71%	85.71%	**92.85%**

Table IV. 3. Classification rates of the MLP and RBFNmodels with concentration of microbubbles (0.025µl/ml) at low MI (0.2) and high MI (0.6) for three different input parameters: the bandwidths and the amplitudes of the fundamental and the second harmonic and the Gaussian parameters issued form Equation (IV.11) [24]:

Results with MLP C =0.025µl/ml	Bandwidths		Amplitudes		Gaussian Coefficients	
	Low MI	High MI	Low MI	High MI	Low MI	High MI
Gaseous Emboli	0%	0%	71.42%	71.42%	92.85%	78.57%
Solid Emboli	100%	100%	85.71%	78.57%	85.71%	100%
Average rate	50%	50%	78.56%	78.56%	**89,28%**	**89.28%**
Results with RBFN C =0.025µl/ml	Bandwidths		Amplitudes		Gaussian Coefficients	
	Low MI	High MI	Low MI	High MI	Low MI	High MI
Gaseous Emboli	0%	0%	78.57%	71.42%	78.57%	92.85%
Solid Emboli	100%	100%	92.85%	92.85%	78.57%	85.71%
Average rate	50%	50%	85.71%	83.13%	78.57%	**89.28%**

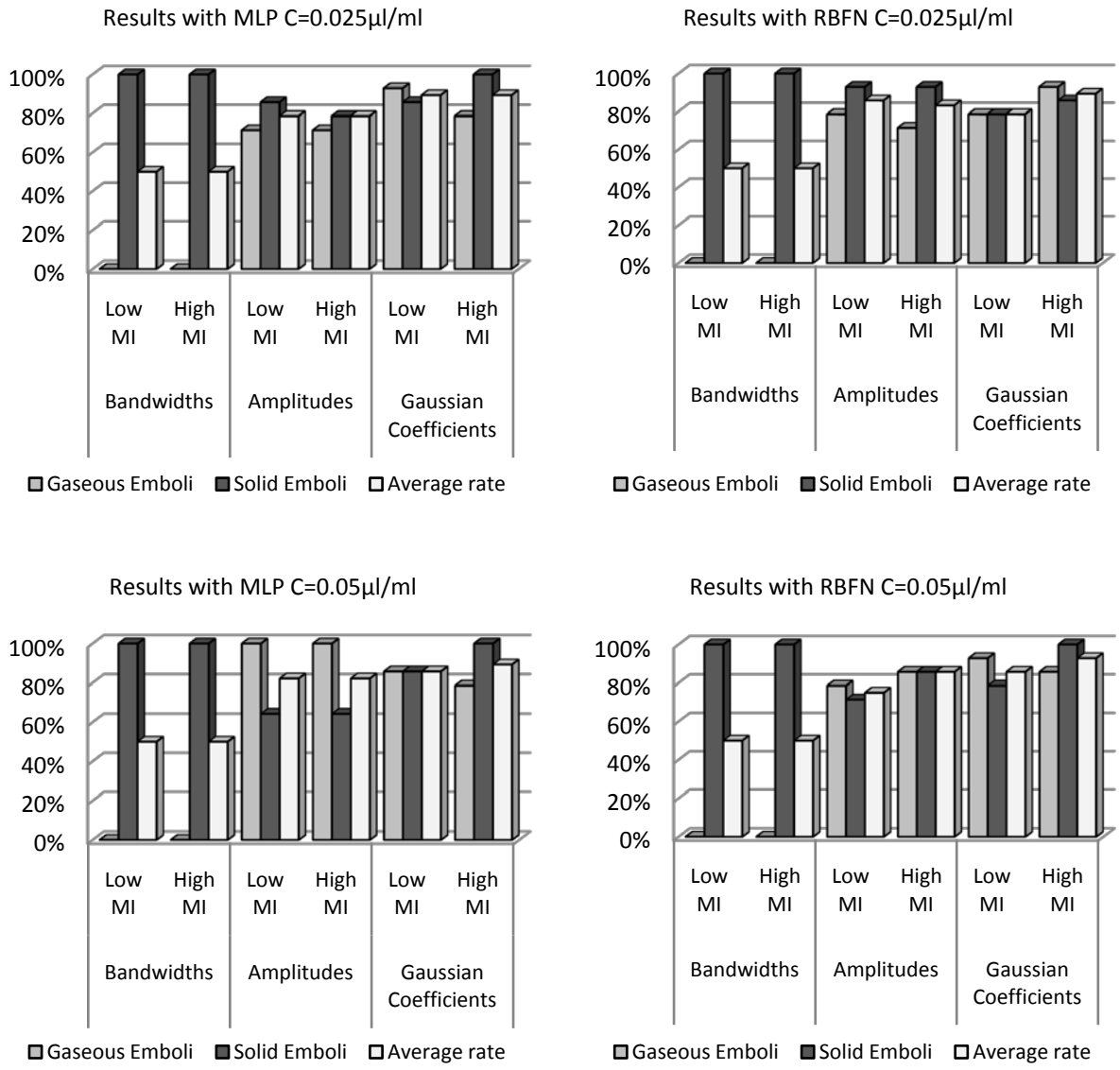

Figure IV.31. Classification rates of gaseous and solid emboli with the two concentrations of microbubbles at low and high MI (0.6) for three different input parameters [24].

Figure IV.32 and Figure IV.33 show the best model obtained for embolus classification using MLP and RBFN with concentration of microbubbles 0.025µl/ml at low (0.2) and high MI (0.6) respectively. For our data, in the classification process the threshold is set to 0.5 to have an initial probability of 0.5 (half) for both solid and gaseous embolus. In a clinical situation, the threshold can be set to a different value depending on the application.

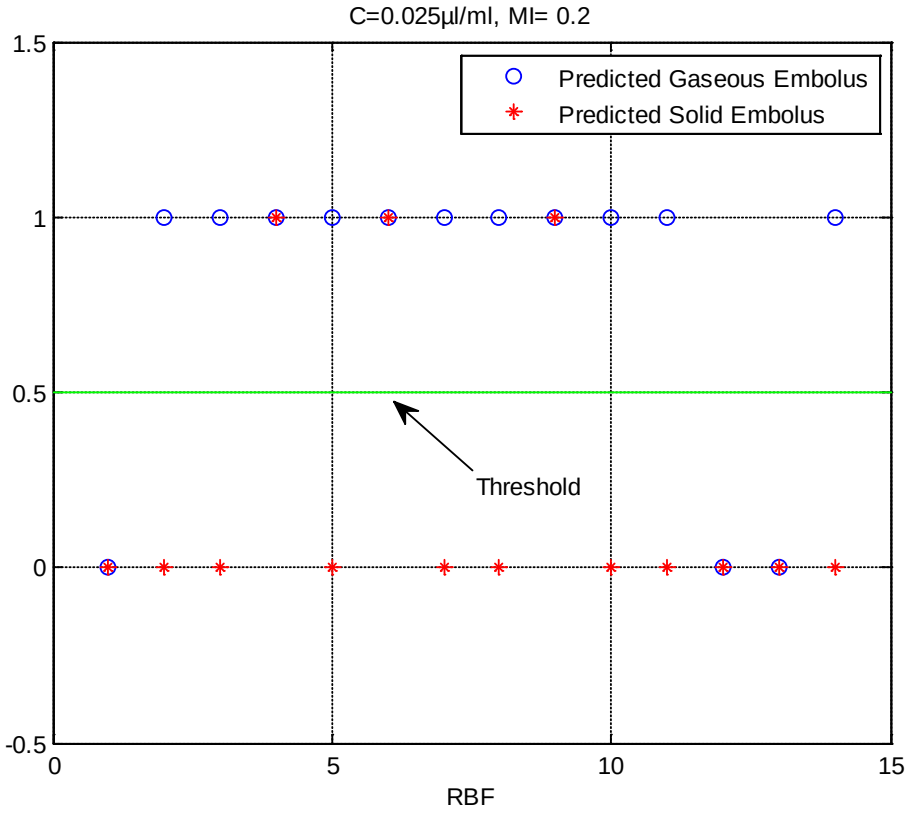

A

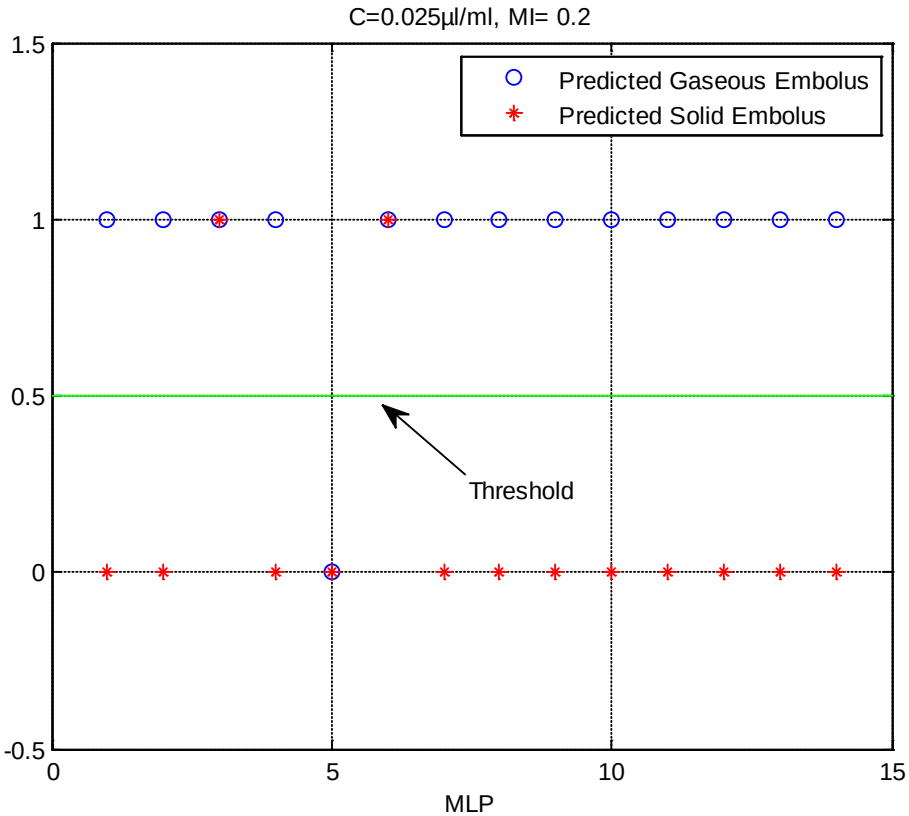

B

Figure IV.32. Embolus classification using MLP and RBFN with concentration of microbubbles of 0.025µl/ml at low MI, (A) MLP; B) RBFN using Gaussian Coefficients.

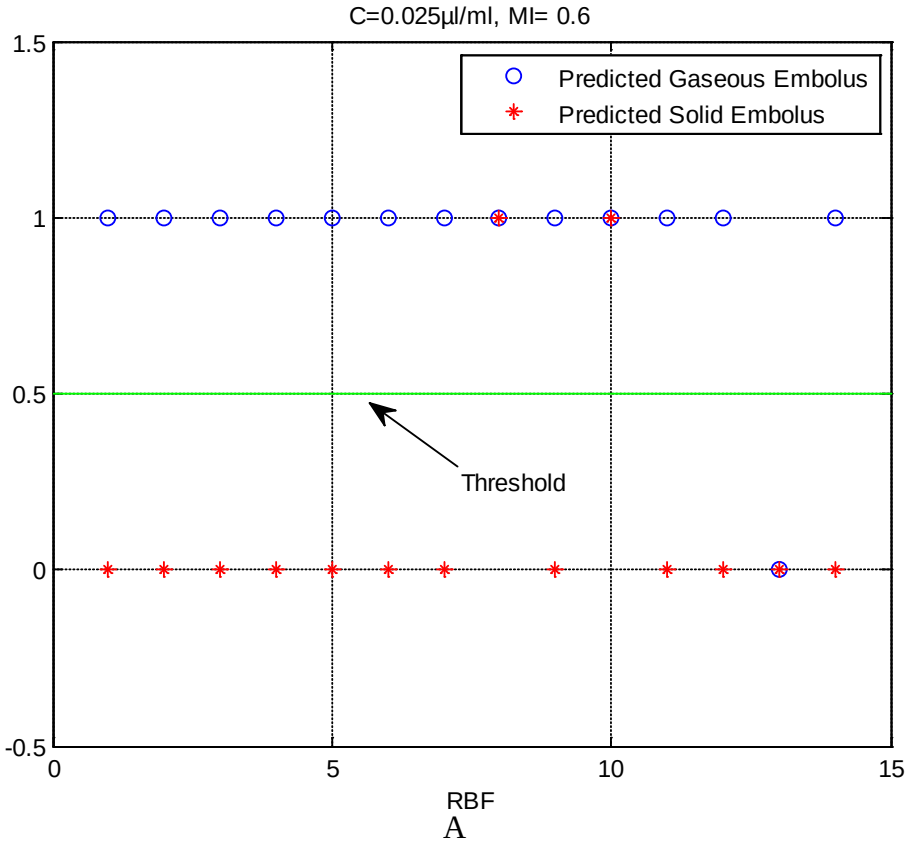

A

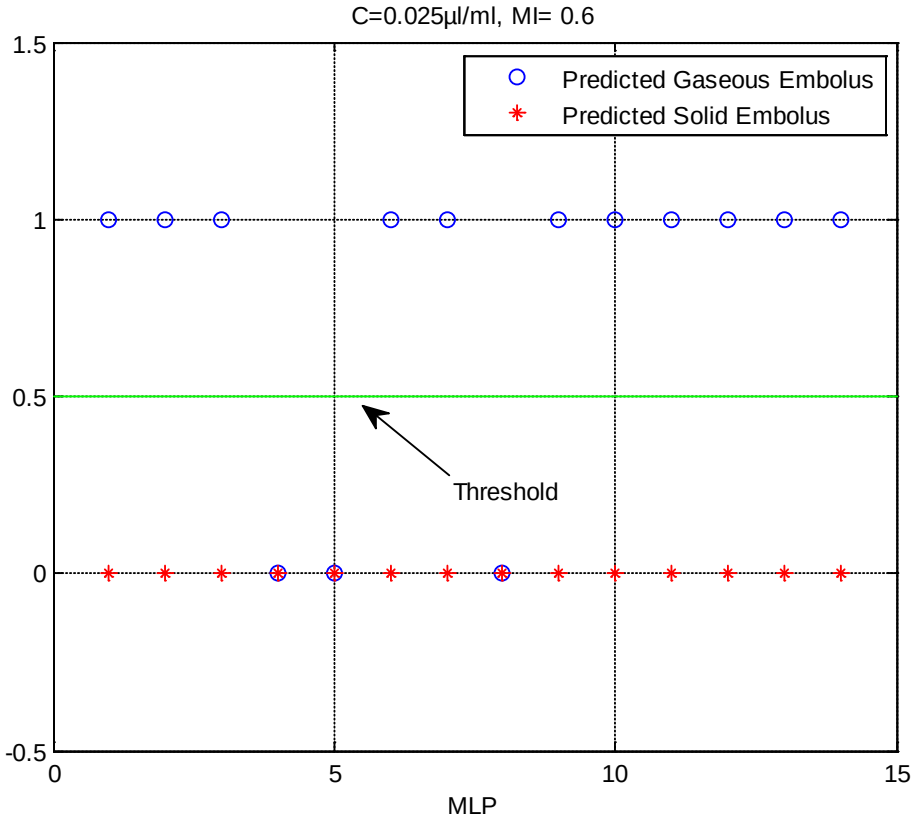

B

Figure IV.33. Embolus classification using MLP and RBFN with concentration of microbubbles of 0.025µl/ml at high MI, (A) MLP; B) RBFN using Gaussian Coefficients.

An output value of 1 corresponds to the gaseous embolus represented by circles and an output value of 0 corresponds to the solid embolus represented by stars. For example, Figure IV.32.A, corresponding to low MI (0.2) shows that the RBFN classification model used in this experiment succeeded in classifying 11 gaseous embolus out of 14 and 11 solid embolus out of 14 also. On the other hand, the MLP classification model used for the same experiment succeeded in classifying 13 gaseous embolus out of 14 and 12 solid embolus out of 14.

Table IV. 4. Confusion matrix of the proposed MLP model using Gaussian Coefficients

Gaussian coefficients		**Results with MLP (C = 0.025µl/ml)**			
		Predicted			
		Low MI (0.2)		**High MI (0.6)**	
		Gaseous emboli	Solid emboli	Gaseous emboli	Solid emboli
Actual class	Gaseous emboli	13	1	11	3
	Solid emboli	2	12	0	14
		Results with MLP (C = 0.05µl/ml)			
		Predicted			
		Low MI (0.2)		**High MI (0.6)**	
		Gaseous emboli	Solid emboli	Gaseous emboli	Solid emboli
Actual class	Gaseous emboli	12	2	11	3
	Solid emboli	2	12	0	14

Table IV. 5. Confusion matrix of the proposed RBFN model using Gaussian Coefficients

Gaussian coefficients		**Results with RBFN (C = 0.025µl/ml)**			
		Predicted			
		Low MI (0.2)		**High MI (0.6)**	
		Gaseous emboli	Solid emboli	Gaseous emboli	Solid emboli
Actual class	Gaseous emboli	11	3	13	1
	Solid emboli	3	11	2	12

		Results with RBFN (C = 0.05µl/ml)			
		Predicted			
		Low MI (0.2)		**High MI (0.6)**	
		Gaseous emboli	Solid emboli	Gaseous emboli	Solid emboli
Actual class	Gaseous emboli	13	1	12	2
	Solid emboli	3	11	0	14

Table IV.4 and Table IV.5 illustrate the confusion matrix of the proposed neural network models (MLP and RBFN respectively) using Gaussian coefficients. The numbers of correct and incorrect predictions made by the two models compared to the target values in the test data are shown in these two tables. For example, at microbubble concentration 0.05 µl/ml at high MI (0.6) the proposed RBFN classification model succeeded in classifying 12 gaseous embolus out of 14 (Sensitivity=85.71%) and 14 solid embolus out of 14 (Specificity =100%). Thus 2 gaseous embolus are not recognized i.e. classified as solid embolus, the solid embolus are all recognized.

The processing time is an important issue if we have to implement this technique in a clinical machine. However the main objective of our study is only to evaluate the performances of the proposed approach in classifying the emboli. Therefore, we did not focus on the time of processing the data. Obviously, MATLAB will not be used as a processing tool since other software packages are more appropriate. Nevertheless, it should be noted that the training phase for the MLP network lasts for a few minutes while the training phase for RBFN network takes less than one minute. The processing time for the test phase (classification) is less 1 second. The current emboli classification techniques are performed in real time using TCD machines since this differentiation is observed in the Doppler signal.

IV.5 Conclusion

This chapter demonstrates the usefulness of exploiting RF signals instead of Doppler signals for a better classification of microemboli as solid or particulate matter. A neural network (MLP or RBFN) analysis using the fundamental and the second harmonic components information contained in the RF signal backscattered by an embolus allows the classification with a classification rate of 92.85%. Furthermore, the strategy to construct the feature vector employed in the classification section is presented. We evaluate the predictive power of a set of three feature extraction approaches and two different classifiers.

The following features are selected as input parameters to the neural network (MLP or RBFN) models:

1- The bandwidths of the scattered RF signals at the fundamental and at the second harmonic frequencies.

2- The amplitudes at the fundamental frequency and at the second harmonic frequency.

3- The frequency spectra of the fundamental and the second harmonic are approximated by a Gaussian function.

Chapter V: Particle Characterization Using Wavelet Based Approach and SVM Based Dimensionality Reduction

V.1 Introduction

A number of researchers have reported that discrete wavelet transform (DWT) performs better than fast Fourier transform (FFT) for the analysis and the detection of embolic signals (ES) [25, 26 ,27]. The existence of fast algorithms to implement DWT, makes also the investigation of the feasibility of ES detection systems based on DWT worthwhile. Therefore, we suggest in this chapter to exploit wavelet-based techniques to detect and to classify the embolic signals. However, the selection of an appropriate mother wavelet for the signal being analyzed is an important criterion [101].

Consequently, in the first part on this chapter we describe a strategy to choose a suitable mother wavelet for detection and classification of microemboli exploiting experimental backscattered RF signals. Several wavelet functions namely, Biorthogonal, Coiflet, Daubechies, and Symlets are evaluated within a microemboli classification system based on discrete wavelet transform (DWT) and support vector machines (SVM) as a classifier. The effectiveness of the choice of the suitable mother wavelet in the evaluation of the proposed system is assessed.

Then, in the second part of this chapter, we employ DWT algorithm based on the selected wavelet function to decompose RF signals into different frequency bands and identify which features lead to a better recognition performance. Several features are evaluated from the detail coefficients. It should be noted that the features used in this study are the same used in the work by N. Aydin et al. [25]. These features are used as inputs to the classification models without using feature selection method. Thereafter, and due to curse of dimensionality, we employ three different dimensionality reduction technique based on Differential Evolution algorithm (DEFS), Fisher Score method, and Principal Component Analysis (PCA). This last step is vital since dimensionality reduction algorithms improve classification accuracy by selecting features that are most relevant to the classification task.

Part.1: Selection of mother wavelet

The general block diagram of the detection algorithm is shown in Figure V.1. The input backscatter RF signals are first detected and collected (signal acquisition). At the second stage, DWT coefficients of the signals are obtained using several wavelet functions. This process decomposes the input signal into an optimum number of frequency bands. Therefore, it is important to determine a suitable wavelet for the signal being analyzed. We evaluate several wavelet functions namely; Biorthogonal, Coiflet, Daubechies, and Symlets within a microemboli classification system based on discrete wavelet transform (DWT) and support vector machines (SVM) as a classifier. In the third step, after applying the DWT on the backscatter RF signals, several features are evaluated from detail and approximation coefficients. In the last step, these features are used as input parameters to the SVM classification model.

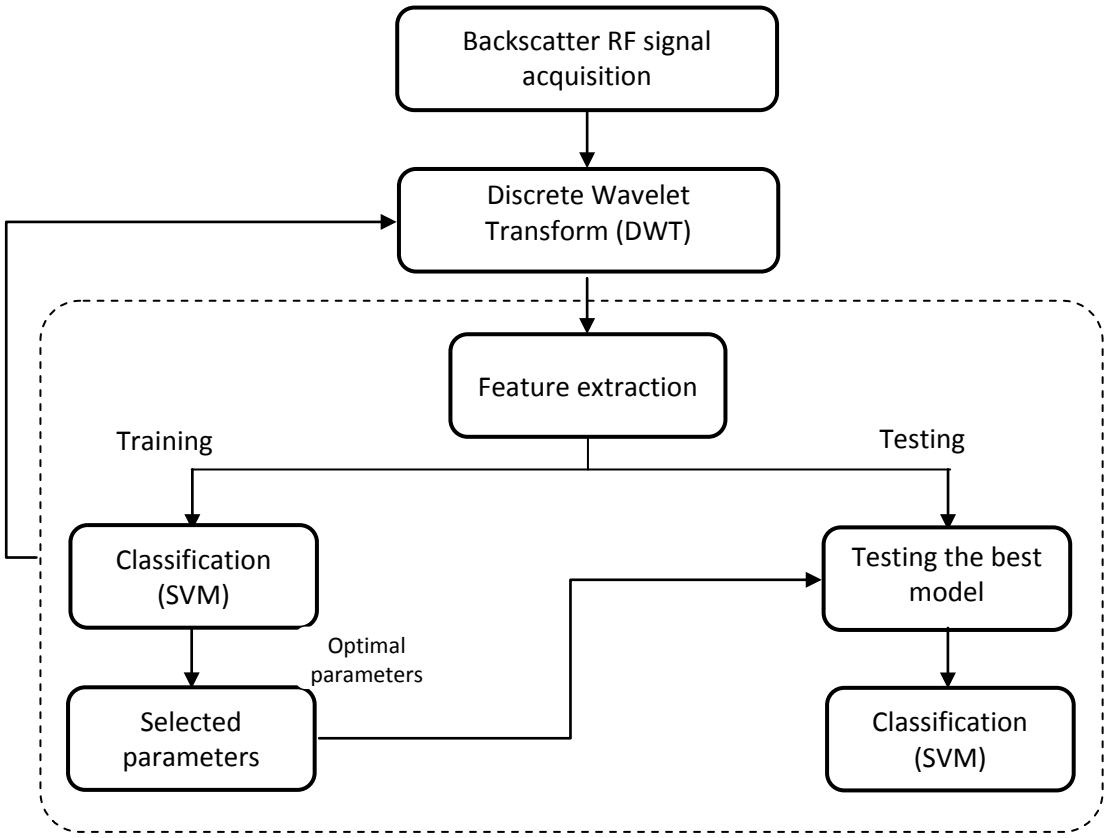

Figure V. 1. Flowchart of the proposed approach.

V.2.1 Wavelet Transform

The wavelet transform is a linear process that decomposes a signal into components that appear at different scales [25, 102]. The basic idea of the wavelet transform is to represent any arbitrary signal *x(t)* as a superposition of a set of wavelets or basis functions. These basis functions (wavelets) are obtained from a single prototype wavelet called the mother wavelet by dilation (scaling) and translation (shifts). The wavelet transform of a continuous signal *x(t)* is defined as [25, 102]:

$$c(a,b) = \int_R x(t) \frac{1}{\sqrt{a}} \psi \frac{(t-b)}{(a)} dt, \qquad \text{(V.1)}$$

where, the indexes *c(a,b)* are called wavelet coefficients of signal *x(t)*, *a* is the dilation and *b* is the translation, *Ψ(t)* is the transforming function (the mother wavelet). Low frequencies are explored with low temporal resolution while high frequencies with more temporal resolution. The discrete wavelet transform (DWT) of a signal is depicted with respect to a mother wavelet and maps continuous finite energy signals to a two-dimensional grid of coefficients [25, 102]. The scale *a* in the discrete wavelet transform case becomes $a = a_0^m$, and the translation *b* becomes $b = nb_0a_0^m$ [25, 102]. The DWT of a discrete signal with length *N* is defined as:

$$c(m,n) = \frac{1}{\sqrt{a_0^m}} \sum_{k=0}^{N-1} s(k) \psi \left(\frac{k - nb_0a_0^m}{a_0^m} \right). \qquad \text{(V.2)}$$

DWT of a discrete signal yields a set of coefficients including all the detailed coefficients and the last approximation coefficients [25, 102].

V.2.2 Feature Extraction

Using DWT, the normalized backscattered RF signal can be transformed into different time–frequency scales through the wavelet analysis. It employs two functions as high-pass filters and low pass filters. The high-frequency filter generates a detailed version of the backscatter RF signal (*D*), while the low-frequency filter produces its approximate version (*A*).

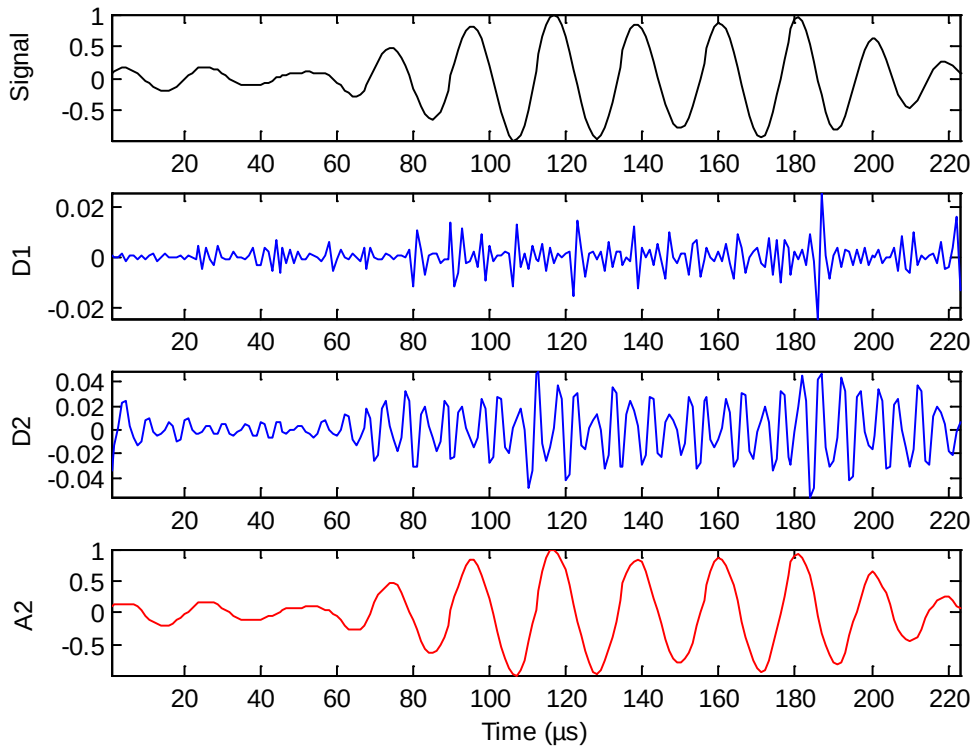

a) Gaseous embolus

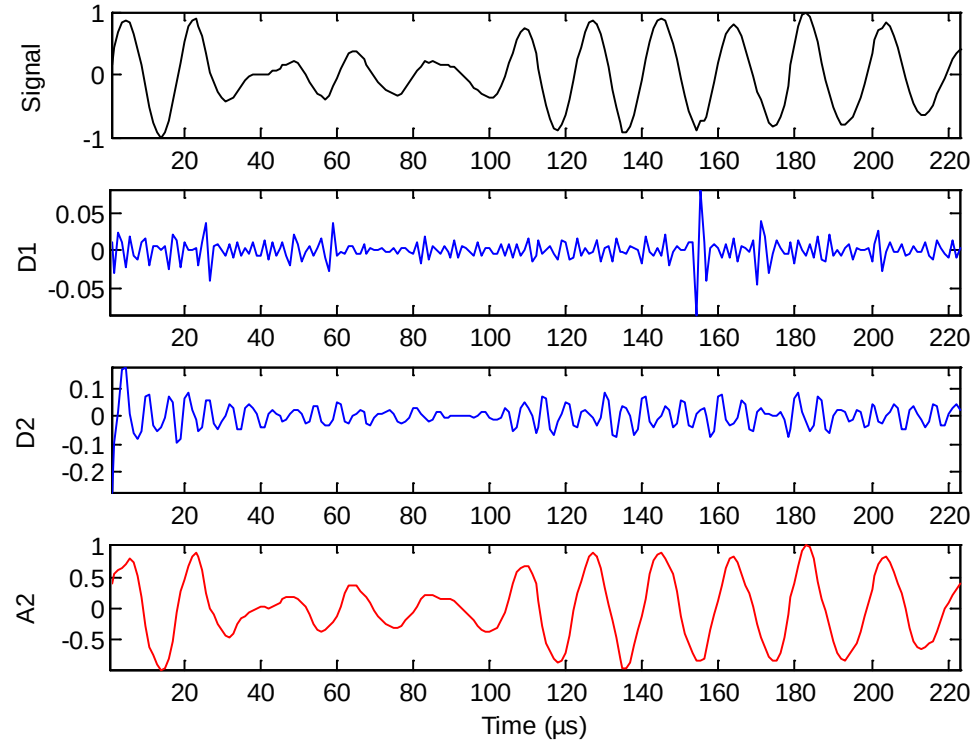

b) Solid embolus

Figure V. 2. Examples of DWT using Daubechies (db4) as mother wavelet of backscatter RF signal at low mechanical index (MI = 0.2).

In our study, we decompose the backscatter RF signal *x(t)* into two levels. Wavelet functions used for this study are standard DWT functions available in Matlab Wavelet toolbox [103] namely Daubechies (1 to 32), Coiflet (1 to 5), Symlet (2 to 8), and Biorthogonal (1.1, 1.3, 1.5, 2.2, 2.4, 2.6, 2.8, 3.1, 3.3, 3.5, 3.7, 3.9, 4.4, 5.5, 6,8). These functions are integrated into the automatic classification system.

An example of the decomposition of gaseous embolus and solid embolus signals using Daubechies (db4) as mother wavelet is shown in Figure V.2. The detail and approximation coefficients are not directly used as inputs for the classifier. Several features are evaluated from the detail and approximation coefficients. It should be noted that for each of the DWT coefficients, four features (standard deviation, root mean square, energy and Shannon-entropy) are calculated using the equations given in Table V.1 [104]. All features are individually applied on the detail and approximation coefficients of each decomposition level.

Table V. 1. Features and their corresponding formulas applied on the detail and approximation coefficients of each decomposition level.

Features	**Formulas**
Standard deviation:	$\sigma^2 = \frac{1}{N}\sum_{j=1}^{N}\left(x_{ij} - \mu\right)$ μ: mean of x
Root mean square:	$RMS = \sqrt{\frac{1}{N}\sum_{j=1}^{N} x_{ij}^{\,2}}$
Energy:	$E = \sum_{j=1}^{N} \left\| x_{ij} \right\|^2$
Shannon-entropy:	$H = \sum_{j=1}^{N} x_{ij}^{\,2} \log\left(x_{ij} \right)^2$

Standard deviation: The standard deviation is a measure of how far a sample in the signal fluctuates from the mean value. A low standard deviation indicates that the samples tend to be very close to the mean value, high standard deviation indicates that the samples are spread out over a large range of values.

Root mean square amplitude: The root mean square (RMS) of a signal is defined as the averaged amplitude of signal: it is used to quantify the overall energy content of the signal.

Energy: The energy of the signals is computed as a feature in this study. Since often gaseous embolus occurrence increases the energy of the signal, it is typical to use energy for microemboli detection.

Shannon entropy: The Shannon entropy is calculated as a measure of energy randomness in each wavelet decomposition level.

As a result, we obtain 12 features for each backscattered RF signal (solid or gaseous embolus). These features are used as inputs to the SVM classifier, which provides in its output a value of 1 or -1 for gaseous or solid emboli, respectively.

V.2.3 Classification (Support Vector Machines)

The classification process consists of two steps: (i) assign the system certain signals as training samples, and (ii) classify the signals according to their features via a trained classifier model. Several types of classifiers have been deployed in the microemboli classification community [18-25]. In this section, we choose SVM classifier (illustrated in chapter II section II.2-4) due to its high generalization performance. Other competitive classifiers could have also been chosen.

After Applying DWT on the backscatter RF signals we obtain 12 features for each mother wavelet filter. In order to get a deep insight into our dataset, we employ Principal Component Analysis (PCA) method depicted in chapter II section II.3-2.1. PCA maps the original feature space to a lower-dimensional space so as to conserve the maximum amount of information from the initial dimensions. It can supply us with a lower-dimensional visualization, it is a projection of the dataset when viewed from its most informative viewpoint. This is done by using only the first few principal components so that the dimensionality of the transformed data is reduced.

It should be noted that PCA is used in this section only for the visualization of our dataset. Figure V.3 shows the distribution of the 1st three feature components using Principal Component Analysis (PCA) extracted using Daubechies db4 mother wavelet. The projection of the features constructed from the dataset in a 3-dimensional chart illustrates that these features are nonlinearly separable.

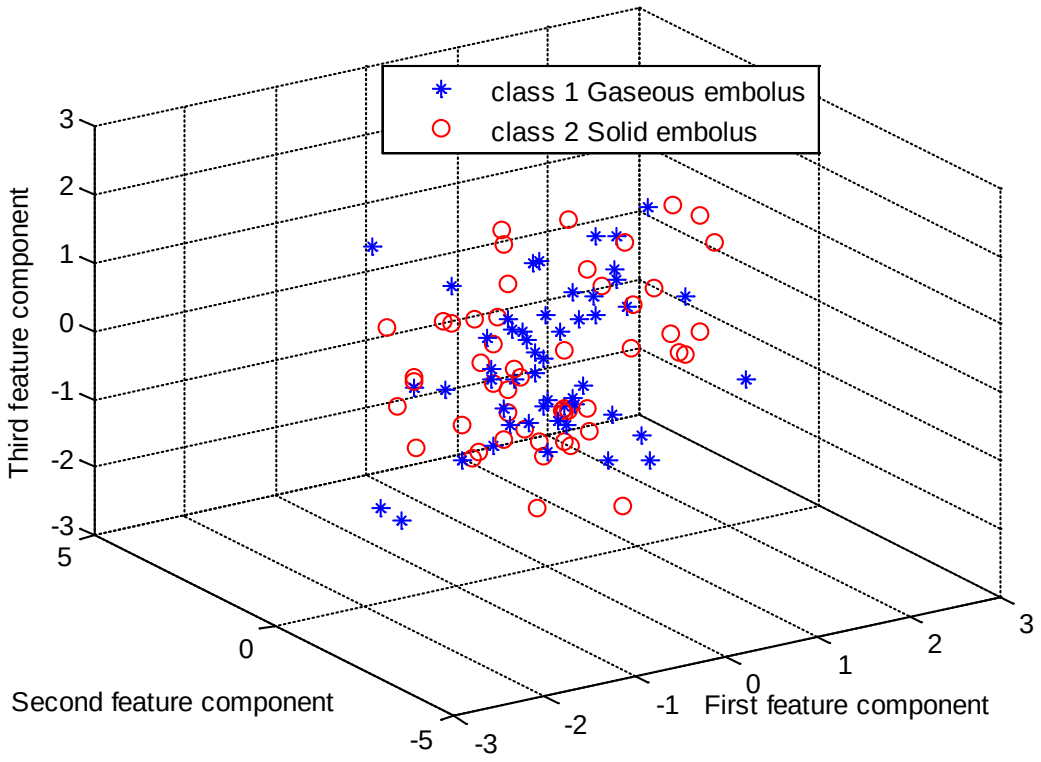

Figure V. 3. Distribution of the 1st three feature components for the concentration of microbubbles (0.025µl/ml) at Low MI (0.2) with Daubechies **db4** mother wavelet using PCA.

In order to evaluate the performance of the proposed system, and since the feature vector extracted from RF signals is nonlinearly separable (refer to Figure V.3), we prefer a nonlinear support vector machines classifier to solve this classification problem.

V.2.4 Results and Discussions

Classification performances are evaluated in term of overall accuracy, which is the percentage of correctly classified emboli among all the emboli independently of the classes they belong to. For each dataset, we ran a nonlinear SVM classifier based on the Gaussian RBF (SVM-RBF) [22]. Classification results for four datasets with each of the wavelet functions used in the classification algorithm are summarized in Table V.2, Table V.3, Table V.4, and Table V.5. The best results appear in bold.

Table V. 2. Detection with Biorthogonal wavelet functions [22].

Wavelet type	Classification rate (%)			
	C=0.025µl/ml		C=0.05µl/ml	
	Low MI (0.2)	High MI (0.6)	Low MI (0.2)	High MI (0.6)
Bior1.1	79,17	75,00	70,83	79,17
Bior1.3	79,17	79,17	79,17	79,17
Bior1.5	75,00	83,33	83,33	79,17
Bior2.2	83,33	87,50	83,33	79,17
Bior2.4	87,50	83,33	83,33	83,33
Bior2.6	83,33	87,50	83,33	83,33
Bior2.8	83,33	79,17	83,33	91,67
Bior3.1	**87,50**	**91,67**	**91,67**	**95,83**
Bior3.3	83,33	87,50	87,50	87,50
Bior3.5	83,33	91,67	87,50	95,83
Bior3.7	83,33	83,33	87,50	91,67
Bior3.9	83,33	91,67	87,50	95,83
Bior4.4	83,33	83,33	87,50	91,67
Bior5.5	79,17	87,50	87,50	91,67
Bior6.8	83,33	87,50	87,50	91,67

Table V. 3. Detection with Coiflet wavelet functions [22].

Wavelet type	Classification rate (%)			
	C=0.025µl/ml		C=0.05µl/ml	
	Low MI (0.2)	High MI (0.6)	Low MI (0.2)	High MI (0.6)
Coif1	83.33	83.33	83.33	83.33
Coif2	87.50	87.50	83.33	83.33
Coif3	**87.50**	**91.67**	**87.50**	**91.67**
Coif4	87.50	75.00	87.50	87.50
Coif5	83.33	75.00	87.50	87.50

Table V. 4. Detection with Symlet wavelet functions [22].

Wavelet type	Classification rate (%)			
	C=0.025µl/ml		C=0.05µl/ml	
	Low MI (0.2)	High MI (0.6)	Low MI (0.2)	High MI (0.6)
Sym2	75.00	75.00	87.50	83.33
Sym3	75.00	79.17	87.50	87.50
Sym4	79.17	87.50	83.33	83.33
Sym5	79.17	87.50	79.17	79.17
Sym6	87.50	87.50	87.50	83.33
Sym7	**87.50**	**91.67**	**91.67**	**87.50**
Sym8	83.33	83.33	83.33	83.33

Table V. 5. Detection with Daubechies wavelet functions [22].

Wavelet type	Classification rate (%)			
	C=0.025µl/ml		C=0.05µl/ml	
	Low MI (0.2)	High MI (0.6)	Low MI (0.2)	High MI (0.6)
db 1	79.17	79.17	83.33	75.00
db 2	62.50	83.33	91.67	83.33
db 3	75.00	79.17	91.67	79.17
db 4	83.33	83.33	79.17	87.50
db 5	87.50	91.67	79.17	91.67
db 6	**91.67**	**91.67**	**91.67**	**95.83**
db 7	79.17	83.33	83.33	87.50
db 8	83.33	79.17	79.17	91.67
db 9	70.83	83.33	83.33	91.67
db 10	70.83	70.83	87.50	91.67
db 11	83.33	79.17	75.00	87.50
db 12	70.83	70.83	83.33	91.67
db 13	75.00	91.67	83.33	91.67
db 14	79.17	75.00	83.33	87.50
db 15	75.00	70.83	83.33	95.83
db 16	75.00	70.83	83.33	91.67
db 17	62.50	75.00	79.17	87.50
db 18	75.00	70.83	83.33	87.50
db 19	75.00	75.00	70.83	91.67
db 20	75.00	75.00	79.17	83.33
db 21	75.00	79.17	83.33	83.33
db 22	70.83	75.00	83.33	87.50
db 23	75.00	75.00	83.33	83.33
db 24	75.00	75.00	75.00	87.50
db 25	70.83	75.00	79.17	91.67
db 26	75.00	75.00	83.33	83.33
db 27	75.00	79.17	79.17	83.33
db 28	70.83	75.00	79.17	87.50
db 29	70.83	75.00	83.33	87.50
db 30	75.00	79.17	83.33	87.50
db 31	70.83	75.00	79.17	87.50
db 32	70.83	75.00	70.83	83.33

Since no other parameters than the wavelet filter type changed, the results give an indication on the suitability of the wavelet function for the particular acquisition. In Table V.2, detection results are given for different Biorthogonal types of the wavelet function. The Biorthogonal 3.1 achieved the best detection. For the Coiflet type wavelet, Coiflet3 achieved the best results (Table V.3). For the Symlet type wavelet, the best results are obtained using Symlet 7 (Table V.4). For the Daubechies type wavelet, the best results are reached by Daubechies 6 (Table V.5).

Classification results for the wavelet functions given in the Table V.2, Table V.3, Table V.4, and Table V.5 indicate that there is no analytical justification for the choice of a particular wavelet function for a particular signal, so the required wavelet filter should be determined experimentally. The performance of the classification system greatly depends on the selection of the mother wavelet.

The best results for the wavelet functions given in the Table V.2, Table V.3, Table V.4, and Table V.5 are grouped in Table V.6.

Table V. 6. Best classification rates and corresponding mother wavelet functions [22].

Wavelet type	Classification rate (%)			
	C=0.025µl/ml		C=0.05µl/ml	
	Low MI (0.2)	High MI (0.6)	Low MI (0.2)	High MI (0.6)
Bior3.1	87.50	91.67	91.67	95.83
Coif3	87.50	91.67	87.50	91.67
db 6	**91.67**	**91.67**	**91.67**	**95.83**
Sym7	87.50	91.67	91.67	87.50

From Table V.6, the wavelet corresponding to the highest classification rate is selected as the most suitable mother wavelet. Therefore, conclusively we can say that among 59 mother wavelet functions db6 appears to be the most appropriate wavelet function for this medical application.

Part.2: Detection using Dimensionality Reduction algorithms

The general block diagram of the detection system is shown in Figure V.4. The input backscatter RF signals are first detected and collected (signal acquisition). At the second stage, DWT coefficients of the signals are collected. Input signal are decomposed into an optimum number of frequency bands using DWT. Therefore, it is vital to select an appropriate wavelet for the signal being analyzed. Suitability of the wavelet filters and orders are determined experimentally. As shown in section V.2 the best mother wavelet on the same types of backscatter RF signals is Daubechies (db6) [22]. In the third step, after applying DTW on the backscatter RF signals, several features are evaluated from the detail coefficients. It should be noted that the features used in this study are the same in the paper by N. Aydin et al. [25]. Table V.7 shows the ten (10) features for each decomposition level and their formulas. In the last step, all these features are first used as inputs to the classification model without feature selection method. Second, due to the curse of dimensionality, we employ three dimensionality reduction techniques dimensionality reduction techniques; Differential Evolution algorithm (DEFS), Fisher Score method, and Principal Component Analysis (PCA) [64, 83, 86, 87]. The motivation for this approach is that the more powerful among the existing machine learning algorithms tend to get confused when supplied with a large number of features [105].

Before classification and dimensionality reduction tasks, and since the generalization performance of an algorithm should be estimated using unseen samples, we randomly divide the dataset into two subsets (training set and test set). After that, we apply cross-validation technique only on the training set to tune the classifier parameters and to select the features. Thus the algorithms have only access to the training set, and the test set is kept unseen both to the ranking step and to the classifying step. The experimental evaluation is performed using hold-out-set cross-validation to avoid overfitting and assure statistical validity of the results [57].

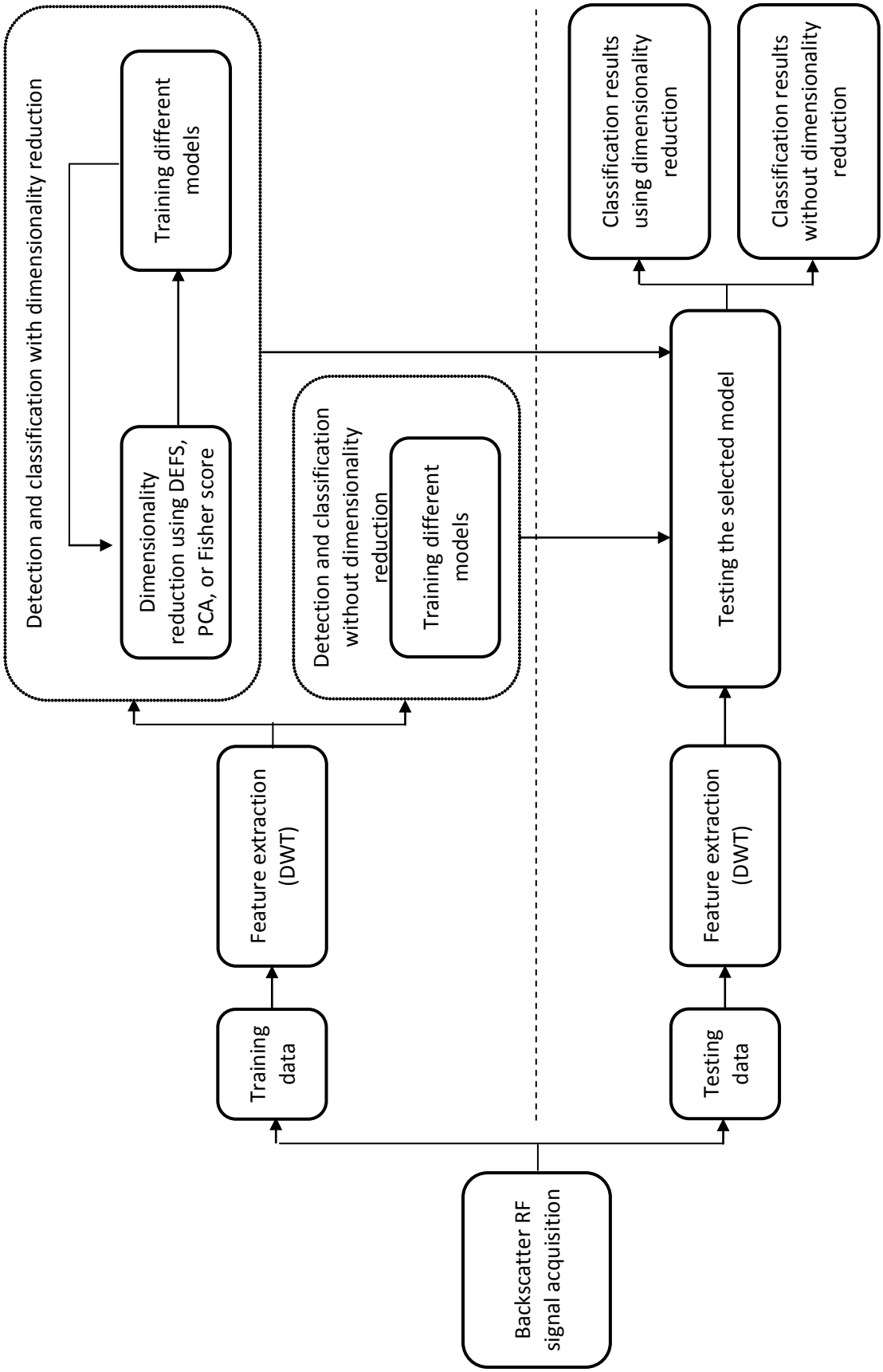

Figure V. 4. Block diagram of the DWT-based detection system.

To summarize, our experiment setting is based on the cross-validation technique. A complete algorithm is constructed by cascading dimensionality reduction and classification. The dimensionality reduction step is achieved by DEFS algorithm, PCA technique, or Fisher score method.The classification step is SVM algorithm. The training data is used to select the most relevant features and to fix the classifier parameters. The final results presented are based on the system's performance using one unseen test session.

V.3-1 Feature extraction

The goal of feature extraction is to determine those components of the signal that are deemed most relevant to the application at hand. An example of the decomposition of gaseous embolus and solid embolus signals using the selected wavelet function Daubechies (db6) is shown in Figure V.5. The detail and approximation coefficients are not directly used as inputs for the classification model. Several features are evaluated from the detail and approximation coefficients.

The instantaneous power (IP) is calculated for the DWT coefficients of each level. A threshold value for each level is determined. Figure V.6 illustrates the associated IP and threshold values, which are used in the detection algorithm.

The threshold is calculated from the data using a statistical method, which depends on the data length and the standard deviation [106], and it is given by:

$$A_{th} = \sigma_n \sqrt{\log_2 N}, \qquad \text{(V.3)}$$

where:

σ_n : is the standard deviation of the signal power at the n^{th} level

N : is the length of the observation.

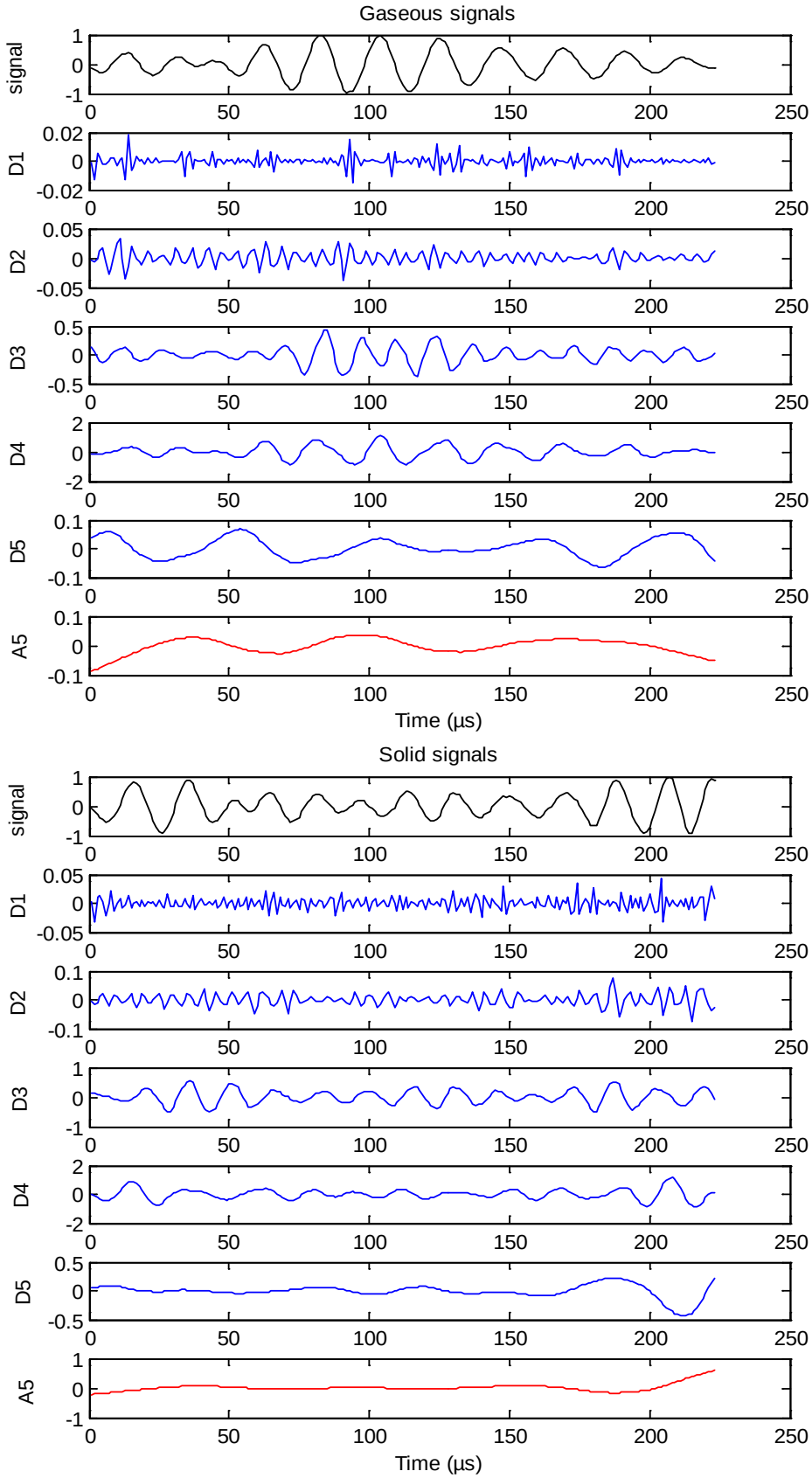

Figure V. 5. Examples DWT of backscatter RF signal using Daubechies (db6) as mother wavelet for C=0.025µl/ml at low MI.

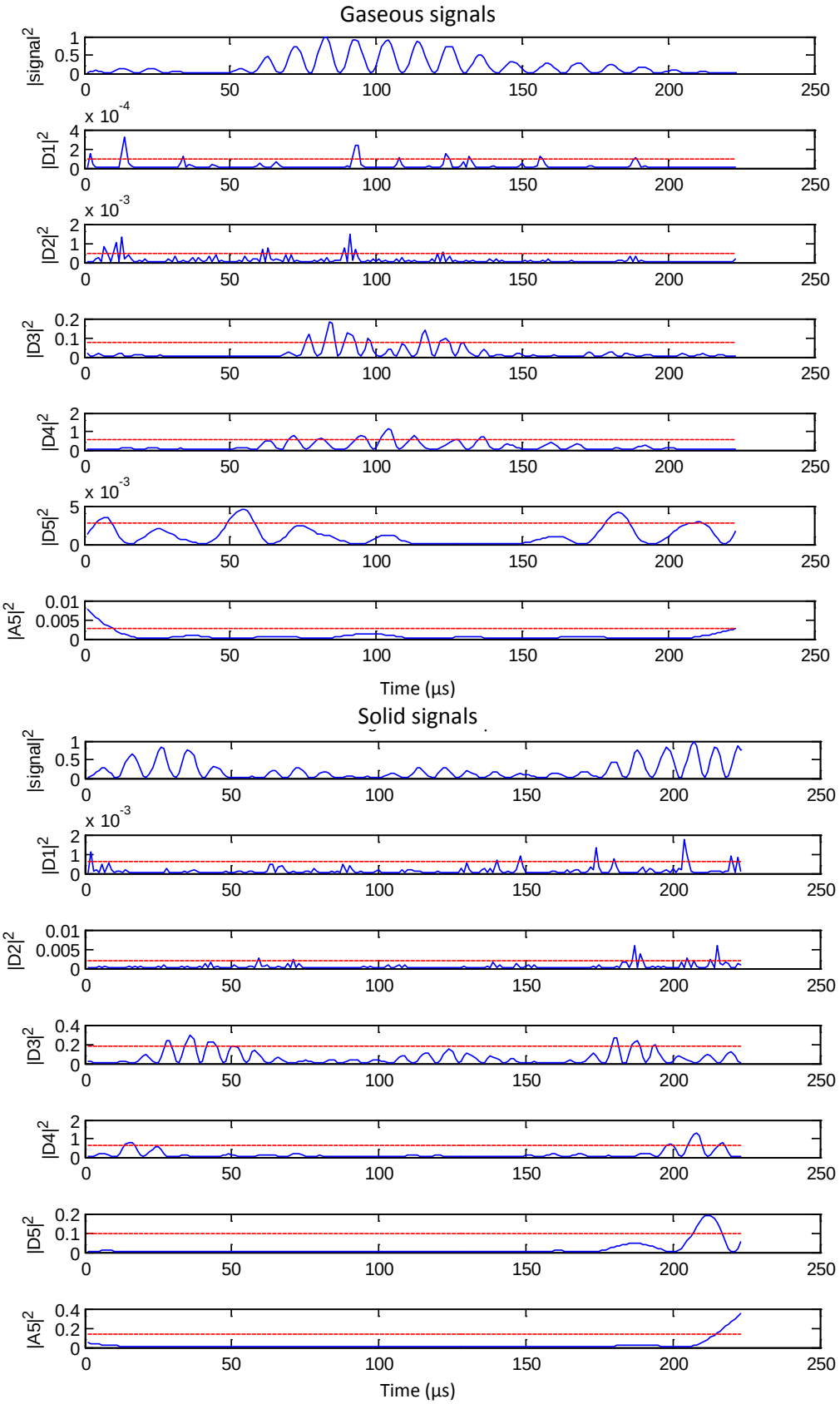

Figure V. 6. Instantaneous power and corresponding threshold values for each level (gaseous and solid embolus signals).

The following parameters relating the threshold are determined:

The ratio of the embolic signal to the background signal (EBR) is the most widely used feature in microemboli detection [25]. EBR shows how strong an embolic signal is relative to the background. *P2TR* is one of the definitions of the EBR, *P2TR* can be calculated using the measures given in Figure V.7.

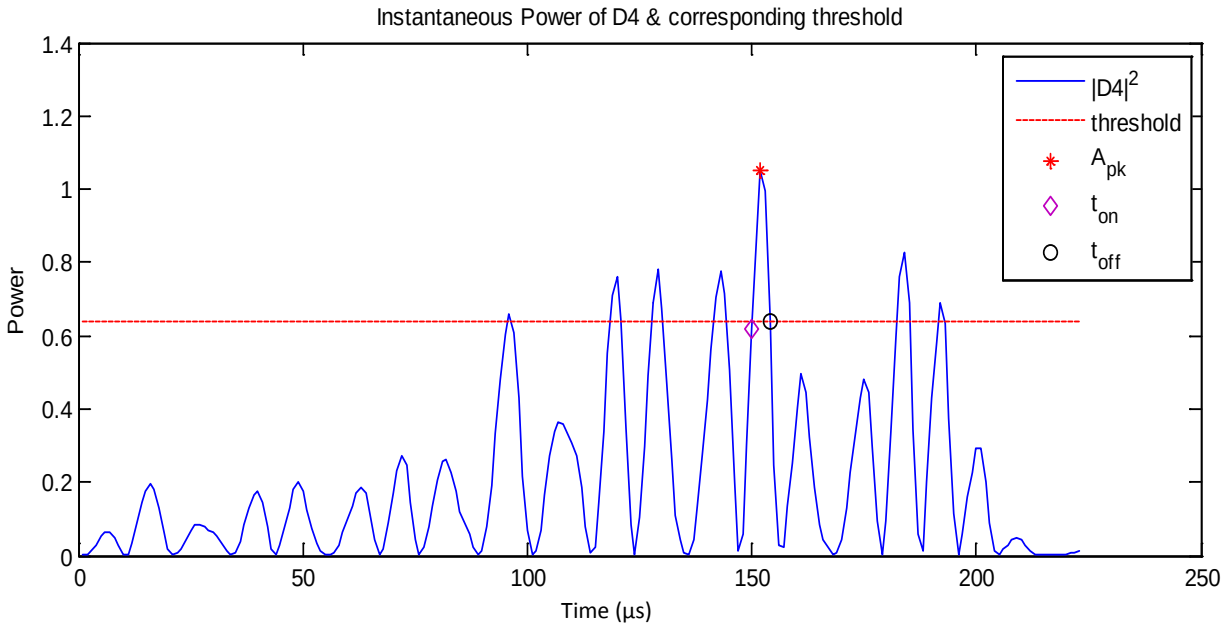

Figure V. 7. Instantaneous power of the detail coefficient and parameters used to calculate detection features.

$$\mathrm{P2TR} = 10\log\frac{\mathrm{A_{pk}}}{\mathrm{A_{th}}}\ (\mathrm{dB}) \qquad \text{(V.4)}$$

Another feature, the total power to the threshold ratio (TP2TR) which is the quantity of power a signal has relative to the background energy, and it is given by:

$$\mathrm{TP2TR} = 10\log\frac{\mathrm{A_{tot}}}{\mathrm{A_{th}}} = 10\log\frac{\sum_{k=t_{on}}^{t_{off}}\mathrm{A}_f(k)}{\mathrm{A_{th}}}\ (\mathrm{dB}) \qquad \text{(V.5)}$$

where A_{tot} is the total power of the signal *A(k)*. It is calculated by integrating the *IP* of signal between t_{on} and t_{off} , as illustrated in Figure V.7.

Two other features, which use threshold indirectly, are rise rate (RR) and fall rate (FR):

$$\mathrm{RR} = \frac{10\ \log\frac{\mathrm{A}_{pk}}{\mathrm{A}_{\mathrm{th}}}}{\mathrm{t}_{\mathrm{pk}} - t_{on}} = \frac{\mathrm{P2TR}}{\mathrm{t}_{\mathrm{pk}} - t_{on}} \quad (\mathrm{dB/ms}) \tag{V.6}$$

$$\mathrm{FR} = \frac{10\ \log\frac{\mathrm{A}_{pk}}{\mathrm{A}_{\mathrm{th}}}}{\mathrm{t}_{\mathrm{off}} - t_{pk}} = \frac{\mathrm{P2TR}}{\mathrm{t}_{\mathrm{off}} - t_{pk}} \quad (\mathrm{dB/ms}) \tag{V.7}$$

where: t_s is the average time of the signal and f_s is the average frequency of the signal.

t_s and f_s are calculated, respectively, as

$$t_s = \frac{1}{E_s}\int_{-\infty}^{+\infty} t\,|\,s(t)\,|^2\,dt\text{, and} \tag{V.8}$$

$$f_s = \frac{1}{E_s}\int_{-\infty}^{+\infty} f\,|\,S(f)\,|^2\,df \tag{V.9}$$

where *S(f)* is the Fourier transform of the signal *s(t).*

Time spreading Ts^2 and frequency spreading Bs^2 are defined as:

$$T_s^2 = \frac{1}{E_s}\int_{-\infty}^{+\infty}(t-t_s)^2\,|\,s(t)\,|^2\,dt\text{, and} \tag{V.10}$$

$$B_s^2 = \frac{1}{E_s}\int_{-\infty}^{+\infty}(f-f_s)^2\,|\,S(f)\,|^2\,df \tag{V.11}$$

where:

$$E_s = \int_{-\infty}^{+\infty}|s(t)|^2 dt \tag{V.12}$$

The instantaneous envelope and instantaneous frequency of a signal [107] are used to describe a signal simultaneously in time and in frequency. These two parameters are defined, respectively, as:

$$a(t) = |s_a(t)| \quad \text{(V.13)}$$

$$f(t) = \frac{1}{2\pi}\frac{darg\ s_a(t)}{dt} \quad \text{(V.14)}$$

where $s_a(t)$ is the Hilbert transform of *s(t).*

$$s_a(t) = s(t) + j\hat{s}(t).\hat{s}(t) \quad \text{(V.15)}$$

The variances of instantaneous envelope and instantaneous frequency (*VIE* and *VIF*) are used as other types of features.

Processing steps for the classification of microemboli can be summarized as follows:

- Apply DWT to for both solid and gaseous signals in order to collect DWT coefficients;
- Calculate Instantaneous power for each level;
- From each level, derive a threshold value to be employed in detection;
- Evaluate previously described parameters for each DWT level;
- Apply: (i) classification, (ii) dimensionality reduction.

Table V.7 summarizes the feature extractor methods that are used in this study It should be noted that the features illustrated in this table are the same used in the work by N. Aydin et al. in which he employed a fuzzy classification system for the characterization of Doppler signals [25].

Table V. 7. The features used in this section and their formulas [25].

	Feature number (n)	Formulations of detail coefficients
$P2TR_n$	n =1,...,5	$P2TR = 10\log\frac{A_{pk}}{A_{th}}$ (dB)
$TP2TR_n$	n =6,...,10	$TP2TR = 10\log\frac{A_{tot}}{A_{th}} = 10\log\frac{\sum_{k=t_{on}}^{t_{off}} A_f(k)}{A_{th}}$ (dB)
RR_n	n=11,...,15	$RR = \frac{10\ \log\frac{A_{pk}}{A_{th}}}{t_{pk} - t_{on}} = \frac{P2TR}{t_{pk} - t_{on}}$ (dB / ms)
FR_n	n=16,...,20	$FR = \frac{10\ \log\frac{A_{pk}}{A_{th}}}{t_{off} - t_{pk}} = \frac{P2TR}{t_{off} - t_{pk}}$ (dB / ms)
t_{sn}	n=21,...,25	$t_s = \frac{1}{E_s}\int_{-\infty}^{+\infty} t\,\lvert s(t)\rvert^2 dt$
f_{sn}	n=26,...,30	$f_s = \frac{1}{E_s}\int_{-\infty}^{+\infty} f\,\lvert S(f)\rvert^2 df$
$T_{s\,n}^2$	n=31,...,35	$T_s^2 = \frac{1}{E_s}\int_{-\infty}^{+\infty}(t-t_s)^2\,\lvert s(t)\rvert^2 dt$
$B_{s\,n}^2$	n=36,...,40	$B_s^2 = \frac{1}{E_s}\int_{-\infty}^{+\infty}(f-f_s)^2\,\lvert S(f)\rvert^2 df$
VIE_n	n=41,...,45	*var(a(t))* with $a(t) = \lvert s_a(t)\rvert$ where $s_a(t) = s(t) + j\hat{s}(t)$. $\hat{s}(t)$ is the Hilbert transform of $s(t)$
VIF_n	n=46,...,50	*var(f(t))* with $f(t) = \frac{1}{2\pi}\frac{d\ \arg s_a(t)}{dt}$

It should be noted here that *n* is the number of the detail coefficient which is used to calculate the classification parameters. In our case *n* is equal to 5 for each decomposition level.

As shown in Figure V.7, and unlike all the detail coefficients, the approximation coefficients does not have a similar shape (peak or Gaussian) thus we can't extract the parameters t_{on} and t_{off}, therefore we discarded the approximation coefficients from the feature extraction phase.

V.3-2 Classification without dimensionality reduction

For binary classification problems with limited number of samples it is crucial to validate the classification model with cross-validation technique. Before building the classification model, the samples are subdivided into three subsets training set, validation set, and test set. The test set is used only for the assessment of the model selected by the cross-validation technique, while the validation set is used to tune the classifiers parameter. Therefore the algorithm has only access to the training and validation sets, the test set is kept unseen in the selection process of the best model.

Classification performance is evaluated in terms of seven evaluation measures (illustrated in chapter II section II.4), which are: Recall (Sensitivity), Specificity, Precision, Kappa, F-measure, overall accuracy, and AUC (Area Under Curve). We have invoked the same SVM classifier (defined in chapter II section II.2.4). Furthermore, we have iteratively tested different SVM parameter settings by trying exponentially growing sequences of C and γ [75] ($C = 2^{-3}, 2^{-2}, ..., 2^{9}, 2^{10}$, $\gamma = 2^{-3}, 2^{-2}, .., 2^{4}, 2^{5}$). For each pair of ($C$, γ) we train the SVM with the training data, and then we use the SVM to classify the validation data. The combination that results in a model with highest validation accuracy is picked as the best choice of the classification problem. The testing accuracy is obtained by applying the selected SVM model on the testing data.

Table V.8 summarizes the percentage of the seven evaluation measures defined in chapter II section II.4 (Accuracy (ACC), Sensitivity or Recall (r), Specificity (Spe), precision (P), F-measure (F), Kappa coefficient (Kappa), and area under curve (AUC)) using SVM analysis as a function of all input features (50 features) and mechanical indexes for the two microbubble concentrations (0.025 µl/ml and 0.05µl/ml).

Table V. 8. Evaluation measures of gaseous and solid emboli using all features [18].

	C = 0.025µl/ml		*C = 0.05 µl/ml*	
	Low MI (0.2)	High MI (0.6)	Low MI (0.2)	High MI (0.6)
Sensitivity or Recall (*r*) (Gaseous emboli)	92.85	78.57	85.74	92.85
Specificity (*Spe*) (Solid emboli)	78.57	85.71	85.71	78.57
Precision (*P*)	81.25	84.61	85.71	81.25
Kappa	71.42	64.28	71.42	71.42
F-measure (*F*)	86.66	81.48	85.71	86.66
Accuracy (ACC)	85.71	82.14	85.71	85.71
AUC (Area Under Curve)	92.85	86.73	91.83	91.83
OT: Optimal Threshold	-0.279	-0.093	0.758	-0.098

Figure V.8 shows the ROC curves of the four datasets using several detection thresholds in which TP rate is plotted on the Y axis and FP rate is plotted on the X axis. The best results that maximizes (sensitivity and specificity) are achieved using the thresholds of -0,279, -0.093, 0.758, and -0,098 for the acquisitions 1, 2, 3, and 4 respectively. The ROC curves in Figure V.8 indicate that the proposed model is deteriorated by irrelevant features.

Figure V.8 illustrates that for the concentration C = 0.025µl/ml at low MI and the concentration C = 0.05µl/ml at high MI with optimal thresholds of -0,279 and -0,098 respectively, the proposed classification model classifier recognizes better gaseous emboli than at solid emboli with a sensitivity of 92.85% and a specificity of 78,57%. However, for the concentration C=0.025µl/ml at high MI (0.6), the classifier performs better at identifying solid emboli than at identifying gaseous emboli with a sensitivity of 78,57% and a specificity of 85,71%. For the concentration C = 0.05µl/ml at low MI and the classification performances for gaseous and solid emboli are quite similar.

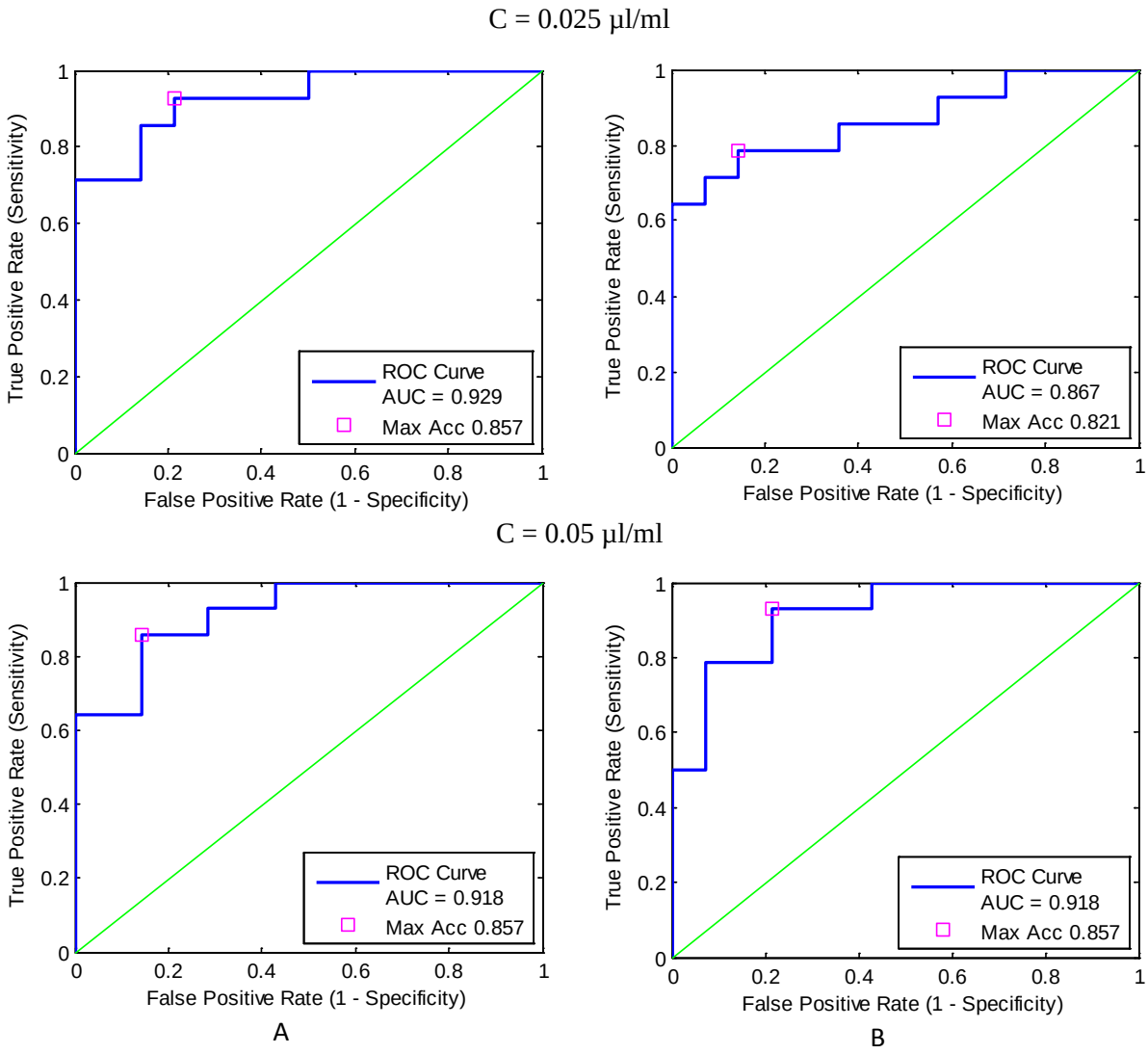

Figure V. 8. ROC curve at different detection thresholds using all features, : A). MI= 0.2, B). MI= 0.6 for two microbubbles concentrations [18]

Average classification rate, F-measure, and Kappa coefficient did not exceed 85.71%, 86.66%, 71.42% respectively for all datasets using all features as input vector. Therefore, the feature vector is too large to be handled properly by the classifier. To overcome this limitation, we group the input parameters into small feature vectors regarding the nature of each feature then we apply the classification algorithm on each set of features separately, the results are shown in Table V.9 and Table V.10.

Table V. 9. Evaluation measures using each set of features separately Acqu 1 and 2 [18].

C = 0.025µl/ml								
Features	Low MI (0.2)							
	r	*Spe*	*P*	Kappa	*F*	ACC	AUC	OT
$P2TR_n$	71.42	71.42	71.42	42.85	71.42	71.42	65.30	-0.972
$TP2TR_n$	92.85	78.57	81.25	71.42	86.66	85.71	90.81	-0.001
RR_n	100	50	66.66	50	80	75	80.61	-0.817
FR_n	85.71	78.57	80	64.28	82.75	82.14	85.20	-0.167
t_{sn}	78.57	100	100	**78.57**	**88**	**89.28**	**94.38**	0.336
f_{sn}	100	78.57	82.35	**78.57**	**90.32**	**89.28**	**93.87**	-0.737
T^2_{sn}	85.71	85.71	85.71	71.42	85.71	85.71	88.26	-0.007
B^2_{sn}	78.57	92.85	91.66	71.42	84.61	85.71	86.22	-0.231
VIE_n	92.85	85.71	86.66	**78.57**	**89.65**	**89.28**	**92.34**	0.002
VIF_n	100	28.57	58.33	28.57	73.68	64.28	52.55	-0.888
Features	High MI (0.6)							
	r	*Spe*	*P*	Kappa	*F*	ACC	AUC	OT
$P2TR_n$	71.42	50	58.82	21.42	64.51	60.71	60.20	-0.215
$TP2TR_n$	92.85	78.57	81.25	71.42	86.66	85.71	86.22	0.072
RR_n	71.42	71.42	71.42	42.85	71.42	71.42	74.49	-0.210
FR_n	92.85	57.14	68.42	50	78.78	75.00	79.59	-0.186
t_{sn}	85.71	92.85	92.30	78.57	88.88	89.28	93.87	-0.165
f_{sn}	92.85	85.71	86.66	**78.57**	**89.65**	**89.28**	**94.38**	-0.246
T^2_{sn}	71.42	100	100	71.42	83.33	85.71	88.26	0.433
B^2_{sn}	100	71.42	77.77	71.42	87.50	85.71	92.34	-0.222
VIE_n	92.85	92.85	92.85	**85.71**	**92.85**	**92.85**	**95.40**	-0.450
VIF_n	64.28	85.71	81.81	50	72	75	70.91	-0.001

Table V. 10. Evaluation measures using each set of features separately Acqu 3 and 4 [18].

C = 0.05µl/ml								
Features	Low MI (0.2)							
	r	*Spe*	*P*	Kappa	*F*	ACC	AUC	OT
$P2TR_n$	92.85	71.42	76.47	64.28	83.87	82.14	86.73	-0.342
$TP2TR_n$	92.85	78.57	81.25	71.42	86.66	85.71	92.34	0.001
RR_n	64.28	85.71	81.81	50	72	75	64.79	0.165
FR_n	64.28	92.85	90	57.14	75	78.57	78.06	0.213
t_{sn}	92.85	85.71	86.66	**78.57**	**89.65**	**89.28**	**91.83**	-0.177
f_{sn}	78.57	92.85	91.66	71.42	84.61	85.71	93.36	0.425
T^2_{sn}	78.57	100	100	**78.57**	**88**	**89.28**	**94.38**	0.197
B^2_{sn}	78.57	92.85	91.66	71.42	84.61	85.71	92.34	-0.186
VIE_n	100	78.57	82.35	**78.57**	**90.32**	**89.28**	**96.42**	0.463
VIF_n	78.57	71.42	73.333	50	75.86	75	73.98	-0.312
Features	High MI (0.6)							
	r	*Spe*	*P*	Kappa	*F*	ACC	AUC	OT
$P2TR_n$	92.85	71.42	76.47	64.28	83.87	82.14	79.08	0.253
$TP2TR_n$	100	64.28	73.68	64.28	84.84	82.14	87.24	-0.457
RR_n	92.85	78.57	81.25	71.42	86.66	85.71	86.73	-0.352
FR_n	64.28	78.57	75	42.85	69.23	71.42	65.81	0.053
t_{sn}	64.28	100	100	64.28	78.26	82.14	86.73	0.002
f_{sn}	71.42	92.85	90.90	64.28	80	82.14	88.26	0.331
T^2_{sn}	78.57	100	100	**78.57**	**88**	**89.28**	**94.89**	0.240
B^2_{sn}	100	78.57	82.35	**78.57**	**90.32**	**89.28**	**94.38**	-0.275
VIE_n	100	64.28	73.68	64.28	84.84	82.14	81.12	-0.352
VIF_n	50	78.57	70	28.57	58.33	64.28	48.98	-0.104

After combining the features into five characteristic vector regarding the nature of each feature and introduced them separately as input parameters into the SVM model, the features $P2TR_n$, RR_n, FR_n, and VIF_n for the two concentrations do not provide significant classification rates neither at low MI (0.2) nor at high MI (0.6). When the set of features $TP2TR_n$, t_{sn}, f_{sn}, T^2_{sn}, B^2_{sn}, and VIE_n are introduced separately as input parameters into the SVM model, the correct average rate of classification of microemboli reached 89.28%, thus a significant improvement in the classification rates is observed. In order to further improve the classification rates we perform in the next section classification based on dimensionality reduction technique.

V.3-3 Classification using Dimensionality Reduction

The feature vector build in section V.3-1 is too large to be handled properly by a classifier during training. To overcome this curse of dimensionality, we perform two approaches of dimensionality reduction techniques: feature selection and feature generation.

Feature selection methods in this thesis are realized using Differential Evolution algorithm (DEFS), and Fisher score algorithm. Feature generation is achieved by the use of principal components analysis.

With the purpose of having similar chances for the three dimensionality reduction techniques, the testing set was hidden for the most part of the experiments and it was only used to ultimately check the final performances.

V.3-3.1 Differential Evolution algorithm

DEFS algorithm is a population-based stochastic search method (described in chapter II section II.3-1.1), it belongs to the family of evolutionary algorithms, it was initially proposed by Storn and Price in 1995 [79, 80]. DEFS algorithm is a wrapper feature selection approach; it conducts a search for a good subset using the classification algorithm as part of the function evaluating feature subsets. These features generates a classifier with the highest possible accuracy. We select the set of features that maximizes the AUC and thus the accuracy of the classification model (refer to Figure V.9).

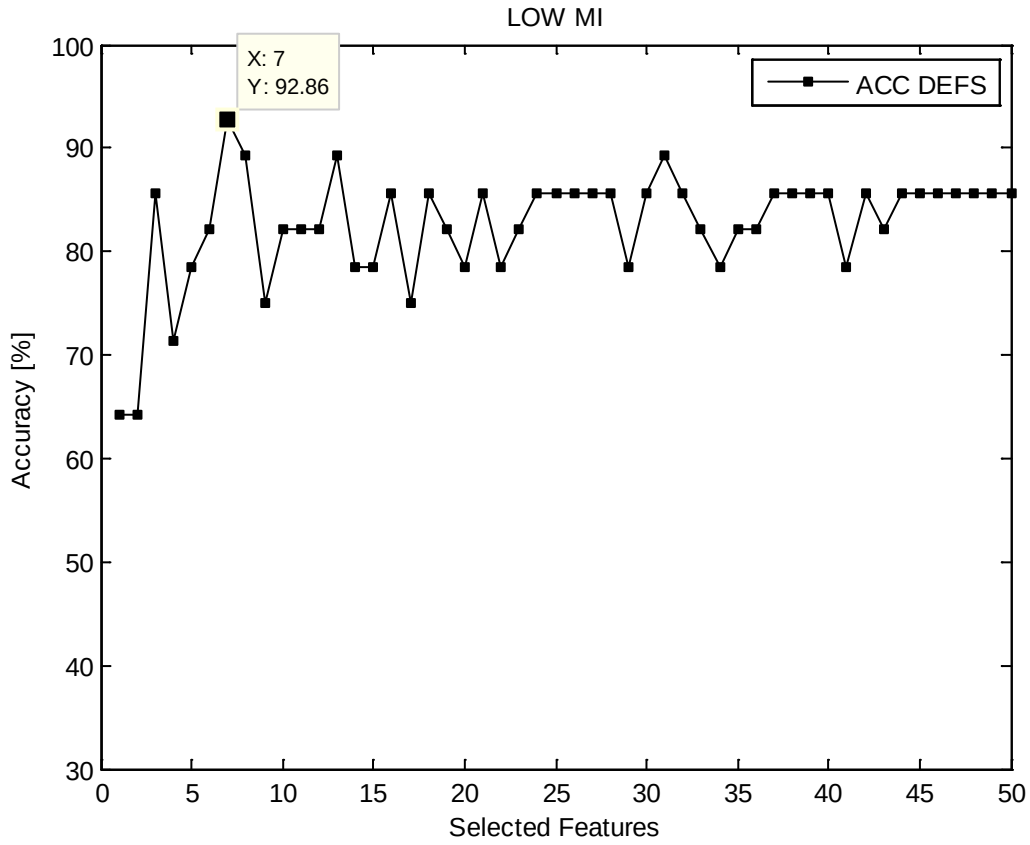

Figure V. 9. Classification rates Vs number of features selected with concentration of microbubbles (0.025µl/ml) at low MI (0.2) using DEFS algorithm.

V.3-3.2 Fisher score

Fisher score is a filter feature selection algorithm (depicted in chapter II section II.3-1.2), it is one of the most widely used supervised feature selection techniques due to its general good performance. It aims at selecting each feature independently by which the within-class distance is minimized and the between-class distance is maximized. Features are ranked in descending order from higher to lower scores, according to their corresponding Fisher criterion independently of the classification algorithm (refer to Figure V.10). After that, feature subset selection is conducted by introducing to the classifier the feature with the highest value of Fisher criterion then adding the next ranked feature until we add all the ranked features one by one. We pick up the set of features that gives the best AUC of the classification model (refer to Figure V.11).

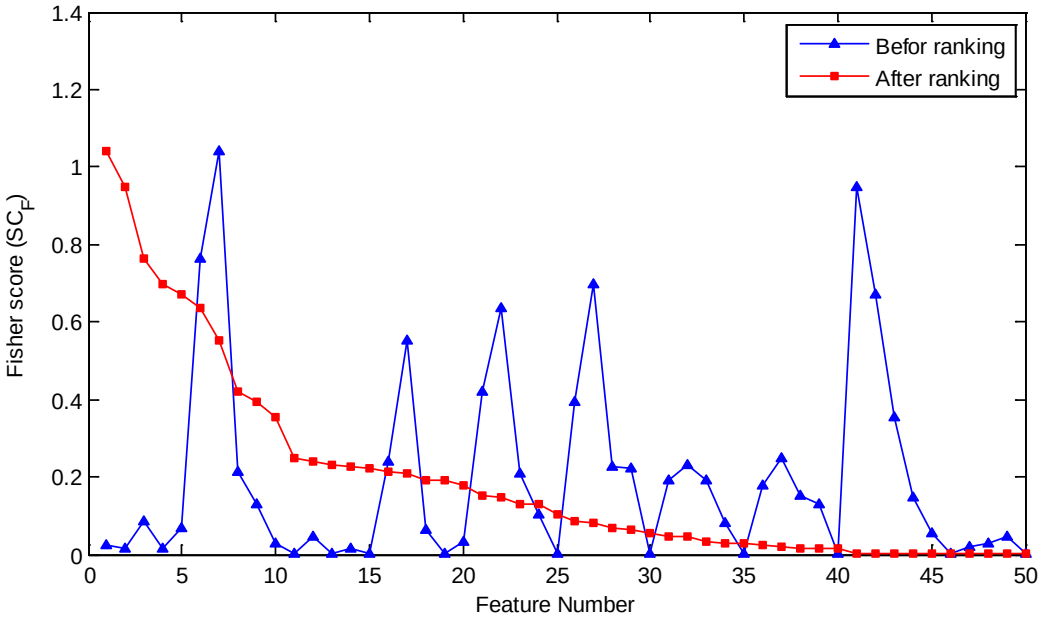

Figure V. 10. Separability (SCF) of each component of feature with concentration of microbubbles (0.025 µl / ml) at low MI (0.2).

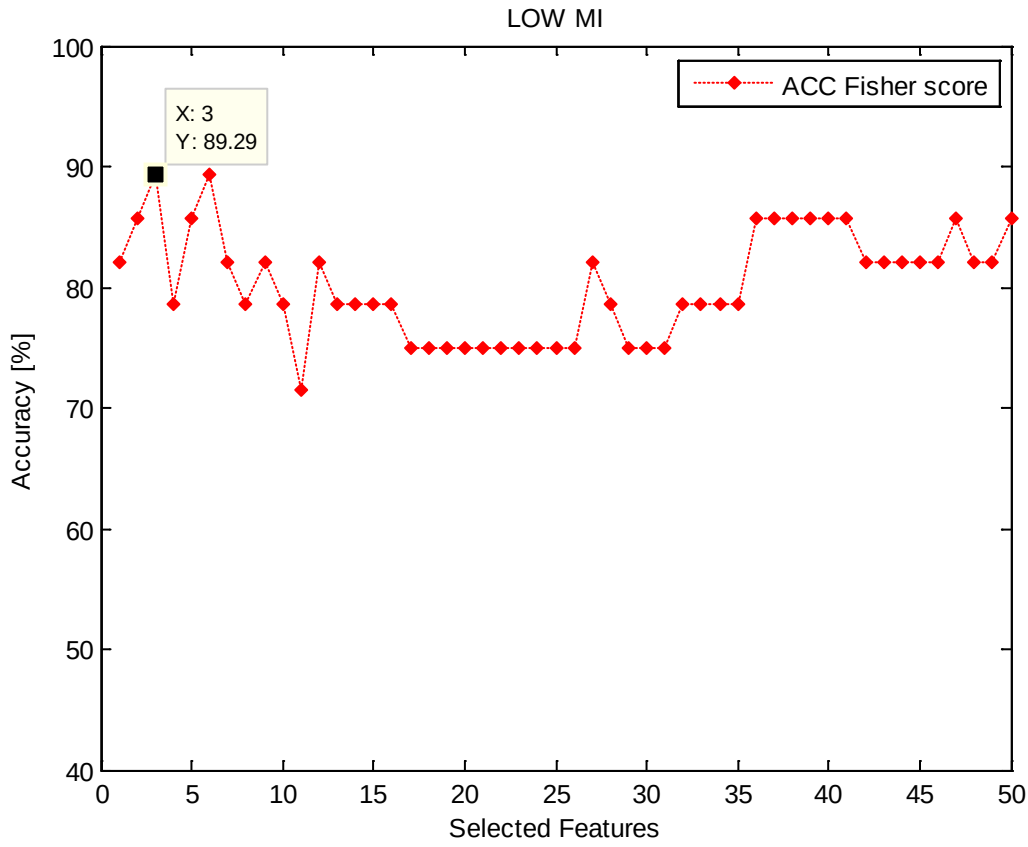

Figure V. 11. Classification rates Vs number of features selected with concentration of microbubbles (0.025µl/ml) at low MI (0.2) using Fisher Score algorithm.

V.3-3.3 Principal Component Analysis (PCA)

PCA is a feature generation technique presented in chapter II section II.3-2.1, it maps a data vector from an original space a new space to create new features that are uncorrelated over the dataset so as to conserve the maximum amount of information from the initial features. If the information associated with the first 2 or 3 principal components represents a sufficient percentage of the total variability of the dataset, the observations could be represented with these on a 2 or 3 components, thus making interpretation much easier. In our case, and since the goal is to obtain the best possible classification rates, we introduce the principal components to the SVM classifier and we select the set of component that generates the highest possible AUC (refer to figure V.12).

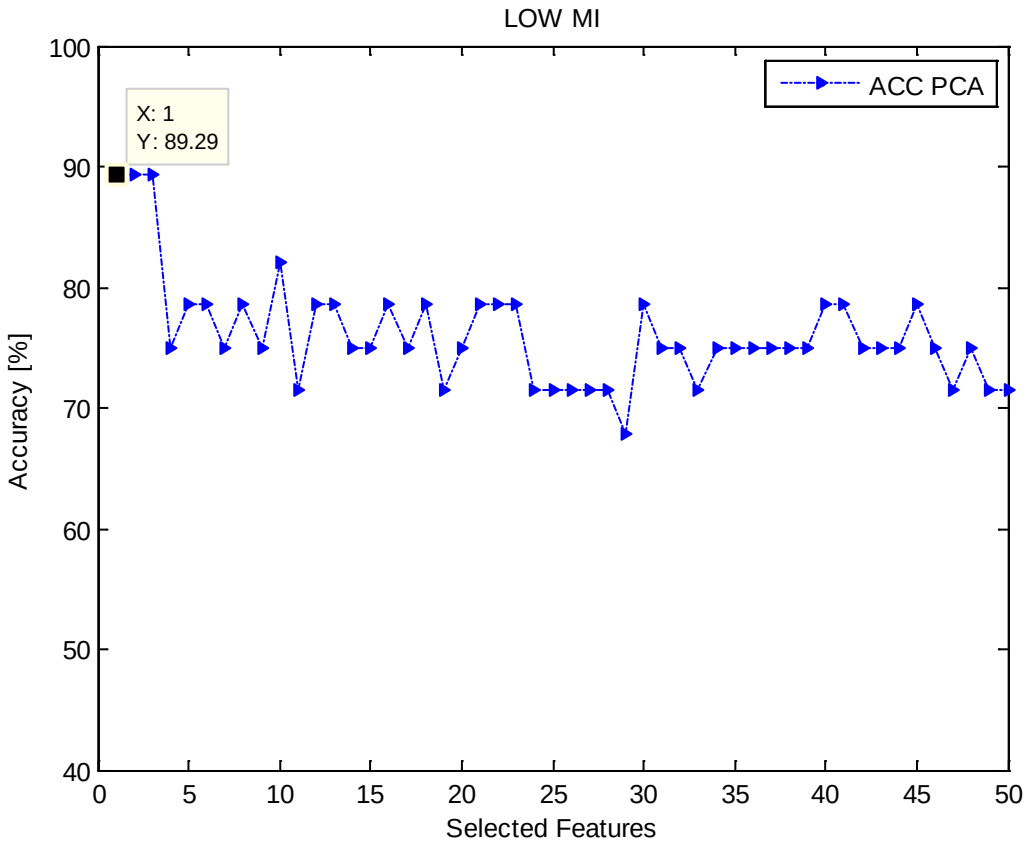

Figure V. 12. Classification rates Vs number of features selected with concentration of microbubbles (0.025µl/ml) at low MI (0.2) using PCA algorithm.

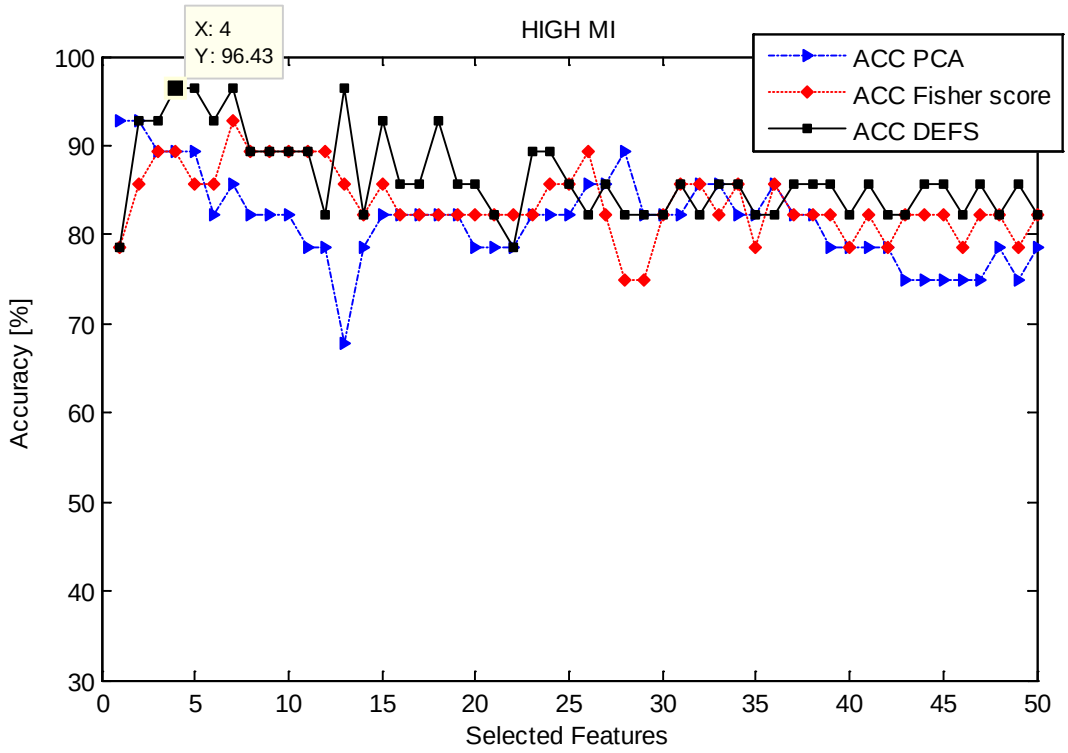

Figure V. 13. Classification rates Vs number of features selected with concentration of microbubbles (0.025µl/ml) at high MI (0.6) using 3 dimensionality reduction techniques.

Figure V.13 and Figure V.14 draw the evolution of the average classification rate Vs number of selected features using the three dimensionality reduction techniques performed in this thesis. At microbubble concentration (0.025 µl/ml) with low and high MI , the best results are obtained using DEFS algorithm (92.85% for low MI and 96.42% for high MI) with seven and four features respectively. For these two acquisitions PCA technique and Fisher score algorithm produce similar classification rates of 89,28% and 92.85% for low and high MI respectively. However, PCA method reaches its highest ACC using only 1 principal component for the two Mechanical index compared to Fisher Score algorithm which achieves the same ACC using 3 and 7 features for low and high MI respectively.

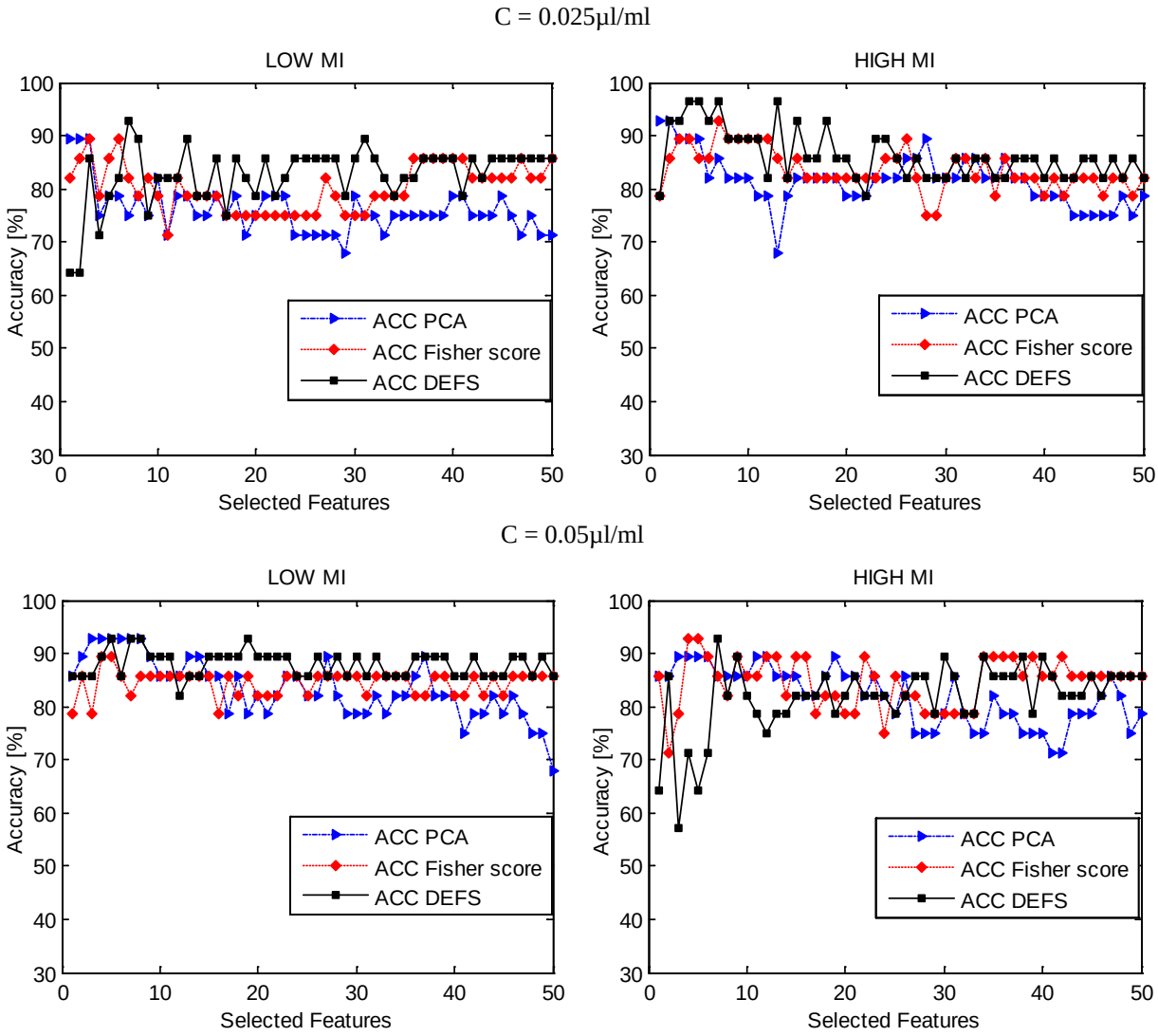

Figure V. 14. Classification rates Vs number of features selected for the four acquisitions using DEFS, Fisher score, and PCA.

At microbubble concentration (0.05 µl/ml) with low MI (0.2), PCA and DEFS achieved comparable results with an ACC of 92.85% with 3 principal component and 5 features respectively. Classification using Fisher score algorithm reached 89,28% average classification rate using 4 features. For the concentration of microbubble (0.05 µl/ml) at high MI (0.6), the best classification rates are obtained using Fisher score and DEFS algorithms with an ACC of 92.85% using a total of 4 and 7 features respectively. PCA reached an ACC of 89,28% using the first three principal components.

Table V.11 shows the final selected features for each acquisition using Differential Evolution algorithm (represented in blue) and Fisher score (represented in red) with SVM as a classifier.

Table V. 11. Selected features for each Acquisition.

Features	Nbr of features	*C = 0.025µl/ml*				*C = 0.05 µl/ml*			
		Low MI		High MI		Low MI		High MI	
		DEFS	Fisher.S	DEFS	Fisher.S	DEFS	Fisher.S	DEFS	Fisher.S
$P2TR_n$	1								
	2								
	3								
	4								
	5								
$TP2TR_n$	6								
	7								
	8								
	9								
	10								
RR_n	11								
	12								
	13								
	14								
	15								
FR_n	16								
	17								
	18								
	19								
	20								
t_{sn}	21								
	22								
	23								
	24								
	25								
f_{sn}	26								
	27								
	28								
	29								
	30								
$T^2_{s\ n}$	31								
	32								
	33								
	34								
	35								
$B^2_{s\ n}$	36								
	37								
	38								
	39								
	40								
VIE_n	41								
	42								
	43								
	44								
	45								
VIF_n	46								
	47								
	48								
	49								
	50								

Table V. 12. Generalization performances using 3 Dimensionality Reduction techniques [18].

	C = 0.025µl/ml					
	Low MI (0.2)			High MI (0.6)		
	PCA	Fisher Score	DEFS	PCA	Fisher Score	DEFS
Nbr of features | P. Components (PCA)	1	3	7	1	7	4
Sensitivity or Recall (Gaseous emboli)	100	92.85	85.71	92.85	92.85	100
Specificity (Solid emboli)	78.57	85.71	100	92.85	92.85	92.85
Precision	82.35	86.66	100	92.85	92.85	93.33
Kappa	78.57	78.57	85.71	85.71	85.71	92.85
F-measure	90.32	89.65	92.30	92.85	92.85	96.55
Accuracy	89.28	89.28	**92.85**	92.85	92.85	**96.42**
AUC (Area Under Curve)	89.79	91.83	**96.93**	95.40	97.44	**97.44**
OT: Optimal Threshold	-0.988	-0.016	0.418	-0.140	0.292	0.116
	C = 0.05µl/ml					
	Low MI (0.2)			High MI (0.6)		
	PCA	Fisher Score	DEFS	PCA	Fisher Score	DEFS
Nbr of feature | P.components (PCA)	3	4	5	3	4	7
Sensitivity or Recall (Gaseous emboli)	92.85	100	92.85	92.85	100	100
Specificity (Solid emboli)	92.85	78.57	92.85	85.71	85.71	85.71
Precision	92.85	82.35	92.85	86.66	87.50	87.50
Kappa	85.71	78.57	85.71	78.57	85.71	85.71
F-measure	92.85	90.32	92.85	89.65	93.33	93.33
Accuracy	**92.85**	89.28	**92.85**	89.28	**92.85**	**92.85**
AUC (Area Under Curve)	**90.30**	87.24	**96.93**	92.85	**94.38**	**96.93**
OT: Optimal Threshold	0.037	-0.366	0.032	-0.301	-0.111	0.089

The output of the designed approach using the three dimensionality reduction techniques and SVM classifier based on hold-out-set cross validation are illustrated in Table V.12. DEFS algorithm presents the best classification rates for the concentration of microbubbles (0.025 µl/ml) at low MI (0.2) and high MI (0.6) our proposed method achieved 92.85%, 96.42% classification rates using 7 and 4 features respectively. For the other two acquisitions the performance measures are quite similar, the proposed method reached a classification rate of 92.85%.

Table V.12 illustrates the analysis of ROC curves using PCA, Fisher score, and DEFS algorithms. The best value of accuracy based on the optimal threshold is obtained using DEFS for concentration C = 0.025µl/ml at high MI (0.6), the ROC point at (0.07, 1) produces its highest accuracy (96.42%), with an AUC of 97.44%. For all the acquisitions a significant improvement in terms of accuracy, sensitivity, and specificity is observed when using dimensionality reduction techniques.

Figure V.15 shows the PCA ROC curves of the four datasets using several detection thresholds in which TP rate is plotted on the Y axis and FP rate is plotted on the X axis. The best results that maximizes (sensitivity and specificity) are achieved for the concentration C = 0.025µl/ml at high MI (0.6) and concentration C = 0.05µl/ml at low MI (0.2) using optimal thresholds of -0.140 and 0.037 respectively. At this cut-offs, the sensitivity is 92.85% and specificity is 92.85%. The ROC curves for this two acquisitions indicate that PCA based classification algorithm recognizes solid emboli and gaseous emboli in a similar manner.

For the concentration C = 0.025µl/ml at low MI (0.2) and the concentration C = 0.05µl/ml at high MI (0.6) the proposed PCA model performs better at identifying gaseous emboli (sensitivities of 100% and 92.85% respectively) than at identifying solid emboli (specificities of 78.57% and 85.71% respectively), the ROC curve produce AUC of 89.79% and 92.85% using optimal thresholds of -0.988 and -0.301 respectively.

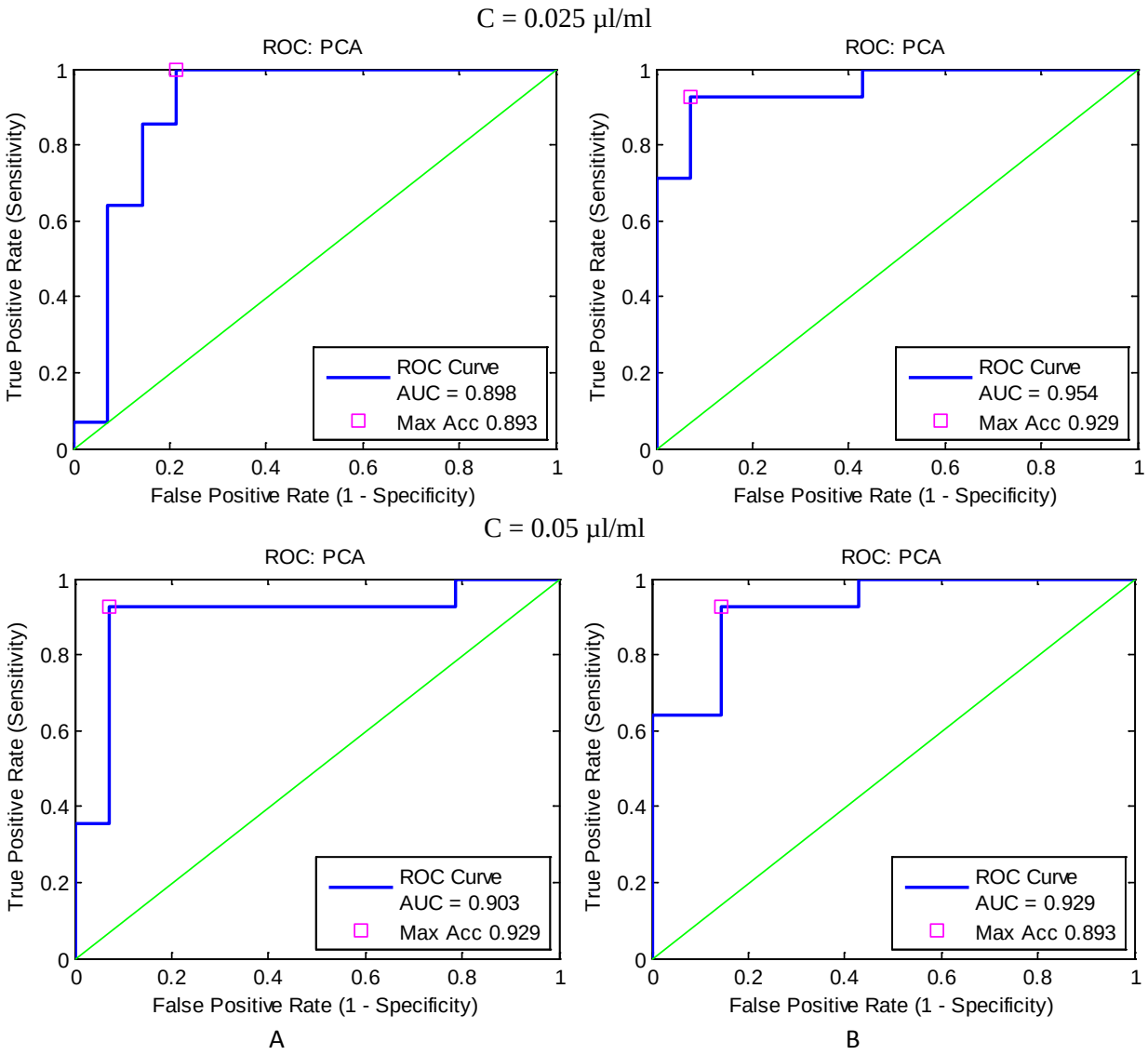

Figure V. 15. ROC curve at different detection thresholds, : A. MI= 0.2, B. MI= 0.6 for two microbubbles concentrations using PCA.

The Roc curves using Fisher score model are illustrated in Figure V.16. The best performances are obtained for the concentration C = 0.025µl/ml at high MI (0.6) and concentration C = 0.05µl/ml at high MI (0.6) with OT of 0.292 and -0.111 respectively. The ROC curve for the concentration C = 0.025µl/ml at high MI (0.6) indicates that the proposed Fisher score model recognizes solid emboli and gaseous emboli en a comparable manner with a sensitivity of 92.85% and a specificity of 92.85%. However for the concentration C = 0.05µl/ml at high MI (0.6) Fisher score model performs better at identifying gaseous emboli (sensitivity=100%) than at identifying solid emboli (specificity =78,57%).

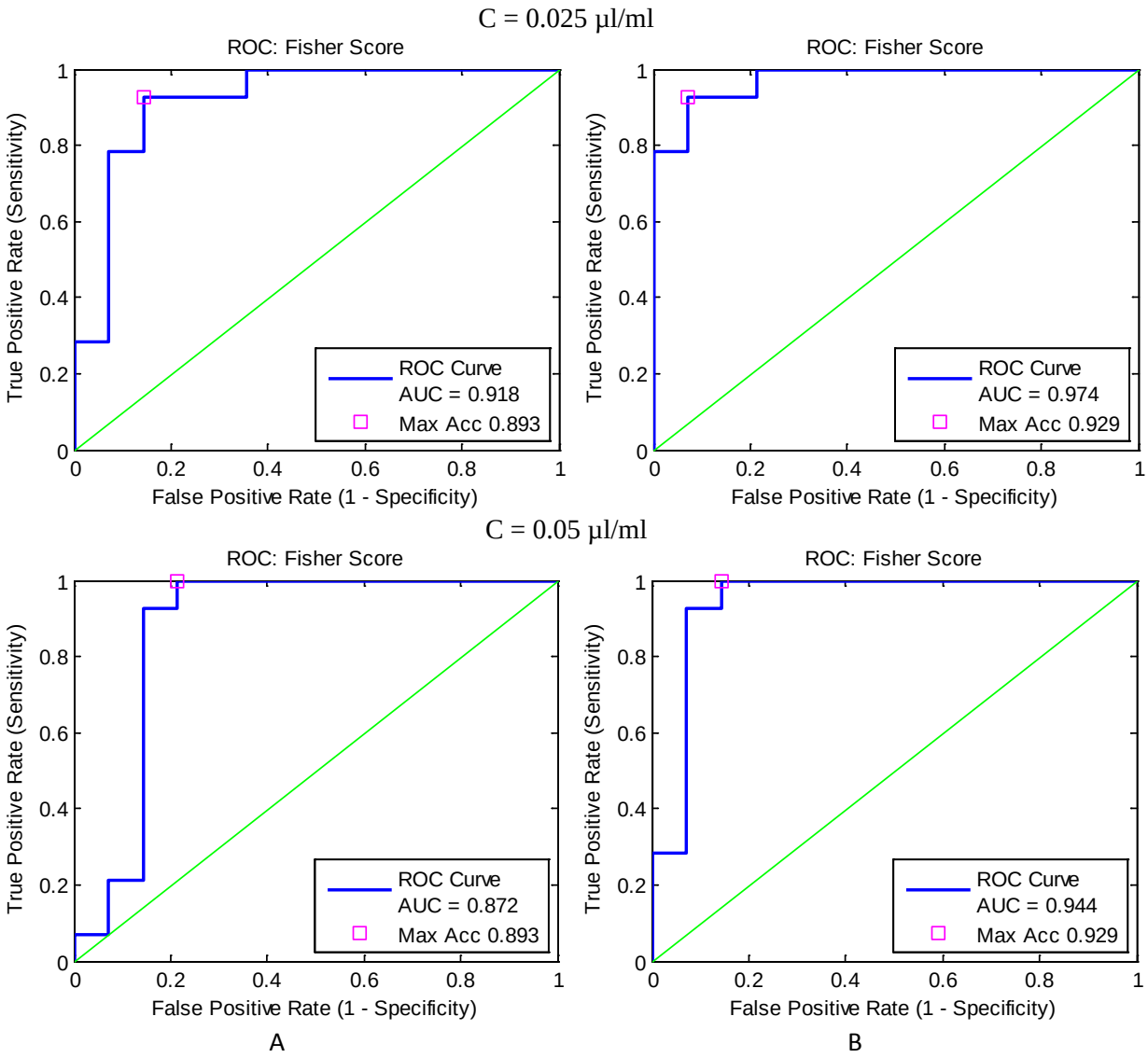

Figure V. 16. ROC curve at different detection thresholds, : A. MI= 0.2, B. MI= 0.6 for two microbubbles concentrations using Fisher score.

For the concentrations C = 0.025µl/ml and C = 0.05µl/ml at low MI (0.2), Fisher based classification model recognizes gaseous emboli (with sensitivities of 92.85 and 100% respectively) in a better way than solid emboli (with specificities of 85.71% and 78.57% respectively).

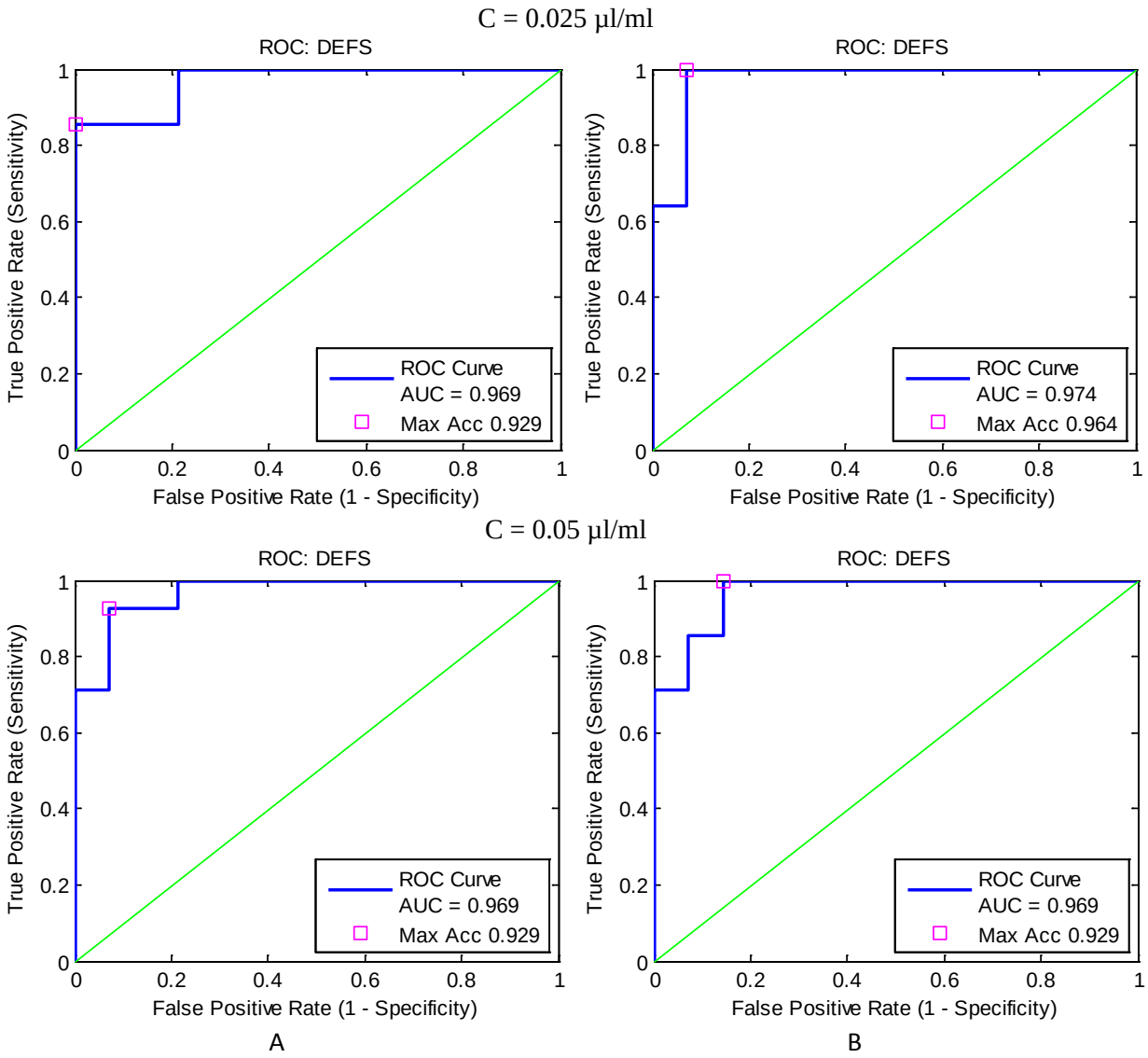

Figure V. 17. ROC curve at different detection thresholds, : A. MI= 0.2, B. MI= 0.6 for two microbubbles concentrations using DEFS [18].

Figure V.17 shows the DEFS ROC curves of the four datasets using several detection thresholds in which TP rate is plotted on the Y axis and FP rate is plotted on the X axis. The best results that maximizes (sensitivity and specificity) are achieved using a threshold of 0.1163. At this cut-offs, the sensitivity is 100% and specificity is 92.85%. The ROC curves in Figure V.17 indicate that the DEFS model performs better at identifying gaseous emboli than at identifying solid emboli for the concentrations C = 0.025µl/ml and C = 0.05µl/ml at high MI (0.6), the ROC curves produce an AUC of 97.44% and 96.93% respectively.

On the contrary, for the concentration C=0.025µl/ml at low MI (0.2), the DEFS based SVM model recognizes better solid emboli than gaseous emboli. The classification performances for gaseous and solid emboli are quite similar for the concentration C = 0.05µl/ml at low MI (0.2).

The DEFS model presents better performances compared to the PCA and the Fisher score models [18].

Table V. 13. Confusion matrix of the DEFS model [18].

		C = 0.025 µl/ml					
		Predicted					
		Low MI (0.2)		Nbr of selected features	High MI (0.6)		Nbr of selected features
		Gaseous emboli	Solid emboli		Gaseous emboli	Solid emboli	
Actual class	Gaseous emboli	12	2	07	14	0	04
	Solid emboli	0	14		1	13	
		C = 0.05 µl/ml					
		Low MI (0.2)		Nbr of selected features	High MI (0.6)		Nbr of selected features
		Gaseous emboli	Solid emboli		Gaseous emboli	Solid emboli	
Actual class	Gaseous emboli	13	1	05	14	0	07
	Solid emboli	1	13		2	12	

Table V.13 illustrates the confusion matrix of the DEFS system. The numbers of correct and incorrect predictions made by DEFS model compared to the target values in the test data are shown in Table V.13. For example, at microbubble concentration 0.025 µl/ml and high MI (0.6) the proposed classification model succeeded in classifying 14 gaseous embolus out of 14 (Sensitivity=100%) and 13 solid embolus out of 14 (Specificity =92.85%). Thus 1 solid embolus is not recognized i.e. classified as gaseous embolus, the gaseous embolus are all recognized.

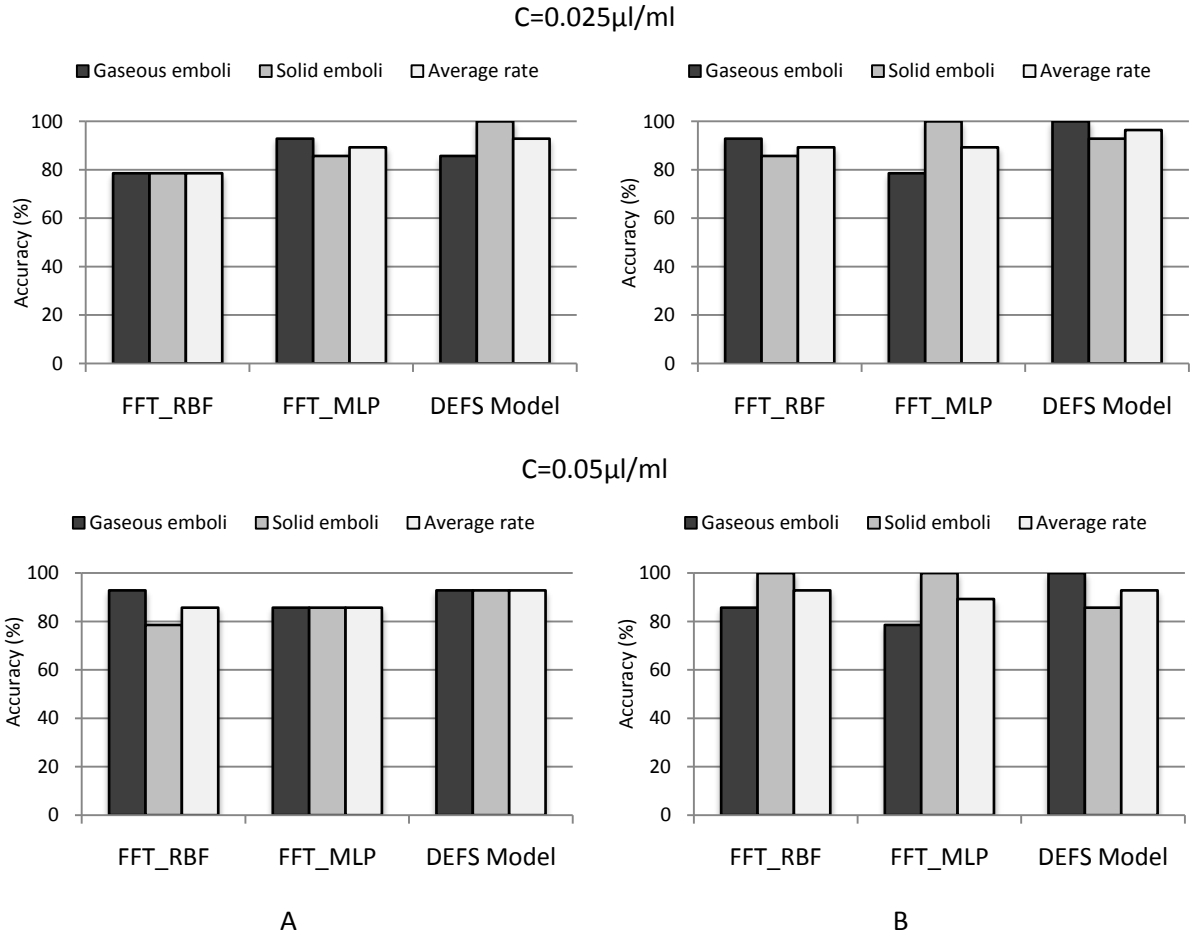

Figure V. 18. Generalisation performances using DEFS algorithm [18] and comparison with the results obtained with FFT model [24]: A. MI= 0.2, B. MI= 0.6 for two microbubbles concentrations.

In order validate the proposed approach; we compare the best proposed model (DWT based DEFS model) [18] in this study with the results obtained in our recently published study (FFT model) [24] on the same backscatter RF signals (refer to Figure V.18). The average percentage of correct classification of microemboli using DEFS algorithm with SVM classifier for two microbubbles concentrations (0.025 µl/ml and 0.05 µl/ml) at high and low mechanical index (0.2 and 0.6) are given in Table V.14.

Table V. 14. Generalisation performances using DEFS algorithm and comparison with the results obtained with the FFT model [24].

Methods (Accuracy [%])	*C = 0.025 µl/ml*				*C = 0.05 µl/ml*			
	Low MI (0.2)			High MI (0.6)	Low MI (0.2)		High MI (0.6)	
	FFT model. [24]		DWT based DEFS model [18]	FFT model. [24]	FFT model. [24]		FFT model. [24]	DWT based DEFS model [18]
	RBFN	MLP		RBFN MLP	RBFN	MLP	RBFN MLP	
Gaseous emboli	78.57	92.85	85.71	92.85 78.57	92.85	85.71	85.71 78.57	100
Solid emboli	78.57	85.71	100	85.71 100	78.57	85.71	100 100	85.71
Average rate	78.57	89.28	**92.85**	89.28 89.28	85.71	85.71	**92.85** 89.28	**92.85**

V.3-6 Discussion

In this experimental study, we exploit RF signals in the detection and the classification of microemboli into gaseous or solid embolus. Several features are evaluated from the detail coefficients using DWT technique. It should be noted that the features used in this study are the same used in the work by N. Aydin et al. [25]. These features are used as inputs to the classification models without dimensionality reduction method. The average classification rate doesn't exceed 89.28% for all datasets, this can be explained by the fact that even the more powerful among the existing machine learning algorithms tend to get confused when supplied with a large number of features.

Building quantitative models (classifiers) using a large number of features most often requires using a smaller set a features than the initial one. Indeed, a too large number of features feed to a model (classifier) results in a too large number of parameters, leading to overfitting and poor generalization abilities [105]. It is noteworthy, in our case, the original data set contains d features (d = 50), an extensive search of all possible combinations would involve the design of 2^{d-1} different models. This value grows exponentially, making an exhaustive search impractical even for moderate values of d. In order to reduce the dimensionality and select a relevant set of features, we implement three dimensionality reduction techniques based on differential evolution, Fisher score, and PCA algorithms. For all the acquisitions a significant improvement in the classification rates is observed when using dimensionality reduction methods. The average classification rate goes down when the number of selected features gets larger which validates that learning might be deteriorated by irrelevant features (refer to Figure V.13 and Figure V.14).

We employ seven evaluation measures such as: Recall (Sensitivity), Specificity, Precision, Kappa coefficient, F-measure, overall accuracy, and AUC (Area Under Curve). These performance measures are used to discriminate relevant information that provide more insight into the characteristics of the model in order to make meaningful decisions. Sensitivity relates to a test's ability to correctly identify those patients with pathology as positive. Specificity of a test refers to its ability to correctly identify individuals without the pathology as negative. Precision measures that fraction of patients classified as positive that are truly positive. Recall and Precision are combined as their harmonic mean, known as the F-measure. Kappa is a coefficient developed to measure agreement among observers. Furthermore, we

investigate other statistical measure which better estimates the accuracy of a given trial test by analyzing sensitivity and specificity simultaneously, this approach is the area under curve (AUC) associated to the receiver operating characteristic (ROC) curve. AUC allows to quantify the ROC curve performance using a single value. It is well known that the higher the AUC value, the more efficient the classifier.

The best results are obtained using DEFS algorithm [18]. The superiority of DEFS Algorithm over PCA and Fisher score techniques is due to process of selection of the best set of features; DEFS technique employs the classification algorithm (SVM in this case) as part of the function evaluating each set of features. However, this process is time consuming in the training and feature selection step compared to PCA and Fisher score algorithms in which the evaluation of the features is conducted independently of the classification algorithm. Fisher Score model and PCA model present similar performances. However, PCA method reach its highest ACC using only the first three principal components compared to Fisher Score algorithm which achieves the same ACC using more than 3 features. This can be explained by the fact that the first three principal components preserve the maximum amount of information from the initial features.

In order validate the proposed approach; we compare the obtained results (DWT based DEFS model) [18] in this study with those obtained in our recently published study [24] on the same backscatter RF signals (refer to Table V.14). In the FFT model [24] we employ a neural network (MLP and RBFN) analysis using the fundamental and the second harmonic components information contained in the RF signal backscattered by an embolus. The experimental results show clearly that our proposed method (DWT based DEFS model) achieves better average classification rates compared to the method cited in [24] using also the same backscatter RF signals.

The superiority the DWT based DEFS and SVM approach over the FFT based Neural Network approach, can be explained by the fact that: (i) DWT is well localized in both time and frequency domain whereas FFT is only localized in frequency domain. (ii) The use of dimensionality reduction technique (DEFS) reduces the size of input vector; therefore, finds the most relevant set of feature that result in higher average classification rate. (iii) SVM has a high capacity for generalization using limited numbers of training data points; furthermore, SVMs don't have local extrema problems that are present for neural networks, which involve

large numbers of training patterns. The performance of SVMs relies on the choice of kernel type and kernel parameters, but this dependence is less influential. (iv) Besides, testing all possible cut-offs using ROC analysis and choosing the optimal threshold lead to better classification rates compared to the fixed threshold of 0.5 adopted in FFT based approach (chapter II) [24].

It is noteworthy that the results depicted by Tables V.8 to V.14 are reproducible. The best results appear in bold. The algorithm has only access to the training and validation sets, the test set is kept unseen in the selection process of the best model. The test set is used only for the assessment of the model selected by the cross-validation technique.

V.4 Conclusion

The results presented in this experimental study demonstrate the usefulness of RF ultrasound signal processing in detection and classification of microemboli. A first proof of concept of emboli classification based on the combination of a time-frequency based feature extraction technique (discrete wavelet transform), dimensionality reduction methods (DEFS, PCA, and Fisher score), and backscatter RF signals is demonstrated. The results indicate that dimensionality reduction not only has the ability to find the most relevant set of inputs that result in higher average classification rate but also has the ability to reduce the size of feature vector. We demonstrate in this experimental study that combining DEFS algorithm and discrete wavelet transform [18] provides better average classification rates (96.42%) in comparison to our previous study using also the same backscatter RF signal [24] that is evaluated extensively in a comparable manner.

Conclusions and perspectives

Conclusions and perspectives

Emboli detection and classification remain a promising research area due to the correlation between embolism consequences and embolus nature (gaseous or solid emboli). The detection and classification of circulating microemboli is nowadays considered as a main challenge in the field of emboli detection. In the human body; emboli can produce severe damage like stroke or heart attack thus the importance of an automatic classification system.

This thesis presented a study on how microemboli problems can be detected and characterized. It investigated a novel approach to the detection and classification of microemboli using Radio-Frequency (RF) ultrasound signals and artificial intelligence techniques. Emboli classification is of high clinical importance for selecting appropriate patient treatment. Several ultrasonic methods using Doppler processing have been used for emboli detection and classification as solid or gaseous matter. Until now, Doppler techniques have shown some limitations to determine clearly the nature of circulating microemboli. Under specific conditions of the ultrasound excitation wave, gaseous bubbles show a nonlinear behavior exploited in this work to distinguish gaseous from solid microemboli. Therefore, we suggested in this experimental study to focus on Radio-Frequency ultrasound signals backscattered by the emboli since they contain additional information about the embolus than the commonly used Doppler signal.

The proposed experimental set-up in this thesis is developed at the University of François Rabelais Tours, France in the INSERM U930 laboratory under the direction of Professor A. Bouakaz. It consists of an Anthares scanner with RF access with a transmit frequency of 1.82 MHz at two mechanical indices (MI) 0.2 and 0.6. To imitate emboli US behavior, Sonovue microbubbles are injected at two different concentrations (10µl and 5µl) in a nonrecirculating flow phantom with a 0.8 mm diameter vessel at a constant flow. Non perfused tissue is assumed to behave as solid emboli. Sonovue concentration is chosen such that fundamental scattering from tissue and contrast are identical. As a result, we obtain four datasets, each dataset consists of 102 samples (51 gaseous emboli and 51 solid emboli). This dataset is used to create a number of discriminative features exploited for the detection and classification of circulating microemboli.

At first, we employed Fast Fourier Transform (FFT) and artificial neural network models for the analysis of RF signals backscattered by gaseous and solid emboli. The results demonstrated the opportunity to classify emboli based on a RF signals by exploiting the nonlinear behaviour of gaseous emboli. The proposed model reached a classification rate of 92.85%.

In view of the fact that several researchers have revealed that discrete wavelet transform performs in a better way than Fast Fourier Transform for the analysis of embolic signals, we employed at a second stage DWT for the analysis of RF signals backscattered by gaseous and solid emboli. We described a strategy to choose the appropriate mother wavelet among 59 mother wavelet functions. Moreover, we proposed another classification system of microemboli using three dimensionality reduction technique (Differential Evolution algorithm, Fisher Score method, and Principal Component Analysis), support vector machines (SVM), and the backscattered RF signals based on the selected wavelet filter. DEFS based approach provides better average classification rates (96.42%) in comparison to the previous study using FFT approach.

With the ability to localize well both in time and frequency, wavelet based dimensionality reduction technique presents higher overall classification accuracies than FFT based neural network approach. Nevertheless, it would be interesting to incorporate both FFT and DWT approaches together in the same classification model.

The immediate extension of the study presented in this thesis include the use of circulating solid emboli instead of surrounding tissue. We should also test the proposed algorithms on a larger dataset and in animal experiments. Besides, we intend to exploit subharmonics in order to allow better discrimination of solid and gaseous emboli.

The combination of classifiers, would simplify the decision-making process. Ensemble classifiers could be an alternative to the stand alone artificial neural network models or the support vector machines.

According to the obtained results, one may need to combine other types of approaches (e.g., filter and embedded) in order to improve the discriminative power of the proposed method. The processing time is an essential consideration if we have to implement this approach in clinical situation. It should be noted that the training/feature selection phase lasts for a few minutes while the processing time for the test phase (classification) is less than 1s.

We demonstrated in this in vitro study, a first proof of concept of emboli classification based on the combination of data mining techniques, signal processing methods, and Radio Frequency information extracted from gaseous and solid emboli. The technique as suggested in this study proves to be effective in improving classification. The implementation of such algorithm in real time applications makes also the investigation of the feasibility of emboli detection systems using RF signal worthwhile. It may let a surgeon, for example, know that something is causing emboli. However, further validations in in-vivo situations are required to demonstrate the additional benefit.

The studies described in this thesis contribute to the general knowledge on the detection and classification problem of microemboli and offer more insight to the use of the RF signals instead of Doppler signals to classify embolic signals. Our conviction is that Radio Frequency ultrasound signals bring real opportunities for microemboli detection and classification and should be also used in combination with Doppler approach in order to improve the discrimination rate. Although the clinical utility still needs evaluation and validation in practical diagnosis, the main message of this study is to validate this strategy in a simple and a controlled experimental environment before further pre-clinical and clinical validations are undertaken.

References

[1] PIPER Keaton, ALGATTAS Hanna, DEANDREA-LAZARUS Ian A, KIMMELL Kristopher T, LI Yan Michael, WALTER Kevin A, SILBERSTEIN Howard J, and VATES G Edward. Risk factors associated with venous thromboembolism in patients undergoing spine surgery. Journal of Neurosurgery: Spine, 2017, vol. 26, no 01, p. 90-96.

[2] KOJURI Javad, MEHDIZADEH Morteza, ROSTAMI Hamed, and SHAHIDIAN Danial. Clinical significance of retinal emboli during diagnostic and therapeutic cardiac catheterization in patients with coronary artery disease. BMC cardiovascular disorders, 2011, vol. 11, no 01, p. 5.

[3] FARGE Dominique, BOUNAMEAUX Henri, BAUERSACHS Rupert M, and BRENNER Benjamin. Women, thrombosis, and cancer: A gender-specific analysis. Thrombosis Research, 2017, vol. 151, p. S21-S29.

[4] BECATTINI Cecilia, AGNELLI Giancarlo, LANKEIT Mareike, MASOTTI Luca, PRUSZCZYK Piotr, CASAZZA Franco, VANNI Simone, NITTI Cinzia, KAMPHUISEN Pieter, and VEDOVATI Maria Cristina. Acute pulmonary embolism: mortality prediction by the 2014 European Society of Cardiology risk stratification model. European Respiratory Journal, 2016, vol. 48, no 03, p. 780-786.

[5] HARRIS Adam A, and BROWN David L. Evaluation of Patients with Suspected Cardiac Sources of Emboli. In Evidence-Based Cardiology Consult, Springer London, 2014, p. 539-551.

[6] RUSSELL David A, ROBINSON Graham J, and JOHNSON Brian F. Popliteal venous aneurysm: a rare cause of recurrent pulmonary emboli and limb swelling. Cardiovascular and interventional radiology, 2008, vol. 31, no 05, p. 1026-1029.

[7] PETRACCA Martina, CALANDRELLI Rosalinda, BROCCOLINI Aldobrando, CALIANDRO Pietro, DELLA Marca Giacomo, FRISULLO Giovanni, MOROSETTI Roberta, PROFICE Paolo, LAMENDOLA Priscilla, and PENNESTR Faustino. Thrombus in Transit: A Potentially Life-threatening Complication of Cerebral Sinus Thrombosis. The Neurologist, 2017, vol. 22, no 01, p. 21-23.

[8] AUSTEN W Gerald, and HOWRY Douglass H. Ultrasound as a method to detect bubbles or particulate matter in the arterial line during cardiopulmonary bypass. Journal of Surgical Research, 1965, vol. 05, no 06, p. 283-284.

[9] SPENCER Merrill P, THOMAS George I, NICHOLLS Stephen C, and SAUVAGE Lester R. Detection of middle cerebral artery emboli during carotid endarterectomy using transcranial Doppler ultrasonography. Stroke, 1990, vol. 21, no 03, p. 415-423.

[10] BASCIANI Reto, KRÖNINGER Felix, GYGAX Erich, JENNI Hansjörg, REINEKE David, STUCKI Monika, HAGENBUCH Niels, CARREL Thierry, EBERLE Balthasar, and ERDOES Gabor. Cerebral Microembolization During Aortic Valve Replacement Using Minimally Invasive or Conventional Extracorporeal Circulation: A Randomized Trial. Artificial organs, 2016, vol. 40, no 12, p. E280–E291.

[11] MARTIN Kristin K, WIGGINTON Jeremy B, BABIKIAN Viken L, POCHAY Val E, CRITTENDEN Michael D, and RUDOLPH James L. Intraoperative cerebral high-intensity transient signals and postoperative cognitive function: a systematic review. The American Journal of Surgery, 2009, vol. 197, no 01, p. 55-63.

[12] PATEL Nikil, MINHAS Jatinder S, and CHUNG Emma ML. Intraoperative embolization and cognitive decline after cardiac surgery: a systematic review. In : Seminars in cardiothoracic and vascular anesthesia. Sage CA: Los Angeles, CA : SAGE Publications, 2016. vol. 20, no. 03 p. 225-231.

[13] MARKUS Hugh S, and PUNTER Martin. Can transcranial Doppler discriminate between solid and gaseous microemboli?. Stroke, 2005, vol. 36, no 08, p. 1731-1734.

[14] RODRIGUEZ Rosendo A, GIACHINO Allan, HOSKING Martin, and NATHAN Howard J. Transcranial Doppler characteristics of different embolic materials during in vivo testing. Journal of Neuroimaging, 2002, vol. 12, no 03, p. 259-266.

[15] VUKOVIĆ-CVETKOVIĆ Vlasta. Microembolus detection by transcranial Doppler sonography: review of the literature. Stroke research and treatment, 2011, vol. 2012, p. 1-7.

[16] PALANCHON Peggy, BOUAKAZ Ayache, KLEIN Jan, and De JONG Nico. Multifrequency transducer for microemboli classification and sizing. IEEE transactions on biomedical engineering, 2005, vol. 52, no 12, p. 2087-2092.

[17] TRANQUART François, CORREAS Jean-Michel, and BOUAKAZ, Ayache. Echographie de contraste: méthodologie et applications cliniques. Springer Science & Business Media, 2007.

[18] **FERROUDJI Karim**, BENOUDJIT Nabil, and BOUAKAZ Ayache. An automated microemboli detection and classification system using backscatter RF signals and differential evolution. Australasian Physical & Engineering Sciences in Medicine, 2017, vol. 40, no 01, p.85-99.

[19] DOUAK Fouzi, TAFSAST Abdelghani, FOUAN Damien, **FERROUDJI Karim**, BOUAKAZ Ayache, and BENOUDJIT Nabil . A wavelet optimization approach for microemboli classification using RF signals. In : Ultrasonics Symposium (IUS), IEEE International. IEEE, 2016. p. 1-4.

[20] **FERROUDJI Karim**, BENOUDJIT Nabil, and BOUAKAZ Ayache. Empirical mode decomposition based support vector machines for microemboli classification. In 8th International Workshop on: Systems, Signal Processing and their Applications (WoSSPA), IEEE, 2013. p. 84-88.

[21] **FERROUDJI Karim**, BAHAZ Mohamed, BENOUDJIT Nabil, and BOUAKAZ Ayache. Microemboli Classification using Non-linear Kernel Support Vector Machines and RF signals. Rev. des Sci. la Technol, 2012, vol. 03, p. 79-87.

[22] **FERROUDJI Karim**, BAHAZ Mohamed, BENOUDJIT Nabil, and BOUAKAZ Ayache. Selection of a suitable mother wavelet for microemboli classification using SVM and RF signals. In : 24th International Conference on Microelectronics (ICM), IEEE, 2012. p. 1-4.

[23] **FERROUDJI Karim**, BAHAZ Mohamed, BENOUDJIT Nabil, and BOUAKAZ Ayache. Feature selection based on RF signals and KNN Rule: Application to microemboli classification. In 7th International Workshop on: Systems, Signal Processing and their Applications (WOSSPA), IEEE, 2011. p. 251-254.

[24] BENOUDJIT Nabil, **FERROUDJI Karim**, BAHAZ Mohamed, and BOUAKAZ Ayache. In vitro microemboli classification using neural network models and RF signals. Ultrasonics, 2011, vol. 51, no 03, p. 247-252.

[25] AYDIN Nizamettin, MARVASTI Farrokh, and MARKUS Hugh S. Embolic Doppler ultrasound signal detection using discrete wavelet transform. IEEE Transactions on Information Technology in Biomedicine, 2004, vol. 08, no 02, p. 182-190.

[26] SERBES Gorkem, and AYDIN Nizamettin. Modified dual tree complex wavelet transform for processing quadrature signals. Biomedical Signal Processing and Control, 2011, vol. 06, no 03, p. 301-306.

[27] AYDIN Nizamettin, PADAYACHEE Soundrie, and MARKUS Hugh S. The use of the wavelet transform to describe embolic signals. Ultrasound in medicine & biology, 1999, vol. 25, no 06, p. 953-958.

[28] PRANDONI P, LENSING AWA, PRINS MH, BARON-ESQUIVIAS G, MARTÍNEZ-ALDAY J, MARTÍN A, MOYA A, SUTTON R, and AMMIRATI F. Pulmonary Embolism in Patients Hospitalized for Syncope. N Engl J Med, 2017, vol. 2017, no 376, p. 494-497.

[29] JEAN-PHILIPPE Rivière. Thrombose, phlébite, embolie : quels sont vos risques? 2003 from: [http://www.doctissimo.fr/html/sante/mag_2003/sem01/mag0627/sa_6870_thrombose_risques.htm]

[30] TOMITA Hirofumi, HAGII Joji, and OKUMURA Ken. Severity and Outcomes of Intracerebral Bleeding and Cardiac Cerebral Embolism. In : Treatment of Non-vitamin K Antagonist Oral Anticoagulants. Springer Singapore, 2017. p. 41-51.

[31] SAMARDZIC Kristian, SAMARDZIC Pejo, VUJEVA Bozo, PRVULOVIC Djeiti, and LATIC-HODZIC Leila. Embolism in retinal circulation after invasive cardiovascular procedures. Medical Archives, 2012, vol. 66, no 01, p. 66.

[32] Kobayashi Nobuaki, Shibata Yusaku, Hata Noritake, and Shimizu Wataru. Formation of Infectious Coronary Artery Aneurysms After Percutaneous Coronary Intervention in a Patient With Acute Myocardial Infarction Due to Septic Embolism. JACC: Cardiovascular Interventions, 2017, vol. 10, no 03, p. E21-E22.

[33] KANAYAMA Naohiro, INORI Junko, ISHIBASHI-UEDA Hatsue, TAKEUCHI Makoto, NAKAYAMA Masahiro, KIMURA Satoshi, MATSUDA Yoshio, YOSHIMATSU Jun, and IKEDA Tomoaki. Maternal death analysis from the Japanese autopsy registry for recent 16 years: significance of amniotic fluid embolism. Journal of Obstetrics and Gynaecology Research, 2011, vol. 37, no 01, p. 58-63.

[34] RISKA Erik B., and MYLLYNEN P. Fat embolism in patients with multiple injuries. Orthopedic Trauma Directions, 2009, vol. 07, no 06, p. 29-33.

[35] MCCARTHY Colin J, BEHRAVESH Sasan, NAIDU Sailendra G, and OKLU Rahmi. Air Embolism: Diagnosis, Clinical Management and Outcomes. Diagnostics, 2017, vol. 07, no 01, p. 5.

[36] MUTH Claus M, and SHANK Erik S. Gas embolism. New England Journal of Medicine, 2000, vol. 342, no 07, p. 476-482.

[37] DI NISIO Marcello, VAN ES Nick, and BÜLLER Harry R. Deep vein thrombosis and pulmonary embolism. The Lancet, 2017, vol. 388, no 10063, p. 3060-3073.

[38] RIES S, KNAUTH M, KERN R, KLINGMANN C, DAFFERTSHOFER M, SARTOR K, and HENNERICI M. Arterial gas embolism after decompression: correlation with right-to-left shunting. Neurology, 1999, vol. 52, no 02, p. 401-401.

[39] WOLF Lorenzo Guerrieri, CHOUDHARY Bikram P, ABU-OMAR Yasir, and TAGGART David P. Solid and gaseous cerebral microembolization after biologic and mechanical aortic valve replacement: investigation with multirange and multifrequency transcranial Doppler ultrasound. The Journal of thoracic and cardiovascular surgery, 2008, vol. 135, no 03, p. 512-520.

[40] PADAYACHEE TS, PARSONS S, THEOBOLD R, LINLEY J, GOSLING RG, and DEVERALL PB. The detection of microemboli in the middle cerebral artery during cardiopulmonary bypass: a transcranial Doppler ultrasound investigation using

membrane and bubble oxygenators. The Annals of thoracic surgery, 1987, vol. 44, no 03, p. 298-302.

[41] LAROVERE Kerri L and O'BRIEN Nicole F. Transcranial Doppler Sonography in Pediatric Neurocritical Care. Journal of Ultrasound in Medicine, 2015, vol. 34, no 12, p. 2121-2132.

[42] BRUCHER Rainer and RUSSELL David. Automatic online embolus detection and artifact rejection with the first multifrequency transcranial Doppler. Stroke, 2002, vol. 33, no 08, p. 1969-1974.

[43] ROY Emmanuel, MONTRÉSOR Silvio, ABRAHAM Pierre, and SAUMET Jean-Louis. Spectrogram analysis of arterial Doppler signals for off-line automated HITS detection. Ultrasound in medicine & biology, 1999, vol. 25, no 03, p. 349-359.

[44] LUI Ping-Wing, CHAN Brent CB, CHAN Francis HY, POON Paul WF, WANG Hsin, and LAM FK. Wavelet analysis of embolic heart sound detected by precordial Doppler ultrasound during continuous venous air embolism in dogs. Anesthesia & Analgesia, 1998, vol. 86, no 02, p. 325-331.

[45] GIRAULT J-M, KOUAMÉ Denis, OUAHABI Abdeldjalil, and PATAT Frédéric. Micro-emboli detection: an ultrasound Doppler signal processing viewpoint. IEEE Transactions on biomedical Engineering, 2000, vol. 47, no 11, p. 1431-1439.

[46] VALTON Luc, LARRUE Vincent, LE TRAON Anne Pavy, MASSABUAU Pierre, and GÉRAUD Gilles. Microembolic signals and risk of early recurrence in patients with stroke or transient ischemic attack. Stroke, 1998, vol. 29, no 10, p. 2125-2128.

[47] TELMAN G, SPRECHER E, and KOUPERBERG E. Potential relevance of low-intensity microembolic signals by TCD monitoring. Neurological Sciences, 2011, vol. 32, no 01, p. 107-111.

[48] VUKOVIĆ Vlasta, LOVRENČIĆ-HUZJAN Arijana, and DEMARIN Vida. Microembolus Detection by Transcranial Doppler Sonography. Technical and Clinical Aspects. Acta Clinica Croatica, 2005, vol. 44, no 01, p. 33-45.

[49] GRAMIAK Raymond and SHAH Pravin M. Echocardiography of the aortic root. Investigative radiology, 1968, vol. 03, no 05, p. 356-366..

[50] APPIS Andrew W, TRACY Melissa J, and FEINSTEIN Steven B. Update on the safety and efficacy of commercial ultrasound contrast agents in cardiac applications. Echo research and practice, 2015, vol. 02, no 02, p. R55-R62.

[51] SCHNEIDER M. SonoVue, a new ultrasound contrast agent. European radiology, 1999, vol. 09, no 03, p. S347-S348.

[52] PALANCHON P, BOUAKAZ Ayache, KLEIN Jan, and De JONG Nico. Emboli detection using a new transducer design. Ultrasound in medicine & biology, 2004, vol. 30, no 01, p. 123-126.

[53] PALANCHON P, BOUAKAZ Ayache, KLEIN Jan, and De JONG Nico. Subharmonic and ultraharmonic emissions for emboli detection and characterization. Ultrasound in medicine & biology, 2003, vol. 29, no 03, p. 417-425.

[54] PALANCHON P, BOUAKAZ Ayache, Van BLANKENSTEIN Jan Heim, KLEIN Jan, BOM N, and De JONG Nico. New technique for emboli detection and discrimination based on nonlinear characteristics of gas bubbles. Ultrasound in medicine & biology, 2001, vol. 27, no 06, p. 801-808.

[55] BOUAKAZ Ayache, FRINKING Peter JA, De JONG Nico, and BOM Nicolaas. Noninvasive measurement of the hydrostatic pressure in a fluid-filled cavity based on the disappearance time of micrometer-sized free gas bubbles. Ultrasound in medicine & biology, 1999, vol. 25, no 09, p. 1407-1415.

[56] BRAMER Max. Principles of data mining. Springer, 2016.

[57] BREIMAN Leo and SPECTOR Philip. Submodel selection and evaluation in regression. The X-random case. International statistical review/revue internationale de Statistique, 1992, p. 291-319.

[58] GRAUPE Daniel. Principles of artificial neural networks. World Scientific, 2013.

[59] DU Ke-Lin and SWAMY M. N. S. Radial basis function networks. In : Neural Networks and Statistical Learning. Springer London, 2014. p. 299-335.

[60] SHANTHI D, SAHOO G, and SARAVANAN N. Designing an artificial neural network model for the prediction of thrombo-embolic stroke. International Journals of Biometric and Bioinformatics (IJBB), 2009, vol. 03, no 01, p. 10-18.

[61] MATOS S, RUANO M Graca, RUANO AE, and EVANS DH. Neural network classification of cerebral embolic signals. In : Engineering in Medicine and Biology Society, 2001. Proceedings of the 23rd Annual International Conference of the IEEE. IEEE, 2001. p. 1761-1764.

[62] TOURASSI Georgia D, FLOYD Carey E, SOSTMAN H Dirk, and COLEMAN R Edward. Acute pulmonary embolism: artificial neural network approach for diagnosis. Radiology, 1993, vol. 189, no 02, p. 555-558.

[63] BENOUDJIT Nabil and VERLEYSEN Michel. On the kernel widths in radial-basis function networks. Neural Processing Letters, 2003, vol. 18, no 02, p. 139-154.

[64] DUDA, Richard O., HART, Peter E., et STORK, David G. Pattern classification. John Wiley & Sons, 2012.

[65] DEMUTH Howard B, BEALE Mark H, DE JESS Orlando, and HAGAN Martin T. Neural network design. Martin Hagan, 2014.

[66] JAIN Lakhmi, SEERA Manjeevan, LIM Chee, and BALASUBRAMANIAM Pagavathigounder. A review of online learning in supervised neural networks. Neural Computing and Applications, 2014, vol. 25, no 3-4, p. 491-509.

[67] KARAYIANNIS Nicolaos and VENETSANOPOULOS Anastasios N. Artificial neural networks: learning algorithms, performance evaluation, and applications. Springer Science & Business Media, 2013.

[68] KARAHOCA Adem, KUCUR Turkalp, and AYDIN Nizamettin. Data mining usage in emboli detection. In : ECSIS Symposium on Bio-inspired, Learning, and Intelligent Systems for Security, BLISS. IEEE, 2007. p. 159-162.

[69] CORTES Corinna and VAPNIK Vladimir. Support-vector networks. Machine learning, 1995, vol. 20, no 03, p. 273-297.

[70] KARAÇALI Bilge, RAMANATH Rajeev, and SNYDER Wesley E. A comparative analysis of structural risk minimization by support vector machines and nearest neighbor rule. Pattern Recognition Letters, 2004, vol. 25, no 01, p. 63-71.

[71] DORAN Gary and RAY Soumya. A theoretical and empirical analysis of support vector machine methods for multiple-instance classification. Machine Learning, 2014, vol. 97, no 1-2, p. 79-102.

[72] ANDREW Alex M. An Introduction to Support Vector Machines and Other Kernel-based Learning Methods. Kybernetes, 2013.

[73] WANG Lipo. Support vector machines: theory and applications. Springer Science & Business Media, 2005.

[74] TOMAR, Divya et AGARWAL, Sonali. Twin support vector machine: a review from 2007 to 2014. Egyptian Informatics Journal, 2015, vol. 16, no 01, p. 55-69.

[75] WU Kuo-Ping and WANG Sheng-De. Choosing the kernel parameters for support vector machines by the inter-cluster distance in the feature space. Pattern Recognition, 2009, vol. 42, no 05, p. 710-717.

[76] SERBES, Gorkem, SAKAR, Betul Erdogdu, GULCUR, Halil Ozcan, et al. An emboli detection system based on Dual Tree Complex Wavelet Transform and ensemble learning. Applied Soft Computing, 2015, vol. 37, p. 87-94.

[77] GHAZALI Najah, JAAFAR Haryati, and RAMLI Dzati Athiar. Microembolus Classification Using MFCC and LPC Feature Extractions. Recent Advances in Electrical Engineering and Educational Technologies. Athens, Greece, November 2014. p.185-190.

[78] BOLÓN-CANEDO Verónica, SÁNCHEZ-MARONO Noelia, ALONSO-BETANZOS Amparo, BENÍTEZ José Manuel, and HERRERA Francisco. A review of microarray datasets and applied feature selection methods. Information Sciences, 2014, vol. 282, p. 111-135.

[79] STORN Rainer and PRICE Kenneth. Differential evolution–a simple and efficient heuristic for global optimization over continuous spaces. Journal of global optimization, 1997, vol. 11, no 04, p. 341-359.

[80] PRICE Kenneth, STORN Rainer M, and LAMPINEN Jouni A. Differential evolution: a practical approach to global optimization. Springer Science & Business Media, 2006.

[81] SEHGAL Smriti, KUMAR Sushil, et BINDU M. Hima. Remotely sensed image thresholding using OTSU & differential evolution approach. In : 7th International Conference on Cloud Computing, Data Science & Engineering-Confluence, 2017. IEEE, 2017. p. 138-142.

[82] SU Haijun, YANG Yupu, and ZHAO Liang. Classification rule discovery with DE/QDE algorithm. Expert Systems with Applications, 2010, vol. 37, no 02, p. 1216-1222.

[83] KHUSHABA Rami, AL-ANI Ahmed, and AL-JUMAILY Adel. Feature subset selection using differential evolution. Advances in neuro-information processing, Springer Berlin Heidelberg, 2009, p. 103-110.

[84] STORN Rainer. Differential evolution research–trends and open questions. In : Advances in differential evolution. Springer Berlin Heidelberg, 2008. p. 1-31.

[85] HAUPT Randy L, and HAUPT Sue Ellen. Practical genetic algorithms. John Wiley & Sons, 2004.

[86] KHUSHABA Rami N, AL-ANI Ahmed, and AL-JUMAILY Adel. Feature subset selection using differential evolution and a statistical repair mechanism. Expert Systems with Applications, 2011, vol. 38, no 09, p. 11515-11526.

[87] VIDAL René, MA Yi, and SASTRY S. Shankar. Principal Component Analysis. In : Generalized Principal Component Analysis. Springer New York, 2016. p. 25-62.

[88] CATTELL Raymond B. The scree test for the number of factors. Multivariate behavioral research, 1966, vol. 01, no 02, p. 245-276.

[89] SERBES Gorkem, SAKAR Betul Erdogdu, GULCUR Halil Ozcan, and AYDIN Nizamettin. An emboli detection system based on Dual Tree Complex Wavelet Transform and ensemble learning. Applied Soft Computing, 2015, vol. 37, p. 87-94.

[90] XU Da and WANG Yuanyuan. An automated feature extraction and emboli detection system based on the PCA and fuzzy sets. Computers in Biology and Medicine, 2007, vol. 37, no 06, p. 861-871.

[91] LI Wenkai and GUO Qinghua. A new accuracy assessment method for one-class remote sensing classification. IEEE Transactions on Geoscience and Remote Sensing, 2014, vol. 52, no 08, p. 4621-4632.

[92] CICCHETTI Domenic V, KLIN Ami, and VOLKMAR Fred R. Assessing Binary Diagnoses of Bio-behavioral Disorders: The Clinical Relevance of Cohen's Kappa. The Journal of Nervous and Mental Disease, 2017, vol. 205, no 01, p. 58-65.

[93] BANDOS Andriy I, GUO Ben, and GUR David. Estimating the Area Under ROC Curve When the Fitted Binormal Curves Demonstrate Improper Shape. Academic Radiology, 2017, vol. 24, no 02, p. 209-219.

[94] FERRARO Maria Brigida, COLUBI Ana, GONZÁLEZ-RODRÍGUEZ Gil, COPPI Renato. A determination coefficient for a linear regression model with imprecise response. Environmetrics, 2011, vol. 22, no 04, p. 516-529.

[95] PIRON Julien, ESCOFFRE Jean-Michel, KADDUR Kadija, NOVELL Anthony, and BOUAKAZ Ayache. Enhanced gene transfection using ultrasound and Vevo Micromarker® microbubbles: Microbubbles-assisted ultrasound and gene delivery. In: Ultrasonics Symposium (IUS), IEEE, 2010. p. 1586-1589.

[96] PALANCHON P, BENOUDJIT N, BAHAZ M, CHERRID N, and BOUAKAZ Ayache. P1A-5 Analysis of Backscattered Signals with a Neural Network Model for Microemboli Classification. In : Ultrasonics Symposium, IEEE, 2007. p. 1259-1261.

[97] SINGH Bikesh Kumar, VERMA Kesari, and THOKE A. S. Investigations on impact of feature normalization techniques on classifier's performance in breast tumor classification. International Journal of Computer Applications, 2015, vol. 116, no 19. p. 11-16.

[98] THEDE Leslie D. Practical analog and digital filter design. Norwood, Mass, USA : Artech House, 2005.

[99] COLOMINAS M. A, SCHLOTTHAUER G, and TORRES M. E. Complete ensemble EMD and Hilbert transform for heart beat detection. In: VI Latin American Conference in Biomedical Engineering. 2014. p. 496-499.

[100] TAHAR Neffati, L'électronique de A à Z, Paris, Dunod, 2006, p. 26-27.

[101] NGUI Wai Keng, LEONG M Salman, HEE Lim Meng, and ABDELRHMAN Ahmed M. Wavelet analysis: mother wavelet selection methods. In : Applied mechanics and materials. Trans Tech Publications, 2013, vol. 393. p. 953-958.

[102] STRANG Gilbert and NGUYEN Truong. Wavelets and filter banks. SIAM, 1996.

[103] MISITI Michel, MISITI Yves, OPPENHEIM Georges, and POGGI Jean-Michel. Matlab Wavelet Toolbox User\'s Guide. Version 3. 2004.

[104] ERIŞTI Hüseyin, UÇAR Ayşegül, and DEMIR Yakup. Wavelet-based feature extraction and selection for classification of power system disturbances using support vector machines. Electric power systems research, 2010, vol. 80, no 07, p. 743-752.

[105] ROSSI Fabrice, LENDASSE Amaury, FRANÇOIS Damien, WERTZ Vincent, and VERLEYSEN Michel. Mutual information for the selection of relevant variables in spectrometric nonlinear modelling. Chemometrics and intelligent laboratory systems, 2006, vol. 80, no 02, p. 215-226.

[106] DONOHO David L. De-noising by soft-thresholding. IEEE transactions on information theory, 1995, vol. 41, no 03, p. 613-627.

[107] BOASHASH, Boualem. Estimating and interpreting the instantaneous frequency of a signal. II. Algorithms and applications. Proceedings of the IEEE, 1992, vol. 80, no 04, p. 540-568.

PUBLICATIONS RELATED TO THIS THESIS

The thesis is based on the following papers:

1- **FERROUDJI Karim**, BENOUDJIT Nabil, et BOUAKAZ Ayache. An automated microemboli detection and classification system using backscatter RF signals and differential evolution. Australasian Physical & Engineering Sciences in Medicine, 2017, vol. 40, no 1, p.85-99.

2- **FERROUDJI Karim**, BENOUDJIT Nabil, BAHAZ Mohamed, et BOUAKAZ Ayache. Selection of a suitable mother wavelet for microemboli classification using SVM and RF signals. In: 2012 24th International Conference on Microelectronics (ICM),. IEEE, 2012. p. 1-4.

3- BENOUDJIT Nabil, **FERROUDJI Karim**, BAHAZ Mohamed, et BOUAKAZ Ayache. In vitro microemboli classification using neural network models and RF signals. Ultrasonics, 2011, vol. 51, no 3, p. 247-252.